Local Electron Transport on The Nanoscale

By

Shenglai He

Dissertation

Submitted to the Faculty of the

Graduate School of Vanderbilt University

in partial fulfillment of the requirements

for the degree of

DOCTOR OF PHILOSOPHY

in

Physics

September 30, 2017

Nashville, Tennessee

Approved:

Kálmán Varga, Ph.D.

Sait Umar, Ph.D.

Yaqiong Xu, Ph.D.

Greg Walker, Ph.D.

TABLE OF CONTENTS

LIST OF TABLES

LIST OF FIGURES

Chapter 1

Introduction

Nanoscale research is a hot topic worldwide and attracts scientists from different backgrounds due to a variety of exotic features in physical and chemical properties. The nanosacle is considered to be on the order of 1-100 nm length where quantum mechanical effects play an important role in determining material properties. The standard method to deal with many-body quantum mechanical problems is to solve many-body Schrödinger equation. However, the problem with this method is the huge computational effort, which makes it virtually impossible to efficiently solve large and complex systems. Density functional theory (DFT) has emerged as a popular alternative[1]. Instead of solving the many-body wavefunctions, it takes the electron density as the key variable and greatly reduces the computational cost. DFT has been widely used to investigate the electronic structure of nanoscale materials [2, 3, 4, 5, 6, 7, 8, 9, 10, 11].

Novel nano electronic devices are necessary in order to continue the advancement of computational power of microprocessors in the next decades. Lots of experimental and theoretical work has been done in this area[12, 13, 14, 15, 16, 17, 18, 19, 20, 21, 22, 23, 24]. On the theory side, it is an open boundary system and usually modeled as a device region connected to semi-infinite electrodes [25, 26, 27, 28, 29, 30, 7, 31]. The general task is to calculate the transport properties. The most common approach to treat transport problems is based on the Landauer formalism combined with DFT [25, 7, 26], which is limited to the steady-state regime. However, though DFT is quite reliable for calculating the electronic structure of molecules and solids, it is strictly a ground state theory. The transport problem is a dynamic process and usually involves excited states. Therefore, Time-dependent DFT (TDDFT) is a more suitable method to describe the transport property. In addition, most experimental and theoretical work focuses on global observables, such as current-

voltage (I-V) curve and the transmission spectrum. However, the underlying physics, for example the local electron pathway, is usually neglected. As devices get ever smaller, approaching nano scale, the study of spatial dependency of current density is important, as it unveils the electron pathway through the structure and can help us better understand the overall transport properties. Recent experiments have attempted to image the current flow in materials[32, 33, 34, 35]. However, imaging local currents at atomistic level is still challenging, more standard and accurate method still needs to be developed. In this thesis, we use TDDFT to investigate the local electron transport in nanomaterials. In Chapter 2 we briefly review the framework of DFT and TDDFT. We will also discuss the two time-dependent transport methods used in this thesis to study local currents. In Chapter 3 we investigate various time propagation schemes for the solution of the time-dependent Schrödinger equation. In Chapter 4 we will introduce a new method for time propagation of the coupled Maxwell and time-dependent Kohn-Sham equation. In Chapter 5 we will investigate the spatial current distribution in graphene nanoribbon under electrical bias using TDDFT. In Chapter 6 We will use the source potential method to study local electron pathway in various nanostructures. In Chapter 7 We will summarize the thesis.

Chapter 2

Formalism

2.1 First Principle Calculations

The basic approach to solve many-body quantum mechanical problem is to solve the Schrödinger equation:

$$H\psi(\mathbf{r}) = E\psi(\mathbf{r}), \tag{2.1}$$

where $\psi(\mathbf{r})$ is the wavefunction of the system. H is the system Hamiltonian operator and is expressed as:

$$H = -\sum_{i=1} \frac{\hbar^2}{2m}\nabla^2_{\mathbf{r_i}} + \frac{1}{2}\sum_{i=1,j} \frac{e^2}{|\mathbf{r_i} - \mathbf{r_j}|} + V, \tag{2.2}$$

Here the first term is the electron kinetic energy, the second term the interelectronic repulsions and V denotes the external potential and background potential, such as the lattice of atomic nuclei. In principle, it is possible to numerically solve the many-body Schrödinger equation. In practice, however, the problem rapidly becomes intractable as the number of electrons increases because of the huge computational expense. For example, in the popular Hartree-Fock approximation, the computational cost can be $O(N^4)$ to $O(N^3)$, where N is the number of electrons.

2.2 Density Functional Theory

DFT has emerged as a popular way to solve the complex many-body problem. Instead of solving the many-body wavefunction, it takes the electron density as the key variable and greatly lowers the computational cost, which makes the calculation of larger systems possible . DFT has been widely used to investigate the electronic structure of nanoscale materials. In this section, I will briefly review the foundations of DFT, including the Hohenberg-Kohn theorem, the Kohn-Sham equations, and exchange-correlation functional.

2.2.1 Hohenberg-Kohn Theorem

In 1964, Hohenberg and Kohn introduced the Hohenberg-Kohn theorem, which consists of 2 principles. The first principle is:

1. the external potential is uniquely determined by the corresponding ground-state electronic density, to within an additive constant.

The proof can be found in most solid-state physics books [36]. Since the electron density $n(\mathbf{r})$ determines the external potential and the external potential determines the ground state energy, the system energy can be express as a function of electron density:

$$E(n(\mathbf{r})) = F(n(\mathbf{r})) + \int d\mathbf{r} V(\mathbf{r}) n(\mathbf{r}), \tag{2.3}$$

where $F(n(\mathbf{r}))$ denotes the kinetic and potential energy of the system and $V(\mathbf{r})$ is the external potential. The second principle is: *2. For all v-representable densities* $n(\mathbf{r})$*,* $E(n(\mathbf{r})) \geq E_0$*, where* E_0 *is the ground-state energy for N electrons in the external potential* $V(\mathbf{r})$.

Thus the problem of solving the Schrödinger equation for ground-states can be re-cast into a variational problem of minimizing the functional $E(n(\mathbf{r}))$ with respect to v-representable densities $n(\mathbf{r})$.

2.2.2 Kohn-Sham Equations

The key is to find the expression of the above energy functional. The most popular way is to solve Kohn-Sham equation, which is the one electron Schrödinger equation of a fictitious system of non-interacting electrons, that generate the same density as any given system of interacting electrons. In Kohn-Sham theory, the total energy of the system is expressed as:

$$E(n(\mathbf{r})) = T(n(\mathbf{r})) + E_H(n(\mathbf{r})) + E_{xc}(n(\mathbf{r})) + \int d\mathbf{r} V_{ext}(\mathbf{r}) n(\mathbf{r}), \tag{2.4}$$

where T is the kinetic energy of a system of non-interacting electrons and expressed in terms of Kohn-Sham orbitals (a set of non-interacting orbitals) :

$$T(n(\mathbf{r})) = \sum_{i=1,N} \int d\mathbf{r} \phi_i^*(n(\mathbf{r}))(-\frac{\hbar^2}{2m}\nabla^2)\phi_i(n(\mathbf{r})), \tag{2.5}$$

E_H is the Hartree energy and given by,

$$E_H(n(\mathbf{r})) = \frac{e^2}{2} \int d\mathbf{r} \int d\mathbf{r}' \frac{n(\mathbf{r})n(\mathbf{r}')}{|\mathbf{r}-\mathbf{r}'|}, \tag{2.6}$$

E_{xc} is called the exchange-correlation energy which contains the complicated many-body effects, and V_{ext} is the external potential acting on the real system.

The Kohn-Sham equations are then found by varing the total energy with respect to Kohn-Sham orbitals with the constraint that the total number of electrons in the system is fixed,

$$\begin{aligned} \left[-\frac{\hbar^2}{2m}\nabla^2 + V_{KS}(\mathbf{r})\right]\phi_i(\mathbf{r}) &= \varepsilon_i \phi_i(\mathbf{r}) \\ V_{KS}(\mathbf{r}) &= V_{ext}(\mathbf{r}) + e^2 \int d\mathbf{r}' \frac{n(\mathbf{r}')}{|\mathbf{r}-\mathbf{r}'|} + \frac{\delta E_{XC}(n(\mathbf{r}))}{\delta n(\mathbf{r})}, \end{aligned} \tag{2.7}$$

where V_{KS} is the Kohn-Sham potential, a local effective potential in which the non-interacting electrons move. The electron density is then given by,

$$n(\mathbf{r}) = \sum_{i=1,N} |\phi_i(\mathbf{r})|^2. \tag{2.8}$$

Note that the Kohn-Sham Hamiltonian is a functional of density, and simultaneously one requires eigenvectors of the Hamiltonian to calculate density. The problem is thus a self-consistent one. One typically choose an initial guess for ϕ_i and construct the corresponding Kohn-Sham hamiltonian. Then one solves Eq. (2.7) to obtain an updated guess for ϕ_i. The process is repeated until ϕ_i stops changing by an appreciable amount.

The Kohn-Sham DFT is in principle an exact theory. However, in practice, the form of exchange-correlation (XC) functional is unkonwn and approximation is needed. Various

methods have been developed to approximate the XC functional, and a comprehensive survey of functionals is beyond the scope of this thesis. The most simple and widely used form is the local density approximation (LDA). Thomas-Fermi is the first to introduce the concept of local density, which is derived from a homogeneous electron gas model. The XC functional is defined as,

$$E_{XC}(n(\mathbf{r})) = \int d\mathbf{r}\varepsilon_{XC}(n(\mathbf{r}))n(\mathbf{r}) = \int d\mathbf{r}[\varepsilon_X(n(\mathbf{r})) + \varepsilon_C(n(\mathbf{r}))]n(\mathbf{r}) \tag{2.9}$$

Where ε_X is the exchange part which is known exactly from the case of a homogeneous electron liquid and turns out to be,

$$\varepsilon_X(n(\mathbf{r})) = -(\frac{81}{64\pi})^{\frac{1}{3}} n(\mathbf{r})^{\frac{1}{3}}, \tag{2.10}$$

ε_C is the correlation part. In this thesis, the correlation functional was calculated for a uniform electron gas using Quantum Monte Carlo simulations [37] and was paramized by Perdew and Zunger [38]. The functional is given by,

$$\varepsilon_C(n(\mathbf{r})) = \begin{cases} -0.1423(1+1.0529\sqrt{r_s}+0.3334r_s)^{-1}, & r_s \geq 1 \\ -0.048+0.031lnr_s-0.0117r_s+0.002r_s lnr_s, & r_s < 1, \end{cases} \tag{2.11}$$

Where the Wigner-Seitz radiurs is defined as

$$r_s = (\frac{4\pi n(\mathbf{r})}{3})^{-1/3}, \tag{2.12}$$

2.3 Time-Dependent Density Functional Theory

TDDFT theory is an extension of ground state DFT to describe the properties and dynamics of many-body systems in the presence of time-dependent external potentials, such as electric or magnetic fields. Similar to DFT, instead of solving the full time-dependent

many-body Schrödinger equation, this theory works with the time-dependent electron density and makes the calculation of large system computational feasible. TDDFT has become a popular method in physics and chemistry to investigate features such as the calculation of optical properties[39, 40, 41, 39, 42], field emission [43, 44, 45, 46], ultrafast strong field processes[47, 48, 49, 50, 51, 52, 53, 54, 55, 56, 57], and ion collisions [58, 59, 60]. In this thesis, we apply it to the study of dynamic electron transport processes. We begin in the subsection 2.3.1 with a summary of the Runge-Gross theorem which provides a rigorous legitimation for a description of a time-dependent many-electron system in terms of the time-dependent electron density. In the subsection 2.3.2 we introduce the time-dependent Kohn-Sham (TDKS) equations. They provide a practical scheme for the calculation of timede-dependent densities and currents of an electronic many-body system.

2.3.1 Runge-Gross Theorem

The breakthrough for modern TDDFT was achieved in 1984 when Runge and Gross [61] proved the uniqueness of the mapping between time-dependent densities and potentials. The starting point is the time-dependent many-body Schrödinger equation :

$$\left(i\hbar\frac{\partial}{\partial t} - H(\mathbf{r},t) \right) \psi(\mathbf{r},t) = 0 \tag{2.13}$$

The Runge and Gross theorem states the following:

Two solutions $\psi(\mathbf{r},t)$ and $\psi'(\mathbf{r},t)$ of the Eq. 2.13 which evolve from a fixed common initial state ψ_0 under the influence of the single particle potentials $V(\mathbf{r},t)$ and $V'(\mathbf{r},t)$, respectively, always lead to different electron densities $n(\mathbf{r},t)$ and $n'(\mathbf{r},t)$, provided the two potentials $V(\mathbf{r},t)$ and $V'(\mathbf{r},t)$ differ by more than a purely time-dependent constant.

The proof can be found in the original paper by Runge and Gross [61]. Similar to Hohenberg-Kohn theorem, the Runge and Gross theorem proves the one-to-one correspondence of time-dependent density and external potential.

2.3.2 Time-Dependent Kohn-Sham Equations

Similar to the case of DFT, the calculation of time-dependent densities would be a lot simpler if we can map the many-electron problem onto a set of N fictitious non-interacting single-particle problems. In the Runge and Gross theorem, the existence of such non-interacting v-representability is postulated. In 1999, Van Leeuwen demonstrated the existence of such single-particle potential and provided the full legitimation for the time-dependent Kohn-Sham (TDKS) scheme [62]. The Van Leeuwen theorem states the following:

A time-dependent particle density $n(\mathbf{r},t)$ obtained from a given many-particle system can, under mild restrictions on the initial state, always be reproduced by an external potential $V'(r,t)$ in a many-particle system with different many-particle interactions. Given the initial state of this other many-particle system, the potential $V'(r,t)$ is unique up to a purely time-dependent function.

The proof can be found in the original paper [62]. According to the theorem, we can set the many-particle interactions of the second system to zero and find an effective single-particle potential $V_{KS}(r,t)$ which reproduces the density of the given interacting many-particle system. Therefore we can introduce an auxiliary system of non-interacting Kohn-Sham particles that move in the effective potential $V_{KS}(r,t)$ and evolves according to the TDKS equations:

$$i\hbar\frac{\partial}{\partial t}\phi_i(\mathbf{r},t) = \left[-\frac{\hbar^2}{2m}\nabla^2 + V_{KS}(\mathbf{r},t)\right]\phi_i(\mathbf{r},t), \tag{2.14}$$

The density is defined as

$$n(\mathbf{r},t) = \sum_{i=1,N} |\phi_i(\mathbf{r},t)|^2 \tag{2.15}$$

In analogy to ground-state DFT, the effective single-particle potential $V_{KS}(\mathbf{r},t)$ is decomposed as :

$$V_{KS}(\mathbf{r},t) = v_{ext}(\mathbf{r},t) + v_H(\mathbf{r},t) + v_{xc}(\mathbf{r},t) \tag{2.16}$$

where the first term is the time-dependent external potential and the second term denotes the time-dependent Hartree potential,defined as in the static case :

$$v_H(\mathbf{r},t) = e\int d\mathbf{r}'\frac{n(\mathbf{r}',t)}{|\mathbf{r}-\mathbf{r}'|} \tag{2.17}$$

The only unknown piece is the exchange correlation potential $v_{xc}(\mathbf{r},t)$ which accounts for the many-body effect. Given the fact that the one-to-one mapping between densities and potentials is only established for fixed initial states, the many-body effect term $v_{xc}(\mathbf{r},t)$ depends, not only on the entire history of the density $n(\mathbf{r},t)$, but also on the initial many-body wavefunction ψ_0. Compared to the ground-state DFT, this causes serious complications, since a new exchange-correlation functional $v_{xc}(\mathbf{r},t)$ is needed for every possible initial wavefunction. Fortunately, the initial-state dependence of the time-dependent exchange-correlation potential drops out if the initial state is a non-degenerate ground state. In this case, the Hohenberg-Kohn theorem of static DFT tells us that the initial wavefunction is a functional of ground-state density and hence the time-dependent exchange-correlation potential becomes a functional of the history of the time-dependent density alone. Most practical calculations are covered by this case, but the functional is still an extremely complex object as it involves the history of the time-dependent density. In practice, it has to be approximated and one of the most common and well tested approaches is the so called adiabatic approximation. Here the form of the exchange-correlation potential from static DFT is taken as the approximation to the time-dependent one :

$$v_{xc}^{tddft}[n(\mathbf{r},t)] = v_{xc}^{dft}[n(\mathbf{r},t)] \tag{2.18}$$

Any of the exchange-correlation potentials used in the static DFT may be used in the above equation. In particular, with the insertion of the static LDA XC potential one obtains the adiabatic local density approximation (ALDA).

2.3.3 Time Propagator

TDKS equation can be solved by time propagating the Kohn-sham orbitals from the initial state to some time, t, using a time-evolution operator:

$$\begin{aligned} U(0,t) &= \mathscr{T} \exp\left[-\frac{i}{\hbar}\int_0^t H(\mathbf{r},t')dt'\right], \\ \phi(\mathbf{r},t) &= U(0,t)\phi(\mathbf{r},0) \end{aligned} \tag{2.19}$$

where $\mathscr{T}$ denotes time ordering. In practice, $U(0,t)$ is split into a product of multiple short-time propagators,

$$U(0,t) = \prod_q U(t_q, t_q+\delta t), \quad t_q = q\delta t, \tag{2.20}$$

which evolves the Kohn-Sham orbitals from t_q to $t_q+\delta t$. The short-time propagator is defined by,

$$U(t_q, t_q+\delta t) = \exp\left[-\frac{i\delta t}{\hbar}H(\mathbf{r},t_q)\right], \tag{2.21}$$

The time step, δt, is chosen to be sufficiently small so that the Hamiltonian can be treated as constant. Implementing a numerical solution to Eq.2.19 requires one to construct a matrix form of the time-propagator Eq.2.21, which is defined via the Taylor expansion:

$$U(t_q, t_q+\delta t) = \sum_{n=0}^{\infty} \frac{1}{n!}\left(-\frac{i\delta t}{\hbar}H(\mathbf{r},t_q)\right)^n \tag{2.22}$$

The complete details of this derivation and the description of the formal propagator may be found, for instance, in Castro et al.[63]. Typically the initial Kohn-Sham orbitals, $\phi(\mathbf{r},0)$, are known and the orbitals at any subsequent time is obtained through the application of Eq. 2.19. In this thesis, a fourth-order Taylor expansion is used to approximate the time-propagator 2.21. Given a sufficiently small time step, this method provides excellent accuracy with reasonable computational cost[64, 65, 59].

2.4 Time-Dependent Transport Calculation

The non-equilibrium Green's function (NEGF) combined with DFT is a popular method to investigate steady state quantum transport phenomena in nanodevices, where the devices are characterized as a small active device region connected to two bulk electrodes. An overview of the theory can be found in articles[66] and book[67].Using this method, transport properties such as current-voltage and transmission spectrum can be obtained. However, the fundamental issue with this method is that DFT is a ground state theory, which is not suitable to describe a highly non-equilibrium open transport system. Therefore, the agreement between experiments and calculations is often poor. Since electron transport is intrinsically a dynamical nonequilibrium process, the time-dependent approach is a more natural choice to solve quantum transport problems. Specifically, the TDDFT is a computationally feasible approach to access excited states, and it is expected to give a better description of the nonequlibrium current carrying states than the conventional DFT. In this section, we will introduce two time-dependent approaches used in this thesis to study the local electron transport.

2.4.1 Bias Potential

In this approach, A rectangular simulation box with zero-boundary condition is used. The initial ground state of the system is prepared by performing a static DFT calculation. Then a bias potential is applied to the system to drive the electron flow. The external bias potential is defined as :

$$V_{\text{ext}}(\mathbf{r},t) = \begin{cases} f(t)\frac{\mathrm{V_b}}{2}, & \mathbf{r} \in \text{left electrode} \\ 0, & \mathbf{r} \in \text{central region} \\ -f(t)\frac{\mathrm{V_b}}{2}, & \mathbf{r} \in \text{right electrode}, \end{cases} \tag{2.23}$$

where V_b is a constant and determines the magnitude of the bias potential. The local current is investigated within the central region. $f(t)$ is a ramp function to slowly turn on the bias potential to avoid numerical instability, and is given by,

$$f(t) = \begin{cases} \frac{t}{\tau}, & t \leq \tau \\ 1, & t > \tau, \end{cases} \tag{2.24}$$

where, in this thesis, the ramp time is $\tau = 0.5$ fs. The system then evolves according to TDKS equation Eq. 2.14. As discussed in the propagator section 2.3.3, the Kohn-Sham orbitals are time propagated and a fourth order taylor expansion is used to approximate the time propagator.

$$\begin{aligned} U(t_q, t_q + \delta t) &\approx \sum_{n=0}^{4} \frac{1}{n!} \left(-\frac{i\delta t}{\hbar} H(\mathbf{r}, t_q) \right)^n \\ \psi(\mathbf{r}, t + \delta t) &= U(t, t + \delta t)\psi(\mathbf{r}, t) \end{aligned} \tag{2.25}$$

As the bias potential drives electron current to the boundary of the simulation cell, the zero-boundary condition used in our simulations will lead to an unphysical reflection. To avoid this effect, a complex absorbing potential (CAP) of the form given by Manolopoulos [68] is added in the region close to the boundary:

$$-iw(x) = -i\frac{hbar^2}{2m} \left(\frac{2\pi}{x_2 - x_1} \right)^2 f(y), \tag{2.26}$$

where x_1 is the start and x_2 is the end of the absorbing region, m is the electron's mass and $f(y)$ is defined as:

$$f(y) = \frac{4}{c^2} \left(\frac{1}{(1+y)^2} + \frac{1}{(1-y)^2} - 2 \right), \quad y = \frac{x - x_1}{x_2 - x_1}; \tag{2.27}$$

where $c = 2.62$ is a numerical constant. In our calculation, the CAP would reduce the electron density in the electrode regions and, through the Hartree and exchange-correlation potentials, affect the Kohn-Sham orbitals in the region where the CAP is zero. To solve this

problem, we have implemented the method proposed in Ref. [69], where the CAP potential (W) is multiplied by a projector P :

$$W \rightarrow PWP. \tag{2.28}$$

The projector P is given by,

$$P = 1 - \sum_{i=1}^{N} |\psi_i(\mathbf{r},0)\rangle\langle\psi_i(\mathbf{r},0)|, \tag{2.29}$$

where N is the number of occupied orbitals and $\psi_i(\mathbf{r},0)$ are the ground state orbitals. This projected CAP projects out the ground state orbitals and thus ensures that only excited electrons in the CAP region are absorbed.

In our calculation, we use norm-conserving Troullier-Martins [70] pseudopotentials to represent the coulomb well of the atomic nucleus and the frozen core electrons, which are very deeply bound and inactive chemically. These pseudopotentials preserve the scattering properties of the combined nucleus and core electron system. In the presence of such non-local pseudopotentials the conventional definition of current density,

$$\mathbf{J}_c = (e\hbar/2mi)[\psi^*(\mathbf{r},t)\nabla\psi(\mathbf{r},t) - \psi(\mathbf{r},t)\nabla\psi^*(\mathbf{r},t)], \tag{2.30}$$

does not satisfy current conservation, $\nabla\cdot\mathbf{J}_c = 0$. We therefore calculate the local current using the expression proposed by Ref. [71],

$$\mathbf{J}(\mathbf{r},t) = -e\sum_{i}^{N}\int_{\Omega} d\mathbf{r}^{'}\,\psi_i^*(\mathbf{r},t)\mathbf{v}(\mathbf{r},\mathbf{r}^{'})\psi_i(\mathbf{r}^{'},t), \tag{2.31}$$

where Ω is the volume of the simulation cell and $\mathbf{v}(\mathbf{r},\mathbf{r}^{'})$ is the so called velocity operator,

defined by,

$$\mathbf{v}(\mathbf{r},\mathbf{r}^{'}) = \frac{-i\hbar}{m}\nabla\delta(\mathbf{r}-\mathbf{r}^{'}) + \frac{1}{i\hbar}\left[\mathbf{r}V_{nonlocal}(\mathbf{r},\mathbf{r}^{'}) - V_{nonlocal}(\mathbf{r},\mathbf{r}^{'})\mathbf{r}^{'}\right]. \tag{2.32}$$

One advantage of this approach is that it only needs a single time propagation, while in NEGF-DFT, one needs converged calculation for many energies to calculate the current. At the same time, NEGF-DFT is evidently time independent, while the TDDFT approach has a transient period before the time-independent limit is reached. A drawback of the approach is that it only works for finite bias, and zero bias conductance cannot be easily calculated.

2.4.2 Complex Injecting Potential

In this approach, a complex injecting potential, acting as an electron source, is added to the Hamiltonian. The system is then time propagated with continuous injection of electrons until a steady state is reached. One can then study the local electron pathway corresponding to the energy level of the injected electron.

Complex potentials have been a powerful tool in quantum mechanical calculations [72, 73, 74, 75]. The use of non-Hermitian Hamiltonian with complex potential extends the quantum mechanical calculations to open systems where the overall probability changes in time and allows simulation of transport and scattering phenomena. In the case of a complex potential :

$$U(\mathbf{r}) = V(\mathbf{r}) + iW(\mathbf{r}) \tag{2.33}$$

The continuity equation has the following form :

$$\frac{\partial n(\mathbf{r},t)}{\partial t} + \nabla\cdot\mathbf{j}(\mathbf{r},t) = \frac{2}{\hbar}W(\mathbf{r})n(\mathbf{r},t) \tag{2.34}$$

This equation shows that in the presence of complex potential the charge is not conserved.

The positive imaginary potential will inject and negative potential absorbs electrons, which can be used for simulating the coupling to a source and a drain. We have used the complex absorbing potential in the previous method to avoid unphysical reflection. However, the construction of injecting potential is not easy, as it has to be a steady source of electrons. In this thesis, we construct a point source potential that injects electron with a prescribed energy. To achieve this, the wavefunction of the system in a given source point $\mathbf{r_0}$ is constrained to be a steady state with energy E,

$$\psi(\mathbf{r_0},t) \equiv e^{-\frac{i}{\hbar}Et}\phi(\mathbf{r_0}) \tag{2.35}$$

Since we only need it at a single point, the form of function $\phi(\mathbf{r})$ is not important and only affects the normalization. The variational principle will be used to enforce constraint on the wavefuction in the time-dependent Schrödinger equation [76, 77]:

$$\begin{aligned} S = &\int_{t_1}^{t_2} dt \int d\mathbf{r}\psi(\mathbf{r},t)^*(i\hbar\frac{\partial}{\partial t}H_{KS})\psi(\mathbf{r},t) - \int_{t_1}^{t_2} dt \int d\mathbf{r}\lambda(\mathbf{r},t)[\delta(\mathbf{r}-\mathbf{r_0})(\psi(\mathbf{r},t)^* - \phi(\mathbf{r},t)^*)] \\ &- \int_{t_1}^{t_2} dt \int d\mathbf{r}\lambda(\mathbf{r},t)^*[\delta(\mathbf{r}-\mathbf{r_0})(\psi(\mathbf{r},t) - \phi(\mathbf{r},t))] \end{aligned} \tag{2.36}$$

where the first term is the variation functional for usual time-dependent Hamiltonian [78] and the other two terms add the constraint with a Lagrange multiplier function [76] $\lambda(\mathbf{r},t)$. Keeping the normalization integral $\int d\mathbf{r}\psi(\mathbf{r},t)^*\psi(\mathbf{r},t)$ constant, the variation of S is :

$$\delta S = \int_{t_1}^{t_2} dt \int d\mathbf{r}\delta\psi(\mathbf{r},t)^* \left(i\hbar\frac{\partial}{\partial t}H_{KS} - \frac{\lambda(\mathbf{r},t)}{\psi(\mathbf{r},t)}\delta(\mathbf{r}-\mathbf{r_0}) \right) \psi(\mathbf{r},t) + c.c. \tag{2.37}$$

Making the above variation $\delta S = 0$, one obtains the new time-dependent Schrödinger equation with the constraint of wavefunction at the source point $\mathbf{r_0}$,

$$\begin{aligned} i\hbar\frac{\partial\psi}{\partial t} &= H\psi \\ H &= H_{KS} - \frac{\lambda(\mathbf{r},t)}{\psi(\mathbf{r},t)}\delta(\mathbf{r}-\mathbf{r_0}). \end{aligned} \tag{2.38}$$

The Lagrange multiplier function, $\lambda(\mathbf{r},t)$, cannot be easily determined from the above equation. However, in order to obtain the desired steady state solution at energy E, its time dependent has to be of the form $e^{-\frac{i}{\hbar}Et}$ to cancel the time dependence of the steady state wavefunction $\psi(\mathbf{r},t) = e^{-\frac{i}{\hbar}Et}\psi(\hat{\mathbf{r}})$. The $\mathbf{r}$ of $\lambda(\mathbf{r},t)$ can also be dropped since we only need it at a single point $\mathbf{r_0}$. With this considerations the Hamiltonian can be written as :

$$H = H_{KS} - ae^{-\frac{i}{\hbar}Et}\frac{1}{\psi(\mathbf{r},t)}\delta(\mathbf{r}-\mathbf{r_0}) \tag{2.39}$$

The constant a only affects the amplitude of the wavefunction through Eq. 2.35. Because we are interested in the electron pathway through the system, we choose it to be $a = 1$. Therefore the source potential term has the following form:

$$V_{source} = -e^{-\frac{i}{\hbar}Et}\frac{1}{\psi(\mathbf{r},t)}\delta(\mathbf{r}-\mathbf{r_0}), \tag{2.40}$$

Which forces the solution to be equal to the solution $\psi_E(\mathbf{r})$ belonging to energy E after extended time propagation where steady state is reached. This new time-dependent equation Eq. 2.38 will then be solved by time propagation using the fourth order taylor time propagator proposed in the previous section 2.3.3. The initial wavefunction is chosen to be:

$$\psi(\mathbf{r},t=0) = \delta(\mathbf{r}-\mathbf{r_0}) \tag{2.41}$$

To avoid the reflection from the boundary of the simulation cell, a complex absorbing potential of the form Eq.2.26 is added in the region close to the boundary and effectively renders the system infinite in the transport direction. After a steady state is reached, the spatial current density will be calculated using Eq. 2.31. Alternatively one could use the Green's function $G(E) = (H_{KS} - E)^{-1}$ to project out $\psi_E(\mathbf{r})$ from an arbitrary function, but this is not feasible (the calculation of the inverse of large matrices is computationally more demanding than the time propagation). The source potential method greatly reduces

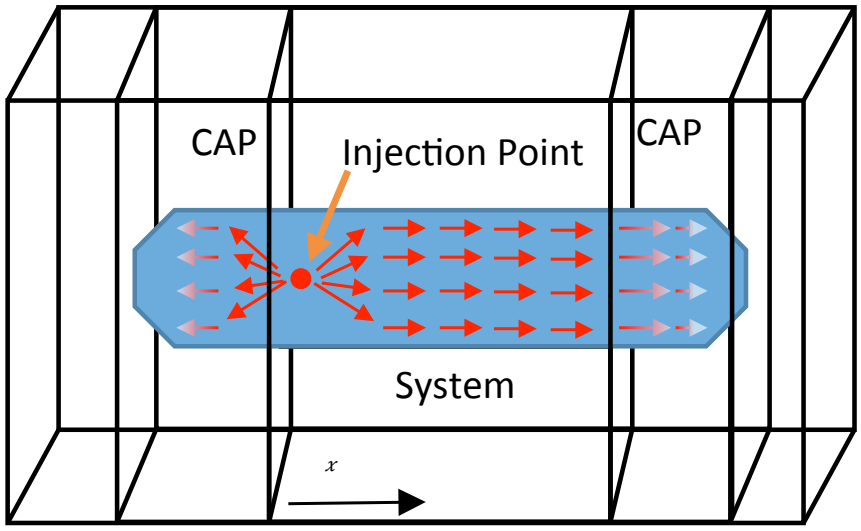

Figure 2.1: A diagram of the simulation setup. CAPs are placed at the beginning and end of the box in the transport direction. The CAP is placed so that the injected electron wave function is completely absorbed before it reaches the edge of the atomic potentials, making the finite system effectively infinite.

computational cost since one only need to propagate one orbital – the injected electron. Moreover, the source potential is more general and may have additional benefits in time dependent calculations (e.g. injecting a time dependent current, linear combination for different energies forming a wave packets, etc.). A diagram of the computational setup is shown in Fig. 2.1.

Chapter 3

Accuracy and Computational Efficiency of Real-Time Subspace Propagation Schemes

Time-dependent Density Functional Theory (TDDFT) has become successful for its balance of economy and accuracy. However, the computational cost of its application to large systems or long time scales remains prohibitively expensive. In this chapter, we investigate the numerical stability and accuracy of the Lánczos basis and the adiabatic eigenbasis methods to solve the time-dependent Kohn-Sham equations with finite and periodic boundary conditions. The bases considered are the Lánczos basis and the adiabatic eigenbasis. We compare the results to a benchmark fourth-order Taylor expansion of the time propagator. Our results show that it is possible to use larger time steps with the subspace methods, leading to a computational speedups by a factor of 2–3 over Taylor propagation. Accuracy is found to be maintained for certain energy regimes and small time scales. Work shown in this chapter has been published [79].

3.1 Background

Time-dependent density functional theory (TDDFT) [80, 81] has become widely used in the simulation of molecules, 2D materials, and bulk materials. Applications of TDDFT include the calculation of optical properties[39, 40, 41, 39, 42], field emission [43, 44, 45, 46], ultrafast strong field processes[47, 48, 49, 50, 51, 52, 53, 54, 55, 56, 57, 82], and ion collisions [58, 59, 60]. In the low energy limit, where the electronic density is directly coupled to an external first order perturbation, TDDFT can be cast into the Casida equation [83, 84]. The investigation of strong field phenomena requires the solution of the time-dependent Kohn-Sham (TDKS) equations directly.

The TDKS equations are given by Eq.2.14. In practice the solution of this equation involves time propagating the Kohn-Sham orbitals from initial state $\phi_m(\mathbf{r}, t_0)$ to any sub-

sequent time. This may be accomplished by exponentiating the Kohn-Sham Hamiltonian operator as shown in section 2.3.3,

Various schemes have been developed for the construction of the time propagator [85, 86, 87, 88, 89, 90, 91, 92, 93] including the polynomial propagators[63, 94], exponential propagators [95, 96], subspace propagation[97, 98, 99, 100, 101, 102, 56, 103, 104, 105, 106, 107, 63], and split-operator techniques[63, 108]. One propagation scheme of particular note is the fourth-order Taylor propagation [109, 110]. In this scheme, the exponential of the Hamiltonian is approximated with a fourth-order Taylor expansion. Taylor propagation of the TDKS equations has proven highly successful in many applications[43, 44, 45, 46, 48, 49, 50, 51, 59, 52, 53], and its popularity is due the simplicity of its implementation: only matrix-vector multiplication is needed, while inversion and diagonalization is avoided. One drawback of this approach is that the Taylor propagator is only conditionally stable. One also notes that the Taylor approximation breaks the unitarity of the propagator. In practice it is found that time steps of $\delta t \leq 0.001$ fs give stable, well converged, and highly accurate results. Furthermore, these small time steps preserve unitarity with a high degree of accuracy.

The requirement $\delta t \leq 0.001$ fs may be seen as an arbitrary constraint. One supposes that the size of the time step should relate to the underlying physics of the system under investigation. From the time-energy uncertainty relation, $\delta E \delta t \leq \frac{\hbar}{2}$, one obtains a physical upper bound on the possible time step: $\delta t_{\max} \leq \frac{\hbar}{2\delta E_{\max}}$. For example if the external field is sinusoidal with a wavelength of 520 nm, the time step should be smaller than $\delta t_{\max} \leq \frac{\hbar}{2\delta E_{\max}} = \frac{\hbar}{2\hbar\omega} = \frac{\lambda}{4\pi c} = \frac{520\text{nm}}{4\pi c} \approx 0.14$ fs. Below the absolute upper bound required to capture the underlying physics, one is free to choose any time step which provides sufficient accuracy for the lowest computational expense. As noted by Castro et al.[63], the time step and algorithm chosen should minimize the computational cost of propagation per unit time.

As theoretical and computational tools improve, it regularly becomes necessary to

reevaluate the various available propagation schemes. One-step explicit time propagators have been analyzed in Ref. [104] and it was found that the accuracy largely depends on the stiffness of the system. The Crank-Nicholson, split-operator method, the Magnus expansion, and the Lánczos propagator have been tested in Ref.[63]. The Lánczos propagator combined with the midpoint rule was found to be the most efficient technique. However, it is also noted that the choice of propagation scheme depends on the characteristic properties of the physical system and the external fields. Recently, adiabatic subspace approaches[106, 107] have been proposed to increase the time step. These works suggest that time steps as large as $0.2 - 0.5$ fs can be used in TDDFT calculations. The promise of larger time steps in these adiabatic eigenstate methods motivates their implementation and test in the present work.

In this chapter, we consider the accuracy and computational cost of propagation on two subspace bases, the Lánczos [97, 98, 99, 100, 101, 102, 56, 103, 104, 105] and adiabatic eigenvector [106, 107] bases. We use a multiscale propagation scheme where the TDKS equations are propagated on a short time step and the subspace basis is updated on a longer time step. We consider the application of these propagation schemes to the solution of multiple physically relevant systems, and solve the TDKS equations with finite and periodic boundary conditions. We also consider the effect of these propagation schemes on the accuracy of molecular dynamics calculations performed by coupling the TDKS equations with the nonadiabatic Ehrenfest dynamics[111, 112]. For both methods we find increased computational speed with only a moderate reduction in accuracy. The accuracy remains very high for certain time and energy regimes. In the implementation of these approaches a real space representation is used, and some of the conclusions of the tests are directly related to this representation. Real space grids are very popular [109, 113, 114, 115] and very powerful in TDDFT calculations, and the test calculations presensted in this chapter can help their further development.

The plan for this chapter is as follows. In section 3.2 we give the computational details

used. We then present the Taylor, Lánczos, and Adiabatic Eigenstate propagation schemes. In section 3.3 we give the results of the simulations using these three schemes for both finite and periodic boundary conditions. Finally, in section 3.4 we summarize and conclude this chapter.

3.2 Computational Details

We begin this section by describing the TDDFT with finite boundary conditions and the periodic case. Subsequently we describe the time propagation algorithms investigated.S

3.2.1 Time-Dependent Kohn Sham Equation

The Kohn-Sham Hamiltonian for the TDKS with finite boundary conditions is given by,

$$H_{\mathrm{KS}}^{\mathrm{finite}} = \left[-\frac{\hbar^2}{2m_e}\nabla^2 + v_{ext}(\mathbf{r}) + v_{Hxc}[n(\mathbf{r},t)](\mathbf{r})\right] + \int d^3\mathbf{r}' v_{pp}(\mathbf{r},\mathbf{r}'), \tag{3.1}$$

where $n(\mathbf{r},t)$ is the electron density, v_{ext} is the external potential, v_{Hxc} is the sum of the Hartree and exchange-correlation potentials, and v_{pp} is the sum of the pseudopotentials of the ions. The periodic TDKS equation is,

$$\begin{aligned} H_{\mathrm{KS}}^{\mathrm{periodic}} &= \frac{\hbar^2}{2m_e}(-i\nabla + \mathbf{k})^2 + v_{ext}(\mathbf{r},t) + V_{Hxc}[n(\mathbf{r},t)](\mathbf{r},t) \\ &\quad + \int d^3\mathbf{r}' e^{-i(\mathbf{k}\cdot\mathbf{r})} v_{pp}(\mathbf{r},\mathbf{r}') e^{i(\mathbf{k}\cdot\mathbf{r}')}. \end{aligned} \tag{3.2}$$

In this case the Kohn-Sham orbitals take the form of Bloch functions, $\varphi_{mk} = u_{mk}e^{i\mathbf{k}\cdot\mathbf{r}}$. For simplicity, we suppress the index k for the remainder of this section.

The time-dependent electron density is given by

$$n(\mathbf{r},t) = \sum_{i}^{N_{\mathrm{KS}}} 2\,|\varphi_m(\mathbf{r},t)|^2, \tag{3.3}$$

where N_{KS} is the number of Kohn-Sham orbitals and the factor of 2 accounts for spin

degeneracy. The Hartree potential is given by,

$$V_{\text{Hartree}} = \int \frac{e^2 n(\mathbf{r},t)}{|\mathbf{r}-\mathbf{r}'|} d\mathbf{r}', \tag{3.4}$$

where e is the electron charge. v_{pp} is the sum of Troullier-Martin [116] norm-conserving pseudopotentials. The exchange-correlation potential is approximated using the adiabatic local density approximation (ALDA) with the parameterization of Perdew and Zunger [117]. We solve the TDKS equations on a real space grid. Real space grids offer flexibility and ease of implementation.

The first stage of each simulation is to prepare the ground state Kohn-Sham orbitals, $\varphi_m(\mathbf{r},0)$, with a density functional theory (DFT) calculation. We consider four physical systems: benzene with an applied linear perturbation, proton-benzene collisions, the electron dynamics driven by an ultrashort laser pulse, and proton-graphene collisions. The first two simulations are performed by solving the TDKS equations with finite boundary conditions, and the proton-graphene collisions are performed with periodic boundary conditions.

The linear perturbation is applied to the benzene molecule at the start of the simulation by multiplying the ground state orbitals by a phase factor,

$$\varphi'_m(\mathbf{r},0) = \varphi_m(\mathbf{r},0) e^{if r_j}, \tag{3.5}$$

where $f = 0.01$ Å^{-1} is a small constant which defines the strength of the perturbation, and $r_j = x,y,z$ is the coordinate along which the perturbation is applied. The orbitals $\varphi'_i(\mathbf{r},0)$ are then propagated in real time.

The time-dependent potential of the laser field is given by the dipole approximation, $V_{\text{laser}} = \mathbf{r}\cdot\mathbf{E}(t)$. The time–dependent electric field given by,

$$\mathbf{E}(t) = \hat{\mathbf{k}} E_{\max} \exp\left[-\frac{(t-t_0)^2}{2a^2}\right] \sin\left[\omega(t-t_0)\right]. \tag{3.6}$$

The parameters a, t_0, and $E_{\max}$ define the width, initial position of the center, and the maximum amplitude of the Gaussian envelope, respectively. ω describes the frequency of the laser, and $\hat{\mathbf{k}}$ is a unit vector defining the polarization of the electric field.

For the proton-benzene and proton-graphene collisions, the proton is represented as a Coulomb potential whose center moves with constant velocity. The Coulomb potential is given by,

$$V_{proj}(\mathbf{r},t) = -\frac{qe}{\sqrt{|\mathbf{r}-\mathbf{R}_{\text{proton}}(t)|^2+\varepsilon^2}}, \tag{3.7}$$

where $\mathbf{R}_{\text{proton}}(t)$ is the position of the proton, q is the charge of the proton, and $\varepsilon = 0.01$ Å is a softening parameter used to avoid numerical instabilities. The position of the ions of the target benzene molecule or graphene sheet are updated using the Ehrenfest dynamics, where the ions follow classical trajectories driven by quantum forces derived from TDDFT. These forces are fed into Newton's second law,

$$\begin{aligned} M_i\frac{d^2\mathbf{R}_i}{dt^2} = Z_i\mathbf{E}_{\text{laser}}(t) + \sum_{j\neq i}^{N_{\text{ions}}}\frac{Z_iZ_j(\mathbf{R}_i-\mathbf{R}_j)}{|\mathbf{R}_i-\mathbf{R}_j|^3} \\ -\nabla_{\mathbf{R}_i}\int v_{pp}(\mathbf{r},\mathbf{R}_i)\rho(\mathbf{r},t)d\mathbf{r}, \end{aligned} \tag{3.8}$$

where M_i and Z_i are the mass and pseudocharge (valence) of the i-th ion, respectively, and N_{ions} is the total number of ions. For the periodic boundary conditions code, an Ewald summation is used to calculate the infinite sum of force terms.

3.2.2 Taylor Propagation

As noted in the background, the fourth-order Taylor propagation scheme has proved highly successful. In this scheme the exponential of the Hamiltonian is approximated as a fourth order Taylor expansion,

$$\exp\left[-\frac{i}{\hbar}H_{\text{KS}}(t_0)\delta t\right] = \sum_{n=0}^{4}\frac{1}{n!}\left(-\frac{i\delta t}{\hbar}H(\mathbf{r},t_0)\right)^n. \tag{3.9}$$

When a sufficiently small time step is used, the algorithm is conditionally stable and preserves the norm of the wave function for long time propagations [109]. For a fourth-order Taylor series the upper limit of the time step is,

$$\delta t < \frac{2.8\hbar}{E_{max}} \tag{3.10}$$

where E_{max} is the maximum eigenvalue of the Hamiltonian. For a real-space finite-difference calculation, the maximum eigenvalue can be estimated by the maximum particle-in-a-box eigenvalue for the given lattice,

$$E_{max} \approx 3\frac{\hbar^2}{2m}\left(\frac{\pi}{\Delta x}\right)^2 \tag{3.11}$$

where Δx is the grid spacing. For a typical grid spacing of 0.2 a.u. this gives a limit of $\delta t < 0.0076$ a.u. (0.00018 fs). This is just a rough estimate since the potential energy also gives a contribution, bringing the maximum time step closer to $\delta t \approx 0.001$ fs.

The Taylor approach is a popular method due to its simplicity. To apply the Taylor propagator one only needs to calculate the action of the Hamiltonian on the wave function, and no inversion or diagonalization is required. The main computational expense of this algorithm, i.e. the critical operation, is the sparse matrix-vector multiplication of the Hamiltonian and the Kohn-Sham orbitals. If the TDKS equations are propagated for N_t time steps then the total number of critical operations per Kohn-Sham orbital required by the fourth-order Taylor propagation is $4N_t$.

3.2.3 Lánczos Subspace Propagation

In the Lánczos propagation scheme, one propagates the Kohn-Sham orbitals on a Lánczos subspace basis. Construction of the Lánczos basis begins by constructing a Krylov subspace of order $N_L + 1$, which is generated by repeated application of the Hamiltonian to a

Kohn-Sham orbital,

$$K_m^{N_L+1}(\phi_m, H_{\mathrm{KS}}) = span\{\phi_m, H_{\mathrm{KS}}\phi_m, H_{\mathrm{KS}}^2\phi_m, \cdots, H_{\mathrm{KS}}^{N_L}\phi_m\}. \tag{3.12}$$

We define a Krylov subspace for each Kohn-Sham orbital. The N_L+1 Lánczos vectors, q_j, are then constructed by Gram-Schmidt orthonormalizing the Krylov basis vectors.

Following the Lánczos algorithm [118], one first tridiagonalizes the Hamiltonian in the Lánczos basis. Next the tridiagonal Hamiltonian is diagonalized to obtain N_L eigenvalues, ε_i, and N_L eigenvectors, $|a_i\rangle$. We directly evaluate the propagator on the Lánczos basis through eigenvalue decomposition,

$$\exp\left[-\frac{i}{\hbar}H_{\mathrm{KS}}(t_0)\delta t\right] = \sum_{j,l=1}^{N_L}\sum_{i=1}^{N_L} |q_j\rangle \langle q_j|\, a_i\rangle\, e^{-i\varepsilon_i\delta t}\, \langle a_i|\, q_l\rangle \langle q_l|. \tag{3.13}$$

Propagation on the subspace is computationally cheap since the number of basis vectors required is small. The Kohn-Sham Hamiltonian is time dependent while the Lánczos basis and propagator are defined at a fixed time, t_0. At t_0 the Kohn-Sham orbitals and density are well represented by this relatively small basis set. As the system is time propagated the representation with this small basis will become poor, and therefore the Lánczos basis and time propagator must be periodically updated. Construction of the Lánczos basis is expensive as it requires N_L sparse matrix-vector multiplications. In practice we have found that the Lánczos basis need only be updated once every, $N_{\mathrm{update}} = 5$, time steps. The total number of critical operations per Kohn-Sham orbital required by this algorithm to propagate for N_t time steps is, $\frac{N_L \cdot N_t}{N_{\mathrm{update}}}$.

3.2.4 Adiabatic Eigenstate Subspace Propagation

For the construction of subspace propagation schemes, one of the most natural bases to consider is the eigenvectors of the time-dependent Kohn-Sham Hamiltonian matrix at some fixed time t_0. This subspace propagation method has been called the adiabatic eigenstate

method[107] and the spectral basis method [106] in the literature. We begin by constructing the subspace basis vectors, $q_j(t_0)$, using the conjugate-gradient diagonalization method. In this case we diagonalize the Hamiltonian at time, t_0,

$$H_{KS}(t_0)\left|q_j(t_0)\right\rangle = \varepsilon_j(t_0)\left|q_j(t_0)\right\rangle, \tag{3.14}$$

and choose the N_e eigenvectors with lowest eigenvalues, $\varepsilon_j(t_0)$. The algorithm for diagonalization shall be described at the end of this section. We then propagate the Kohn-Sham orbitals on this subspace for N_{update} time steps using the Crank-Nicholson propagator,

$$\hat{U}(t,t+\delta t) = \left(\hat{I}+\frac{i\delta t}{2\hbar}\hat{H}_{KS}(t)\right)^{-1}\left(\hat{I}-\frac{i\delta t}{2\hbar}\hat{H}_{KS}(t)\right), \tag{3.15}$$

where $\hat{H}_{KS}(t) = \langle q_i(t_0)|\, H_{KS}(t)\left|q_j(t_0)\right\rangle$. Since the Crank-Nicholson operator is unitary, the norm of each Kohn-Sham orbital is preserved with each propagation step. We apply this propagator to the Kohn-Sham orbitals N_{update} times. As with the Lánczos basis, the subspace calculated at t_0 becomes unsuitable with time. We therefore reconstruct the subspace basis and recalculate the propagator once every N_{update} time steps. It was found that much larger values of, $N_{\text{update}} = 20-30$, gave accurate propagation.

To improve the computational efficiency, we split the Hamiltonian into a stationary matrix and a dynamic matrix,

$$\hat{H}_{stationary} = \sum_{j=1}^{M}\left|q_j(t)\right\rangle \varepsilon_j(t)\left\langle q_j(t)\right| - \hat{H}_{dynamic} \tag{3.16}$$

$$\hat{H}_{dynamic} = \sum_{i,j=1}^{M}\left|q_i(t)\right\rangle \left\langle q_i(t)\right| V_{Hxc}\left|q_j(t)\right\rangle \left\langle q_j(t)\right|. \tag{3.17}$$

The stationary matrix is only updated every N_{update} time steps. The calculation of V_{Hxc}, and hence of the dynamic matrix, is inexpensive and therefore updated every time step.

We shall now describe the construction of the eigenbasis at time, $t_0 + N_{\text{update}}\delta t$, given

the eigenbasis at time, t_0. In the conjugate-gradient method, the eigenvectors of $H(t_0 + N_{\text{update}}\delta t)$ are produced iteratively from an initial trial vector. In this case the initial trial for $q_j(t_0 + N_{\text{update}}\delta t)$ is $q_j(t_0)$. The critical operation for the conjugate-gradient method is the application of the Hamiltonian, H_{KS}, to the trial vectors. In our implementation we begin the diagonalization process with 4 conjugate-gradient iterations, requiring a total of $5 \cdot N_e$ sparse matrix-vector multiplications. After these 4 iterations, the basis is orthonormalized using the Gram-Schmidt procedure. In our testing the Gram-Schmidt orthonormalization of N_e vectors requires a computational expense on the same order as N_e sparse matrix-vector multiplications, and we therefore include this operation in our algorithm analysis. The conjugate-gradient-Gram-Schmidt procedure is then repeated 3 times, for a total of $4 \cdot ((5+1) \cdot N_e) = 24 \cdot N_e$ critical operations. In our testing, the combination of 4 conjugate-gradient iterations and 3 conjugate-gradient-Gram-Schmidt procedures offers a reasonable trade off between accuracy and computational expense.

The conjugate-gradient-Gram-Schmidt iterations yields a set of vectors, $q'_j(t_0 + N_{\text{update}}\delta t)$. In the next step of the algorithm we construct the reduced Hamiltonian,

$$\hat{H}_{ij}(t_0 + N_{\text{update}}\delta t) = \left\langle q'_j(t_0 + N_{\text{update}}\delta t) \right| H_{KS}(t_0 + N_{\text{update}}\delta t) \left| q'_i(t_0 + N_{\text{update}}\delta t) \right\rangle, \quad (3.18)$$

requiring an additional N_e sparse matrix-vector multiplications. The reduced Hamiltonian, which has size $N_e \times N_e$, is then diagonalized using the DSYGVX function in the LAPACK library for FORTRAN, yielding N_e eigenvectors, v_j. This diagonalization step is of minimal cost since the dimension of the reduced Hamiltonian is small. The final set of adiabatic eigenbasis vectors is defined as, $\left| q_j(t_0 + N_{\text{update}}\delta t) \right\rangle = \sum_i \left\langle q'_i | v_j \right\rangle \left| q'_i \right\rangle$. Collecting the relevant contributions to the computational cost, the total number of critical operations per Kohn-Sham orbital required by this algorithm to propagate the system for N_t time steps is $\frac{25 \cdot N_e \cdot N_t}{N_{\text{update}} \cdot N_{\text{KS}}}$.

At time, $t = 0$, the initial trial vectors for the conjugate-gradient algorithm are cho-

sen arbitrarily, and a greater number of conjugate-gradient iterations is often required to construct a well converged basis set. We initialize the basis by applying the above diagonalization algorithm 10 times, for a total of $\frac{250 \cdot N_e}{N_{\mathrm{KS}}}$ critical operations per Kohn-Sham orbital. The cost of initializing the basis and propagating the system for 10 fs using various time steps is shown in Table 3.3.

The Lánczos and Eigenstate Subspace propagations are very similar. A representation approximating the lowest instantaneous eigenstates are used in both cases. The main difference is that in the Lánczos case each orbital is propagated in its own subspace, while in the case of the Eigenstate Subspace approach each orbital is time developed in the same subspace. One notes that high-order excitations are excluded by this method, implying that high-frequency oscillations will not manifest in the dynamics. This is consistent with the desired goal of constructing efficient algorithms for the solution of TDDFT in cases where the dynamics change sufficiently slowly as to be represented by long time steps.

3.3 Results and discussion

We have presented three prototypical applications of TDDFT. The first application is the optical properties of benzene, which are calculated by solving the TDKS equations with finite boundary conditions. The other two applications are nonadiabatic Ehrenfest molecular dynamics simulations of proton-benzene and proton-graphene collisions which are solved using finite and periodic boundary conditions, respectively. We consider the Lánczos and adiabatic eigenbasis propagation methods for cases which involve finite boundary conditions. For the proton-graphene collisions we consider only the Lánczos basis propagation method. In our implementation the adiabatic eigenbasis is computationally prohibitively expensive for periodic boundary conditions since the basis must be constructed separately for each k-point. The adiabatic eigenbasis might be more suitable to orbital bases. The use of an adiabatic eigenbasis with periodic boundary conditions is also investigated by Sato et al.[119], where a new efficient variant of the eigenbasis representation is proposed.

The box dimensions, grid spacing, and total propagation time of each application is given in Table 3.1. Where applicable, the initial projectile-target separation and the k-point mesh are also given. The planes of benzene and graphene are parallel to the *y*-*z* plane. The polarization vector of the linearly polarized ultrashort laser pulse is parallel to the *x* axis. The trajectory of the proton in the collision simulations is parallel to the *x* axis, and the proton's kinetic energy is 200 eV. The proton is fired through the center ring of the benzene molecule, and through a C-C bond of the graphene. The supercell in the proton-graphene collisions contains 4 carbon atoms. The parameters in each application are sufficient for the comparison of different propagation schemes as desired here. In the next subsection we show the results of the optical properties simulations, and in the following subsection we show the results of the molecular dynamics simulations.

Application	L_x (Å)	L_y (Å)	L_z (Å)	Δx (Å)	K-Points	Time (fs)	Initial Separation (Å)
Benzene Optical Properties	9.8	9.8	9.8	0.20	N/A	10	N/A
Benzene Ultrafast Laser	9.8	9.8	9.8	0.20	N/A	30	N/A
Proton-Benzene Collision	20	16.8	16.8	0.20	N/A	40	11
Proton-Graphene Collision	31.75	2.45	4.26	0.20	1x2x3	20	15.88

Table 3.1: Numerical details of the three prototypical applications of TDDFT considered. The grid spacing, Δx, is equal in each spatial direction. The k-point mesh only applies to the proton-graphene collision, where the TDKS equations are solved with periodic boundary conditions. The "Time" column refers to the total propagation time. The "Initial Separation" column refers to the initial distance between the proton projectile and the target.

3.3.1 Optical Properties

In this subsection we solve the TDKS equations with finite boundary conditions. Taylor propagation gives well converged results with a time step of 0.001 fs. Smaller time steps yield negligible differences in the computational results. We therefore use this method as a benchmark calculation to which the subspace methods are compared.

The first system under consideration is a benzene molecule driven by an initial linear perturbation, with the details outlined in section II. The plane of the molecule is aligned parallel to the *y*-*z* plane. The linear perturbation induces an excitation involving all excited

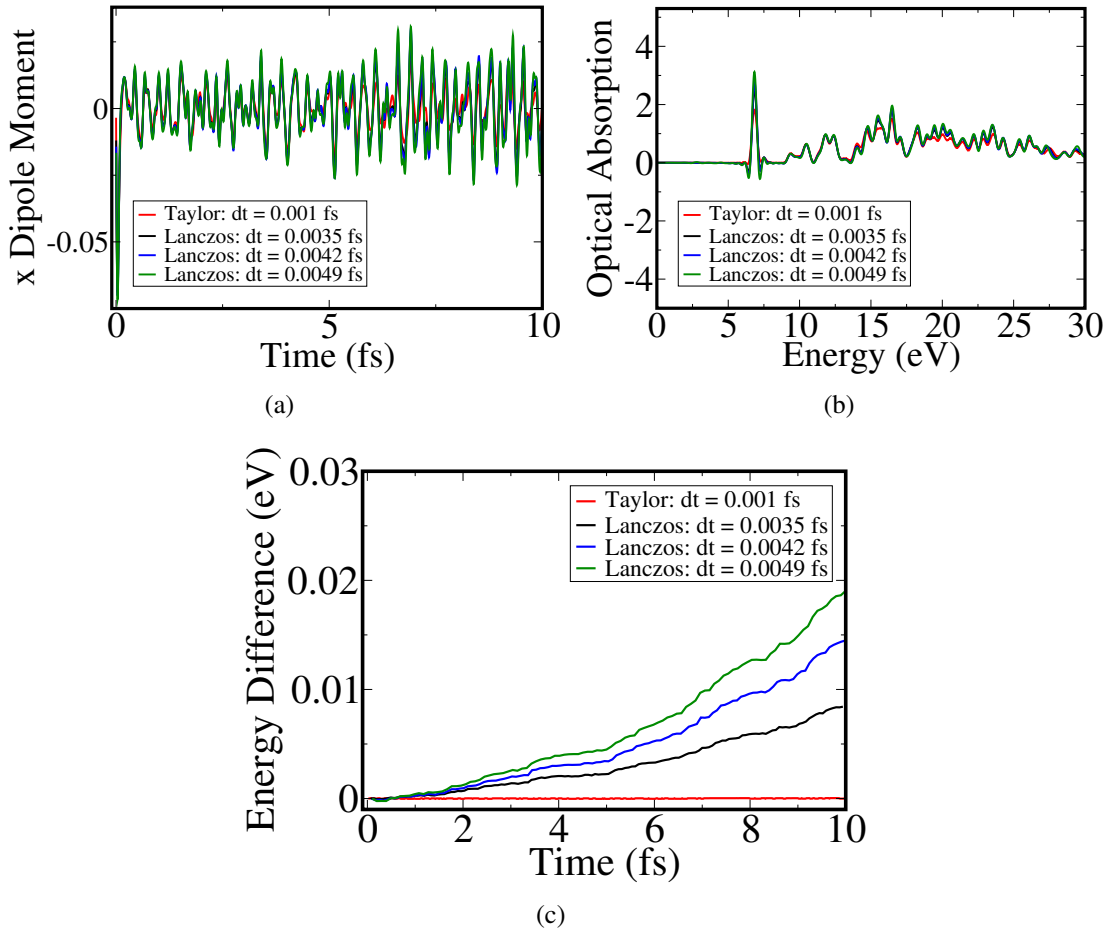

Figure 3.1: (Color online) Optical properties of benzene as calculated using the Taylor and Lánczos propagation schemes for the time dependent density functional theory code with finite boundary conditions. At time $t = 0$, a small disturbance is applied to the system. The Lánczos basis updated every 5 time steps. Plots (a) show the dipole moment induced along the axis perpendicular to the plane of the molecule (x axis) when the perturbation is also applied in the x axis. Plots (b) show the optical absorption calculated by averaging the Fourier transform of the induced dipole of each spatial coordinate. Plots (c) show the change in total energy in the case where the dipole-perturbation is applied along the x direction.

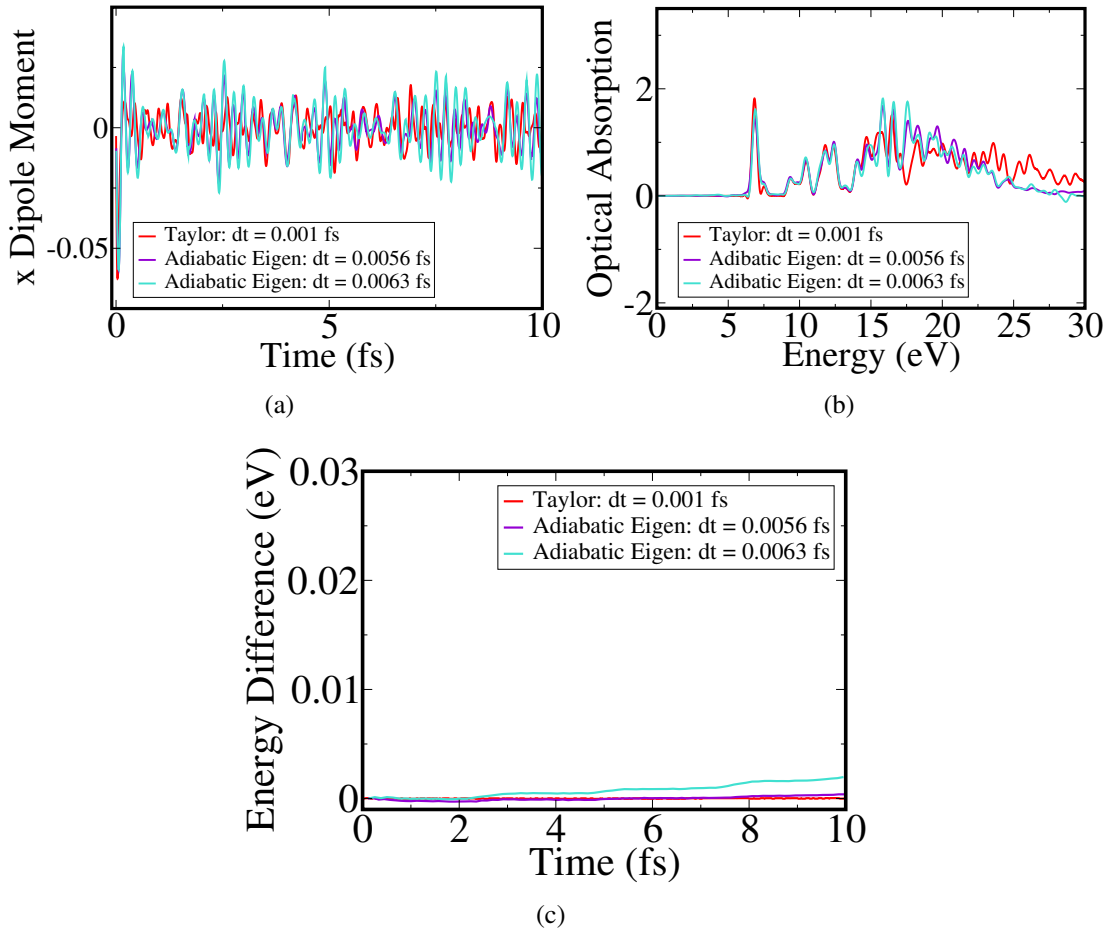

Figure 3.2: (Color online) Optical properties of benzene as calculated using the Taylor and adiabatic eigenbasis propagation schemes for the time dependent density functional theory code with finite boundary conditions. At time $t = 0$, a small disturbance is applied to the system. The adiabatic eigenbasis is updated every 30 time steps. Plots (a) show the dipole moment induced along the axis perpendicular to the plane of the molecule (x axis) when the perturbation is also applied in the x axis. Plots (b) show the optical absorption calculated by averaging the Fourier transform of the induced dipole of each spatial coordinate. Plots (c) show the change in total energy in the case where the dipole-perturbation is applied along the x direction.

Method	Time step (fs)	f strength	% Difference
Taylor	0.001	1.2286	0
Lánczos	0.0035	1.2348	0.5
Lánczos	0.0042	1.2442	1.3
Lánczos	0.0049	1.2102	1.5
Adiabatic	0.0056	1.3384	8.9
Adiabatic	0.0063	1.3088	6.5

Table 3.2: Comparison of the f strength of the $\pi - \pi^*$ excitation of benzene for the Taylor, Lánczos, and Eigenvector Decomposition propagation schemes. The $\pi - \pi^*$ excitation corresponds to the peak in the absorption spectrum centered at ≈6.9 eV (see Fig. 3.1 and Fig. 3.2). The percent difference in the f strength between the subspace methods and the Taylor benchmark is also calculated. In each case the f strength is within 10% of the Taylor benchmark, indicating that the subspace propagations are well converged.

states of the molecule. We perform this calculation three times, once for each spatial coordinate. We then calculate the dipole moment along the direction in which the perturbation is applied, d_x, d_y, and d_z. The absorption strength distribution for each dipole moment is calculated as,

$$S_i(E) = \frac{1}{2\pi^2 \varepsilon_0 a_0 f} E \int_0^{t_{\max}} e^{iEt/\hbar} d_i(t) g(t) dt, \quad i = x, y, z, \tag{3.19}$$

where $t_{\max}$ is the final time, ε_0 is the permittivity of free space, a_0 is the Bohr radius, and f is the strength of the applied linear perturbation [see Eq. (3.5)]. $g(t) = 1 - 3\left(\frac{t}{t_{\max}}\right)^2 + 2\left(\frac{t}{t_{\max}}\right)^3$ is a broadening factor. The absorption strength distribution is the average of the three spatial directions, $S(E) = (S_x + S_y + S_z)/3$.

For the Lánczos scheme, we have found that a reasonable trade off between physical accuracy and computational efficiency by updating the Lánczos basis once every, $N_{\text{update}} = 5$, time steps. The number of Lánczos basis vectors is, $N_L = 30$. In Fig. 3.1.a and 3.1.b, we have shown the dipole moment and optical absorption for three time steps, 0.0035 fs,

0.0042 fs, and 0.0049 fs. We also show the benchmark Taylor propagation for comparison. The frequency of the oscillations in the dipole moment follow the Taylor benchmarks for all three time steps, while the amplitude diverges as the time step increases. After the initial perturbation is applied the total energy should be conserved. The difference between the energy at time, t, and the initial energy is plotted in Fig. 3.1.c. Energy conservation remains valid throughout the propagation within 0.02 eV. One notes that the intial total energy is slightly different depending on the choice of basis, because the resolution of the initial perturbation is basis dependent.

The physical quantity which is accessible by experiment is the optical absorption. Up to a time step of 0.0049 fs, the optical absorption [see Eq. (3.19)] is well produced by the Lánczos scheme. In particular, the peaks in the spectrum are very well aligned. We note that despite the good agreement for most energies, there are negative values in the absorption spectrum at energies of $\approx$9.73 eV and $\approx$10.9 eV. These negative values are also in the absorption spectrum obtained with the benchmark Taylor propagation, and represent the inaccuracies related to a finite propagation time. To quantify the agreement in the optical absorption we consider the oscillator f strength of the $\pi - \pi^*$ transition, which corresponds to the peak in the spectrum centered at $\approx$6.9 eV. The f oscillator strength is the integral of the absorption strength distribution, $\int S(E)/\hbar dE$. We take 5 eV and 8.3 eV as the integration bounds. The results are shown in Table 3.2. While the amplitude of the peak increases with time step, the unphysical negative values compensate to give f strengths within 1.5% of the Taylor propagation value for each time step considered.

In Table 3.3 we have calculated the theoretical computational cost of the three propagation schemes for various time steps. The time step of 0.0049 fs gives reasonable agreement with the Taylor propagation benchmark with a speed up by a factor of 3.3.

We now consider the adiabatic eigenbasis. We have found that this basis needs to be updated infrequently relative to the Lánczos basis, and we therefore update the basis every, $N_{\text{update}} = 30$, time steps. The total number of basis vectors is, $N_e = 75$. In Fig. 3.2.a and

3.2.b we have shown the dipole moment and optical absorption spectrum for time steps of 0.0056 and 0.0063 fs. The total energy is conserved to within 0.002 eV (see Fig. 3.2.c). The optical absorption spectrum is very well reproduced for energies below ≈15 eV. Accuracy for higher energies may be found by increasing the size of the basis. For both time steps, the f strength of the $\pi - \pi^*$ transition is accurate to within 8.9%, implying a well converged calculation (see Table 3.2). A time step of 0.0063 fs gives a speedup over the Taylor benchmark by a factor of 5.1 (see Table 3.3).

3.3.2 Ultrashort Laser Pulse

In this section we consider electron dynamics of benzene driven by an ultrashort laser field solved by applying the Taylor and subspace propagation schemes to solve the time–dependent Kohn-Sham equations with finite boundary conditions. $N_L = 30$ Lánczos basis vectors and $N_e = 75$ adiabatic eigenbasis vectors were used. The Lánczos basis is updated every $N_{\text{update}} = 5$ time steps, and the adiabatic eigenbasis is updated every $N_{\text{update}} = 20$ time steps. The wavelength of the laser field is 800 nm, the peak electric field is 1 V/Å, and the FWHM pulse width is 4.5 fs. The peak of the field occurs at $t = 20$ fs, and the polarization of the laser field is aligned along the x axis, perpendicular to the molecular axis. Fig. 3.3.a and 3.3.c show the dipole moment as calculated using the Lánczos and adiabatic eigenbasis methods, respectively. Fig. 3.3.b and 3.3.d show the change in total energy. In each plot the benchmark Taylor propagation is shown for comparison.

We begin by describing the results of the benchmark Taylor propagation. As expected, the dipole moment follows the electric field adiabatically. The change in total energy is essentially zero until ≈ 9 fs, indicating a stable propagation in an external field which is essentially zero. From $t \approx 8.7$ fs to $t \approx 22.4$ fs, an oscillatory shape is visible which is proportional to the intensity of the laser field. By the end of the simulation, the total energy has increased by $\approx 9 \cdot 10^{-5}$ eV, highlighting the excellent stability of the Taylor method.

For the Lánczos method, one observes a strong agreement of the dipole moment with

the Taylor benchmark for both time steps considered. For a time step of 0.003 fs, the total energy difference follows the Taylor benchmark with very good accuracy. By the end of the simulation, the total energy has increased by ≈ 0.0036 eV. With a time step of 0.004 fs, the total energy difference slightly overestimates the Taylor benchmark in the pulse region. From $t \approx 21.3$ fs to $t \approx 22.6$ fs the total energy difference is nearly constant since the external potential is essentially zero. However for times, $t \geq 22.6$ fs, the energy difference becomes unstable and by the end of the simulation the total energy has increased by ≈ 0.028 eV. One emphasizes that the propagation remains stable during the physically relevant time period where the external potential is nonzero ($8.7 \leq t \leq 22.4$ fs). A time step of 0.004 fs and basis updating every 5 time steps corresponds to a speed up by a factor of 2.7 over the Taylor benchmark (see Table 3.3).

The adiabatic eigenbasis method also produces a dipole moment with good agreement with the Taylor benchmark. In this case, the energy difference begins to overestimate the Taylor benchmark at ≈ 12 fs. By the end of the simulation, the total energy increases by $\approx$ 0.008 eV and ≈ 0.01 eV for time steps of 0.005 fs and 0.006 fs, respectively. In contrast to the Lánczos method, the divergences from the benchmark begin to build while the potential is nonzero, which might be a signature that a larger subspace is needed. However, with this method the total energy remains constant for times, $t \geq 22.5$ fs. The adiabatic eigenbasis method with a time step of 0.006 fs and basis updating every 20 time steps gives a speedup of 3.4 over the Taylor benchmark (see Table 3.3).

3.3.3 Ion Collisions

In this subsection we consider proton-benzene and proton-graphene collisions solved by applying the Taylor and subspace schemes. In the Ehrenfest dynamics approach, the ion dynamics are strongly coupled to the electron dynamics. The stability of the ion dynamics is therefore highly dependent on the stability of the electron propagation scheme. Ion kinematics are also a highly relevant physical quantity which is accessible by experiment[120,

121, 122], and important for the comparison of experiment and theory[48]. The proton-benzene collision is calculated by solving the TDKS with finite boundary conditions using Taylor, Lánczos basis, and adiabatic eigenbasis propagation schemes. Periodic boundary conditions are used for the proton-graphene collision.

We begin with a discussion of the proton-benzene collision. Fig. 3.4.a and 3.4.c show the position of a hydrogen ion of the benzene molecule as calculated using the Lánczos and adiabatic eigenbases methods, respectively. Fig. 3.4.b and 3.4.d show the position of a carbon ion for the two methods. The trajectories calculated using a benchmark Taylor propagation is shown in each plot. Since the colliding proton passes through the center of the bond ring the trajectories of the ions not shown are similar. $N_L = 30$ Lánczos basis vectors and $N_e = 75$ adiabatic eigenbasis vectors were used. The Lánczos basis is updated every $N_{\text{update}} = 5$ time steps, and the adiabatic eigenbasis is updated every $N_{\text{update}} = 20$ time steps. In each case small divergences from the Taylor benchmark begin to accumulate at $\approx$7 fs. The propagation remains stable in each case for up to $\approx$25. With the Lánczos method, time steps up to 0.004 fs give relatively accurate results. This corresponds to a speedup over the Taylor benchmark of 2.7 (see Table 3.3). For the adiabatic eigenbasis, time steps up to 0.006 fs gives relatively accurate results, which corresponds to a speedup of 3.4 over Taylor propagation.

In the proton-graphene collision, the proton is shot through the center of a C-C bond of the graphene. Fig. 3.5 shows the trajectory of one of the carbon ions of the C-C bond as calculated using the Lánczos basis propagation method and compares the result to a benchmark Taylor propagation. As in the finite code, $N_L = 30$ Lánczos basis vectors are used and the basis is updated every, $N_{\text{update}} = 5$, time steps. The stability of the Lánczos propagation in this case rapidly decreases with increasing time step. At $\Delta t = 0.003$ fs, the Lánczos propagation diverges from the Taylor benchmark at $\approx$13 fs and subsequently tracks the general shape of the Taylor propagation trajectory. This time step corresponds to a speedup over Taylor propagation of 2.0 (see Table 3.3). At $\Delta t = 0.004$ fs, the propagation

diverges at ≈4 fs after which the shape of the trajectory is very inaccurate.

3.4 Summary

In conclusion, we have investigated two subspace propagation methods using the Lánczos and adiabatic eigenstate bases and compared the results to a benchmark propagation using a fourth-order Taylor expansion of the time propagator. By making use of a multiscale algorithm where propagation of the orbitals is performed with small time steps and basis updating is performed on a larger time step, the computational efficiency of the subspace methods were improved over the Taylor benchmark by factors on the order of 2–3 (see Table 3.3). The Lánczos basis propagation proved to give a reasonably accurate optical absorption spectrum over the entire energy range considered, while the adiabatic eigenbasis propagation only gave accurate results at low energies. Additionally, both subspace methods gave relatively stable propagations with only minor deviations from energy conservation. In the case of benzene driven by an ultrashort laser pulse, both methods accurately reproduced the dipole moment and remained very stable. Instabilities in the Lánczos propagation scheme became apparent with large time steps and long propagation times. The adiabatic eigenbasis scheme proved stable over the full 30 fs simulation for the time steps considered. Laser pulses with short duration are important to the quantum control of chemical reactions since shorter pulses allow for more complete control over the dynamics [123]. Strong laser pulses with sub-5 fs duration are experimentally accessible and have recently been used to induce selective bond cleavage [124] and to steer dissociation channels [125, 126]. Subspace propagation may provide a computationally efficient scheme to study these physically important laser pulses where only short propagation times are necessary.

Subspace propagation of molecular dynamics simulations remained accurate and stable only on restricted femtosecond time scales. We note that this may be the result of the relatively high speed of the colliding 200 eV proton. Longer propagation times may be accessible for external potentials which change sufficiently slowly. Nevertheless one cannot

recommend a general propagation method which has both fast computational speeds and universal applicability.

The adiabatic eigenspace approaches helped to increase the time step by about a factor of five, to about 0.005 fs, which is still much smaller than the time step of 0.2-0.5 fs used in Ref.[107]. Part of the reason for this is that in Ref. [107] a linear-time-dependence approximation [127] was introduced for the time-dependent Hamiltonian. This approach allows the use of the adiabatic eigenspace and corresponding subspace propagator for longer times before the need to update the basis. This approximation may work in certain cases but we did not found it useful (accurate enough) in the present work. In our examples the Hamiltonian changes too fast and one cannot simply approximate it for much longer time steps. On the other hand, we have used long time propagations and calculated up to higher energies in the optical spectrum. For shorter times and low energies one can use longer time steps, but as our examples demonstrate, those time steps will not converge in a long time propagation. Further work is needed to explore propagation methods that preserve the accuracy and increase the efficiency of time dependent calculations.

Method	Update	Time step (fs)	Critical Operations	Theoretical Speedup
Taylor	N/A	0.001	40000	1
Lánczos	5	0.003	19998	2.00
Lánczos	5	0.0035	17136	2.33
Lánczos	5	0.004	15000	2.67
Lánczos	5	0.0042	14280	2.80
Lánczos	5	0.0049	12246	3.27
Adiabatic	20	0.005	13750	2.91
Adiabatic	20	0.006	11667	3.43
Adiabatic	30	0.0056	8692	4.60
Adiabatic	30	0.0063	7867	5.08

Table 3.3: Comparison of the computational speed of the Taylor, Lánczos, and Eigenvector Decomposition propagation schemes. The column labeled "Update" gives the number of time steps between basis updates. The number of critical operations refers to the total theoretical computational cost per Kohn-Sham orbital of propagating the system for 10 fs. The theoretical speedup is the number critical operations required by the method divided by the number of critical operations required by the benchmark Taylor propagation.

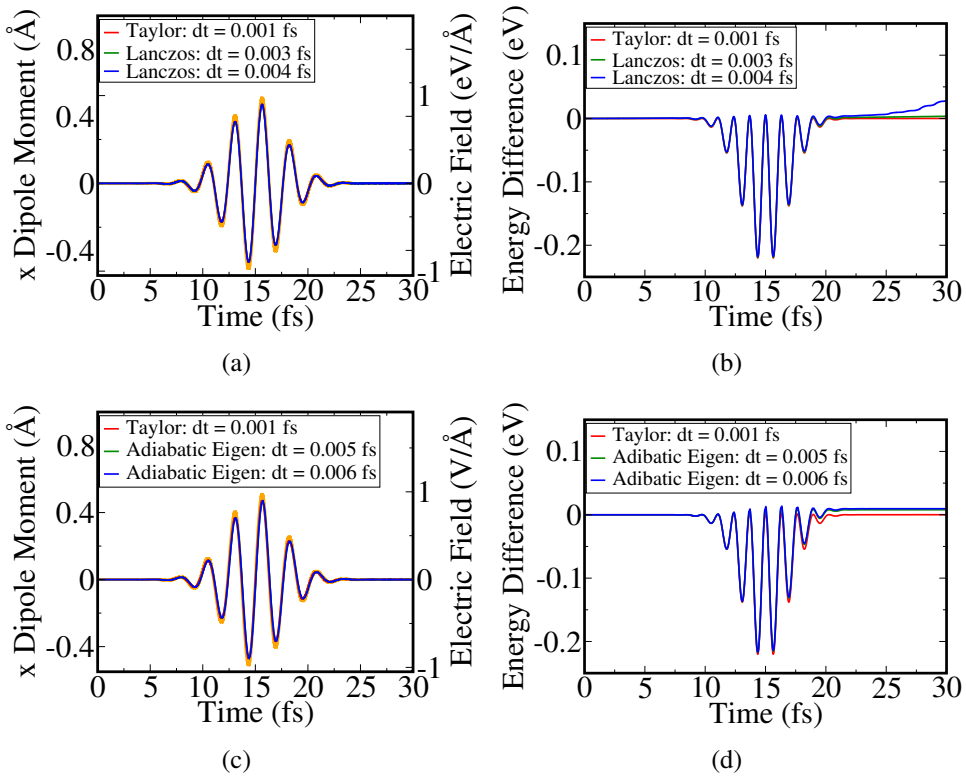

Figure 3.3: (Color online) Electronic dynamics of a benzene molecule driven by a linearly polarized ultrashort laser pulse as calculated using the Taylor, Lánczos, and adiabatic eigenbasis propagation schemes for the time dependent density functional theory code with finite boundary conditions. The wavelength of the laser field is 800 nm, the peak electric field is 1 V/Å, and the FWHM pulse width is 4.5 fs. The peak of the field occurs at $t = 20$ fs, and the polarization of the laser field is aligned along the x axis, perpendicular to the molecular axis. Plots (a-b) compare the Lánczos propagation scheme with the benchmark Taylor propagation, and plots (c-d) compare the adiabatic eigenbasis propagation scheme to the benchmark Taylor propagation for various time steps. The Lánczos basis updated every 5 time steps and the adiabatic eigenbasis is updated every 20 time steps. Plots (a) and (c) show the dipole moment induced along the x axis. The thick orange line shows the electric field of the laser pulse. Plots (b) and (e) show the change in total energy.

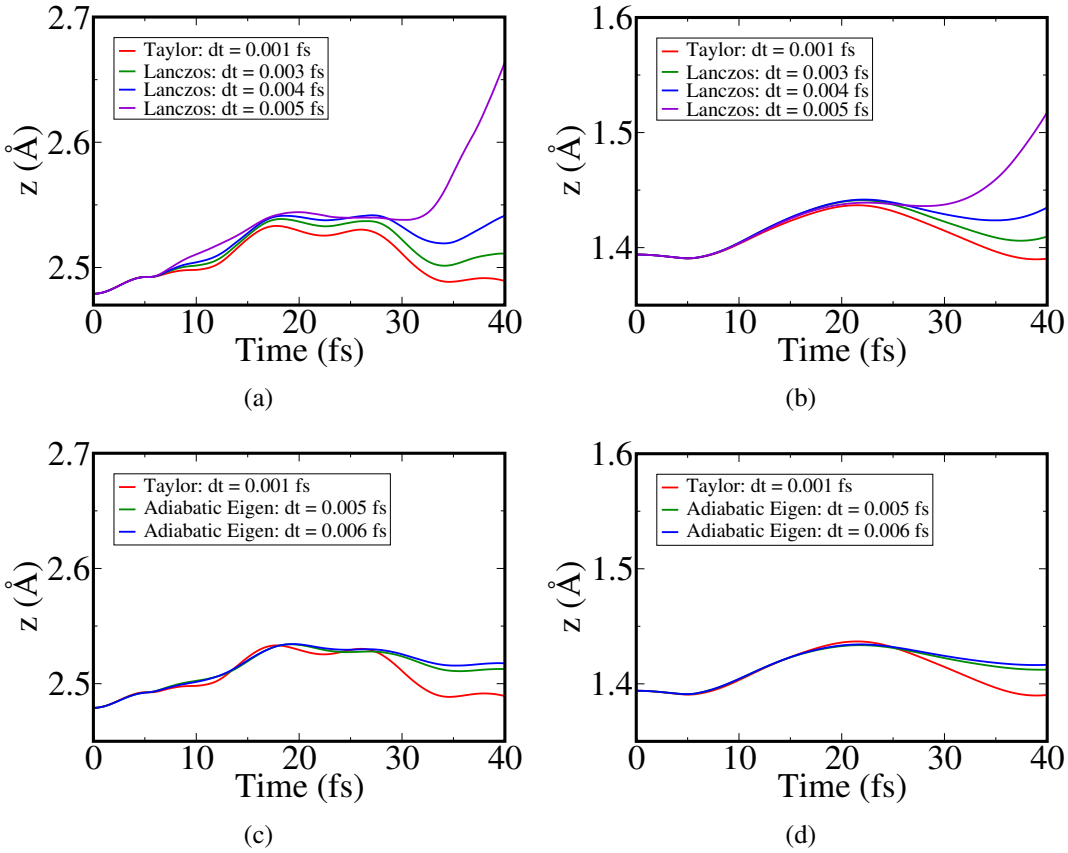

Figure 3.4: (Color online) Comparison of the Lánczos basis and adiabatic eigenbasis propagation schemes to the benchmark Taylor propagation in the case of proton collision through the center of a benzene ring. Finite boundary conditions are used. The Lánczos basis is updated every 5 time steps, and the adiabatic eigenbasis is updated every 20 time steps. The motion of the colliding proton is parallel to the x axis. The plane of the benzene molecule is parallel to the $y-z$ plane. Plots (a-b) show the trajectories of (a) a hydrogen ion and (b) a carbon ion for the Lánczos and Taylor propagations schemes, and plots (c-d) show the trajectories of (c) a hydrogen ion and (d) a carbon ion for the adiabatic eigenbasis and Taylor propagation schemes. Other ions not shown have similar trajectories.

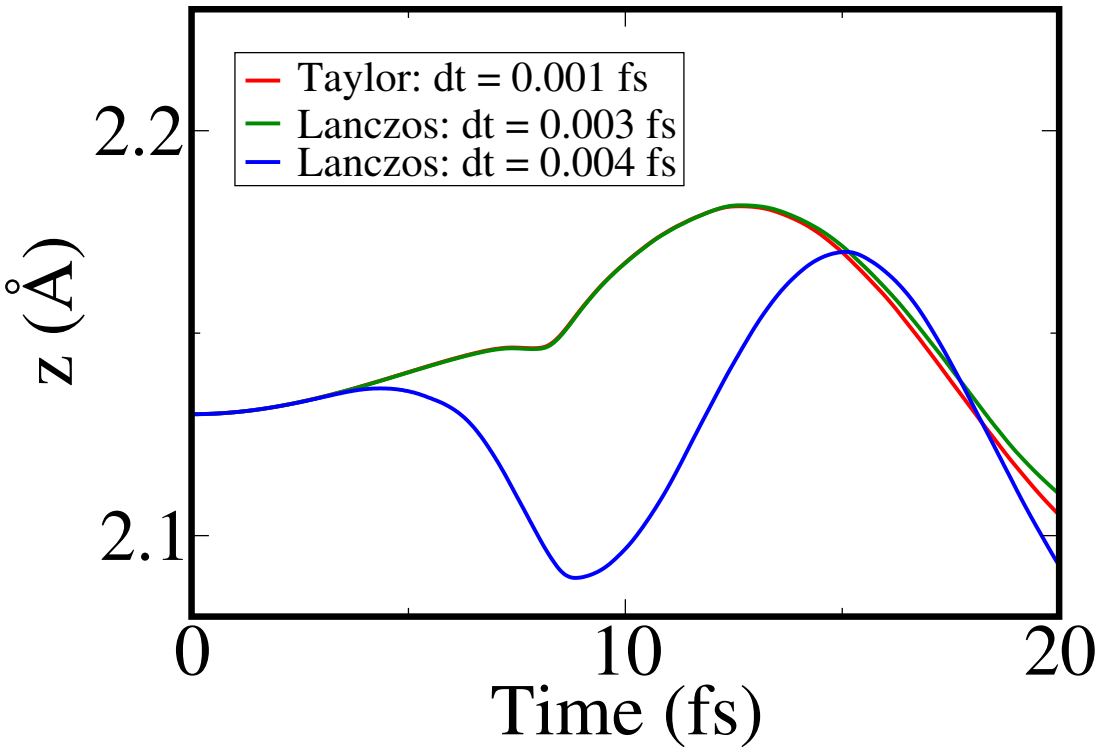

Figure 3.5: (Color online) Position of a carbon ion of graphene during a proton-graphene collision, as calculated using both the Lánczos and Taylor propagation schemes. Periodic boundary conditions are used. The proton's trajectory is perpendicular to the graphene plane and is shot through the middle of a C-C bond. The plot shows the trajectory of one of the two carbon ions of this C-C bond. The trajectory of the other carbon ion of the C-C bond is symmetric.

Chapter 4

Time Propagation Method for the Coupled Maxwell and Kohn-Sham Equations

In this chapter, An accurate method for time propagation of the coupled Maxwell and time-dependent Kohn-Sham (TDKS) equation is presented. The new approach uses a simultaneous fourth-order Runge-Kutta based propagation of the vector potential and the Kohn-Sham orbitals. The approach is compared to the conventional fourth-order Taylor propagation and predictor-corrector methods. The calculations show several computational and numerical advantages including higher computational performance, greater stability, better accuracy and faster convergence. Work shown in this chapter has been published [128].

4.1 Background

An accurate description of the interaction of electromagnetic fields and matter is an indispensable tool for understanding and predicting electric and optical properties of nanostructures. Modeling and simulation of this interaction plays a critical role in the foundation of modern electronics, information processing, and optical communications [129, 130, 131, 132, 133]. Quantum electrodynamics would, in principle, provide a complete description of these systems, but the high complexity and prohibitively large computational expense prevents its application to realistic systems. A viable alternative is the combination of nonrelativistic quantum mechanics to describe the particles and a classical treatment of the electromagnetic fields. In this semiclassical framework the electromagnetic fields are not quantized and their time evolution is governed by the Maxwell equations coupled to the quantum mechanically determined charge and current distributions of particles [134, 135, 136]. A full many-body quantum approach is not tractable for systems containing more then a few electrons, and most approaches are based on the time depen-

dent density functional theory (TDDFT) [137, 138].

Various approaches have been developed to use the coupled Schrödinger and Maxwell systems [139, 140, 141, 134, 142, 143, 144, 145, 146, 147, 148, 136, 149, 150]. In problems where the propagation of electromagnetic waves in materials is tackled, most approaches use a finite-difference time-domain solution for the electromagnetic waves and time evolution of the Schrödinger equation in real space for the electrons [147, 149]. Due to the large wavelength of the electromagnetic waves typically considered, the simulation cell has to be large and the atomistic details are suppressed. Yabana et al. [151] devised a multiscale approach where the Maxwell equations are solved on the scale of the electromagnetic wavelength and the Schrödinger equation is solved on the atomic scale using TDDFT. This approach, however, is computationally expensive and only works for certain geometries. At the same time, many problems require the treatment of the electromagnetic fields coupled to the electronic structure at the atomic scale. In this case the electromagnetic fields and the Schrödinger equation is propagated on the same time and length scale [152] which limits the applicability of this method to small simulation cells and short timescales.

In this chapter we investigate the simultaneous time propagation of the vector potential of the electromagnetic fields and the wave function describing the electrons of the system. First, we compare the accuracy and efficiency of the conventional approaches [153, 154], then we propose a new method, based on a dual Runge-Kutta approach to improve the time propagation scheme. This approach allows larger time steps and lower computational cost than previously considered propagators. We use the formalism proposed by Bertsch et al. [152]. In this approach, which has been successfully applied to various problems [153, 151, 154, 155], the time-dependent Kohn-Sham equations of TDDFT and Maxwell equations are solved on a real space grid with periodic boundary conditions. To incorporate the electromagnetic fields, the Kohn-Sham equation is coupled to the Maxwell equations by adding a vector potential $\mathrm{A}(t)$ to the linear momentum in the Kohn-Sham equation.

The plan for this chapter is as follows. In section 4.2 we present the Maxwell-TDKS

formalism and the numerical approach used. In section 4.3 we review the Taylor and predictor-corrector real-time propagation schemes. In section 4.4 we describe the proposed simultaneous fourth-order Runge-Kutta propagation method and in section 4.5 we compare the three propagation schemes. In section 4.6 we summarize the results and conclude this paper.

4.2 Maxwell-TDKS Equation With Periodic Boundary Conditions

In systems with the periodic boundary conditions the Kohn-Sham orbitals take the form of Bloch waves,

$$\psi_{ik}(\vec{r},t) = e^{i\vec{k}\cdot\vec{r}} u_{ik}(\vec{r},t), \tag{4.1}$$

with a lattice periodic spatial part, $u_{ik}(\vec{r},t)$, where i is the orbital and k is the k-vector index, and a phase factor, $e^{i\vec{k}\cdot\vec{r}}$. The Maxwell-TDKS equations can be written as,

$$i\frac{\partial}{\partial t} u_{ik}(\vec{r},t) = H_{KS}(t) u_{ik}(\vec{r},t). \tag{4.2}$$

The Kohn-Sham Hamiltonian, in atomic units, is given by,

$$\begin{aligned} H_{KS}(t)u_{ik}(\vec{r},t) &= \left[\frac{1}{2}\left(-i\nabla + \vec{k} + \vec{A}(\vec{r},t)\right)^2 + V_{Hxc}[n(\vec{r},t)](\vec{r},t)\right] u_{ik}(\vec{r},t) \\ &\quad + \int d^3\vec{r}\,' e^{-i(\vec{k}\cdot\vec{r})} v_{pp}(\vec{r},\vec{r}\,') e^{i(\vec{k}\cdot\vec{r}\,')} u_{ik}(\vec{r}\,',t), \end{aligned} \tag{4.3}$$

where, $n(\vec{r},t)$ is the electron density, $\vec{A}$ is the vector potential, V_{Hxc} is the sum of the Hartree and exchange-correlation potentials, and v_{pp} is the sum of Troullier-Martins [116] norm-conserving pseudopotentials for the ions. The time-dependent density, $n(\vec{r},t)$, is defined as

$$n(\vec{r},t) = 2\sum_{ik} |u_{ik}(\vec{r},t)|^2.$$

The Hartree potential is given by,

$$V_{\text{Hartree}} = \int \frac{n(\vec{r}\,',t)}{|\vec{r}-\vec{r}\,'|} d\vec{r}\,'. \tag{4.4}$$

The exchange-correlation potential is approximated using the adiabatic local density approximation (ALDA) with the parameterization of Perdew and Zunger [117]. The vector potential, $\vec{A} = \vec{A}_{ext} + \vec{A}_{ind}$, is a "macroscopic" quantity which is the sum of the external field, $\vec{A}_{ext}$, and the induced internal field, $\vec{A}_{ind}$. V_{Hxc} is a "microscopic" field within the unit cell.

Unlike the ordinary TDKS equations, where v_{Hxc} is the only term which depends on the time-dependent density, the vector potential in the Maxwell-TDKS equations also couples to the spatial average of the current density,

$$\frac{\partial^2 \vec{A}}{\partial t^2} = -4\pi \vec{J} = -\frac{4\pi}{\Omega} \int d\vec{r} \left[\vec{j}(\vec{r},t) + \vec{j}_{pp}(\vec{r},t) \right], \tag{4.5}$$

where $\vec{j}(\vec{r},t)$ is the normal probability current in quantum mechanics while $\vec{j}_{pp}(\vec{r},t)$ is the contribution from the non-local part of the pseudopotential as defined e.g. in [154]. Eq.4.5 is the Maxwell-equation describing the time-dependent macroscopic fields induced by the time-dependent currents.

A brief description of the numerical approach is as follows. A real space grid representation [156, 152, 157] is used to solve the TDKS equations, Eq.4.2. The kinetic energy operator is calculated using a fourth order finite-difference formula. Our test system is a diamond crystal, the same system as used by Bertsch et al. [152]. There are 8 carbon atoms in a cubic box of $L^3 = 6.73^3$ Bohr^3. The grid spacing is $\Delta x = \Delta y = \Delta z = 0.42$ Bohr. An equidistant $2 \times 2 \times 2$ and $5 \times 5 \times 5$ k-point meshes are used. While these meshes may be too small for calculations that can be compared experiments, these k point grids are sufficient for the test of different approaches.

At the beginning of the calculation, the ground-state Kohn-Sham orbitals of the un-

perturbed system are obtained by solving the time-independent Kohn-Sham equations of density functional theory (DFT). Next the system is perturbed by an instantaneous electric field, $\vec{E}(t)$, in a form of a delta-function kick at time, $t = 0$,

$$\vec{E}(t) = -\frac{d\vec{A}_{ext}}{dt} = -A_0\delta(t)\vec{e}_z, \tag{4.6}$$

where $A_0 = 0.01$ a.u. is the strength of the perturbation and $\vec{e}_z$ is the unit vector pointing to the z direction. This gives an initial condition for the vector potential,

$$\vec{A}(t=0) = A_0\vec{e}_z.$$

The Kohn-Sham orbitals are then propagated in real time. In this paper we consider three propagation algorithms: fourth-order Taylor propagation (Algorithm 1), predictor-corrector (PC) (Algorithm 2), and simultaneous fourth-order Runge-Kutta (SRK4) (Algorithm 3).

4.3 Time Propagation of the Maxwell-TDKS equation

In the fourth-order Taylor propagation, the Kohn-Sham orbitals are propagated as,

$$u_{ik}(\vec{r},t+\Delta t) = \sum_{n=0}^{4}\frac{1}{n!}\left(-\frac{i\Delta t}{\hbar}H_{KS}(t)\right)^n u_{ik}(\vec{r},t). \tag{4.7}$$

This is a conditionally stable propagation scheme. It has proved to be very accurate in many applications [43, 44, 45, 46, 48, 49, 50, 51, 59, 52, 53] provided that the time step is sufficiently small.

If one propagates the Kohn-Sham orbitals using the Taylor approach but without including the induced vector potential, the largest time step one may use to obtain well converged results is $\Delta t_0 = 0.04$ a.u. (0.001 fs). V_{Hxc} is a slowly changing quantity which can be treated as a constant during each step of the propagation. In this case the most expensive opera-

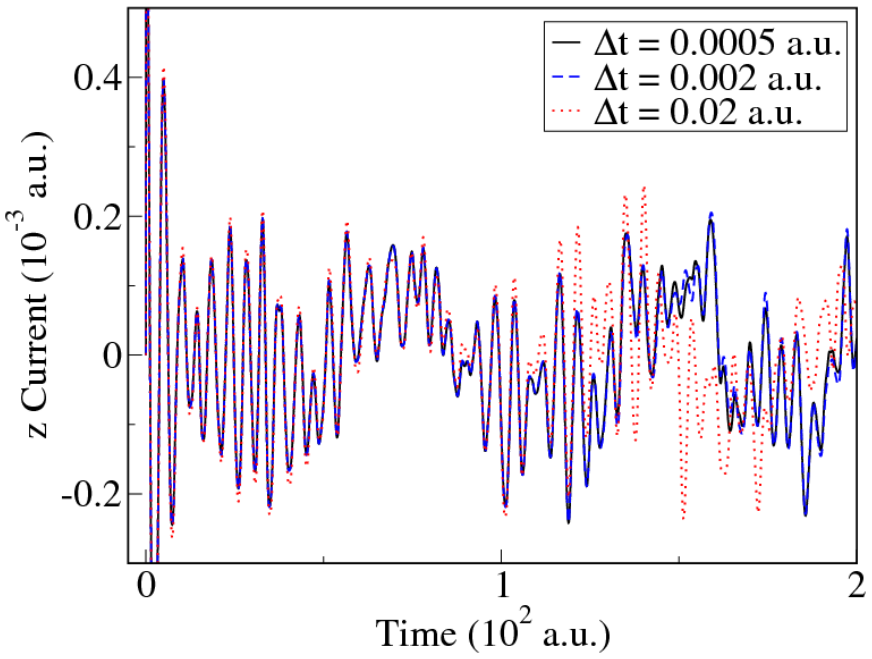

(a)

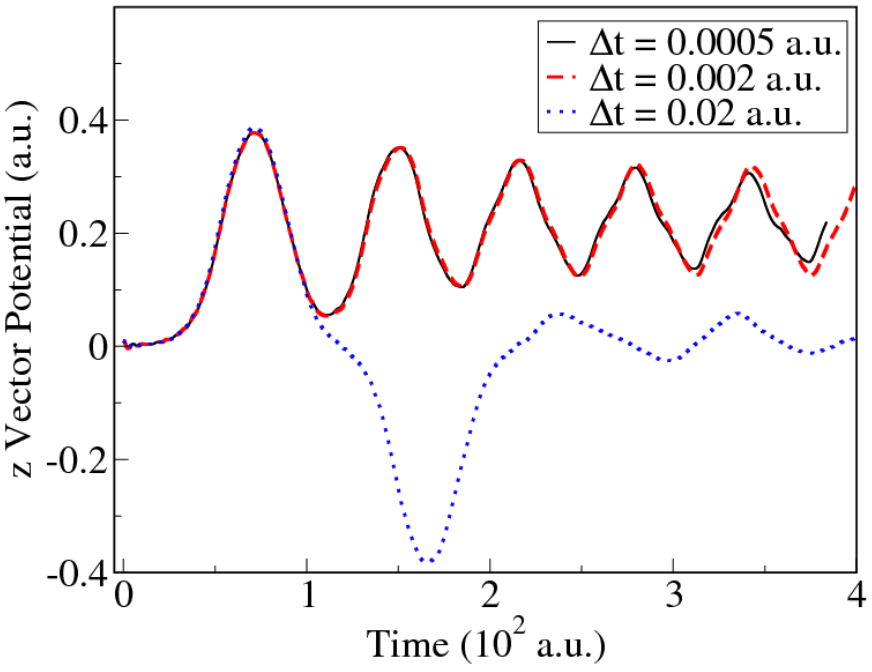

(b)

Figure 4.1: (Color online) (a) Current and (b) vector potential in the z direction in a diamond crystal induced by a delta kick applied in the z direction. A $2 \times 2 \times 2$ k-point mesh is used. The Kohn-Sham orbitals are propagated with the Taylor propagation scheme (Algorithm 1) for times up to 400 a.u. Current plotted only up to 200 a.u. Well converged results are obtained for time steps $\Delta t \leq 0.002$ a.u.

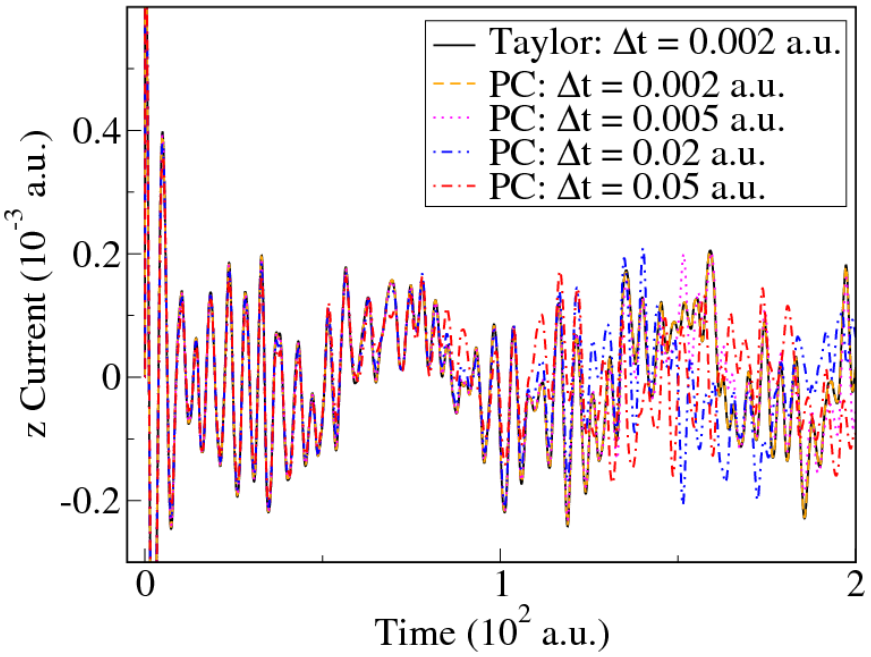

(a)

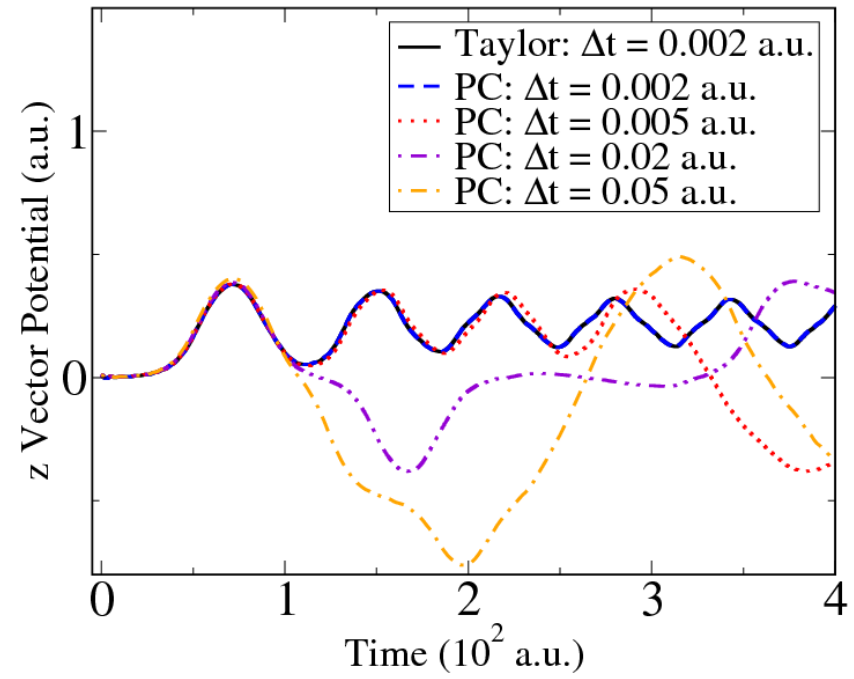

(b)

Figure 4.2: (Color online) (a) Current and (b) vector potential in the z direction in a diamond crystal induced by a delta kick applied in the z direction. A $2 \times 2 \times 2$ k-point mesh is used. The Kohn-Sham orbitals are propagated with the predictor-corrector propagation scheme (Algorithm 2) for times up to 400 a.u. Current plotted only up to 200 a.u. The propagation only remains stable for very small time steps, $\Delta t \leq 0.002$ a.u., with the Taylor benchmark and PC method exactly overlapping.

tion of the calculation is the application of the Kohn-Sham Hamiltonian to the Kohn-Sham orbitals. The commonly used fourth-order Taylor propagator requires four of these sparse matrix-vector operations per Kohn-Sham orbital.

To include the induced current and vector potential, one must propagate the Maxwell-TDKS equations simultaneously. We begin by investigating the simple propagation algorithm shown in Algorithm 1. In this algorithm the Kohn-Sham orbitals are time developed using Taylor propagation and the vector potential is updated using a finite-difference representation of the second derivative. Since the second derivative of the vector potential is related to the current (see Eq.4.5), the vector potential is very sensitive to small changes in current. This makes the simultaneous solution of the TDKS and Maxwell-equations more challenging. The induced vector potential changes more rapidly than V_{Hxc}. If a time step on the same order as $\Delta t_0 = 0.04$ a.u. is applied to the Maxwell-TDKS equations using Algorithm 1, the calculation diverges. For example, a time step of $\Delta t_T = 0.02$ a.u. leads to a divergence at 100 a.u. (2 fs) as shown in Fig. 4.1. Reducing the time step to $\Delta t_T = 0.002$ a.u. gives well converged results. However, this time step is computationally prohibitively expensive (see Table 4.1). Fig. 4.1 shows that the divergence does not occur at the beginning of the calculation. This makes it difficult to select a proper time step for the Taylor propagator.

Algorithm 1 Taylor Method for the Maxwell-TDKS equation

procedure TAYLOR1STEP($n(\vec{r},t)$, $\{\psi_{ik}(\vec{r},t)\}$, $\vec{A}(t)$, $\vec{A}(t-\Delta t)$) ▷ The initial condition

$V_{Hxc}(\vec{r}) \leftarrow$ COMPUTEVHXC($n(\vec{r},t)$)

$\{\psi_{ik}(\vec{r},t+\Delta t)\} \leftarrow$ TAYLORPROPAGATOR1STEP($\{\psi_{ik}(\vec{r},t)\}$, $\vec{A}(t)$, $V_{Hxc}(\vec{r})$) ▷ 4th order expansion

$\vec{J} \leftarrow$ COMPUTECURRENT($\{\psi_{ik}^{pred}(\vec{r})\}$)

$\vec{A}(t+\Delta t) \leftarrow 2\vec{A}(t) - \vec{A}(t-\Delta t) + (-4\pi)\vec{J}\Delta t^2$

end procedure

To alleviate this problem, the PC method was introduced and has been used in many

applications [152, 158, 153]. The PC algorithm is summarized in Algorithm 2. A typical PC method requires two Taylor propagations, and hence 8 applications of the Hamiltonian to each Kohn-Sham orbital.

We use the well converged result of Algorithm 1 with $\Delta t_T = 0.002$ a.u. as a benchmark calculation. In Fig. 4.2, we calculate the current density and induced vector potential using the PC method and compare to the benchmark. We have found that a time step of $\Delta t_{PC} = 0.005$ a.u. yields a stable propagation within 200 a.u. (5 fs). With larger time steps the results diverge more quickly.

Algorithm 2 PC Method with Taylor Propagator

procedure PREDICTORCORRECTOR1STEP($n(\vec{r},t)$, $\{\psi_{ik}(\vec{r},t)\}$, $\vec{A}(t)$, $\vec{A}(t-\Delta t)$) ▷ The initial condition

$V_{Hxc}(\vec{r}) \leftarrow$ COMPUTEVHXC($n(\vec{r},t)$) ▷ predict stage

$\{\psi_{ik}^{pred}(\vec{r})\} \leftarrow$ TAYLORPROPAGATOR1STEP($\{\psi_{ik}(\vec{r},t)\}$, $\vec{A}(t)$, $V_{Hxc}(\vec{r})$)

$n^{pred}(\vec{r}) \leftarrow$ COMPUTEDENSITY($\{\psi_{ik}^{pred}(\vec{r})\}$)

$V_{Hxc}^{pred}(\vec{r}) \leftarrow$ COMPUTEVHXC($n^{pred}(\vec{r})$)

$\vec{J} \leftarrow$ COMPUTECURRENT($\{\psi_{ik}^{pred}(\vec{r})\}$)

$\vec{A}^{pred} \leftarrow 2\vec{A}(t) - \vec{A}(t-\Delta t) + (-4\pi)\vec{J}\Delta t^2$

$V_{Hxc}^{corr}(\vec{r}) \leftarrow \frac{1}{2}(V_{Hxc}^{pred} + V_{Hxc})$ ▷ correct stage

$\vec{A}^{corr} \leftarrow \frac{1}{2}(\vec{A}^{pred} + \vec{A}(t))$

$\{\psi_{ik}(\vec{r},t+\Delta t)\} \leftarrow$ TAYLORPROPAGATOR1STEP($\{\psi_{ik}(\vec{r},t)\}$, $\vec{A}^{corr}$, $V_{Hxc}^{corr}(\vec{r})$) ▷ real propagation

$n(\vec{r},t+\Delta t) \leftarrow$ COMPUTEDENSITY($\{\psi_{ik}(\vec{r},t+\Delta t)\}$)

$\vec{J} \leftarrow$ COMPUTECURRENT($\{\psi_{ik}(\vec{r},t+\Delta t)\}$)

$\vec{A}(t+\Delta t) \leftarrow 2\vec{A}(t) - \vec{A}(t-\Delta t) + (-4\pi)\vec{J}\Delta t^2$

end procedure

4.4 Simultaneous Runge-Kutta Time Propagation

While the PC method is a popular approach, it is neither a standard "multi-step" or a "multi-value" differential equation solver [159]. As shown in the previous section, when the induced vector potential is included the PC method leads to numerical instabilities unless a very small time step is used. We propose a Runge-Kutta (RK) based approach as a new propagation method. Compared to the PC method, the RK approach allows for stable propagation with larger time steps and less computational cost per time step.

For convenience we begin by rewriting the Maxwell-TDKS equations as first-order differential equations in time,

$$\frac{\partial u_{ik}(\vec{r},t)}{\partial t} = -iH_{KS}(t)u_{ik}(\vec{r},t) \tag{4.8}$$

$$\frac{d\dot{\vec{A}}(t)}{dt} = -4\pi\vec{J}, \tag{4.9}$$

where $\dot{\vec{A}}(t)$ is the first-order time derivative of the vector potential $\vec{A}(t)$. With both equations in the form,

$$\frac{dy}{dt} = f(t,y),$$

one may use the fourth-order Runge-Kutta method (RK4) propagate ψ_{ik} and $\dot{\vec{A}}$ simultaneously. The Runge-Kutta method updates the equations as follows [159]:

$$y(t+\Delta t) = y(t) + \frac{\Delta t}{6}(k_1 + k_2 + k_3 + k_4),$$

where,

$$
\begin{aligned}
k_1 &= f(t, y(t)) \\
k_2 &= f(t + \frac{\Delta t}{2}, y(t) + k_1 \frac{\Delta t}{2}) \\
k_3 &= f(t + \frac{\Delta t}{2}, y(t) + k_2 \frac{\Delta t}{2}) \\
k_4 &= f(t + \Delta t, y(t) + k_3 \Delta t).
\end{aligned}
$$

By substituting the density, the vector potential and the wave functions, one evaluates the time derivative of the wave functions; one also evaluates the derivative of $\dot{\vec{A}}$ with the averaged current calculated out of the wave functions. The two derivatives can be used to construct the RK4 algorithm.

The simultaneous RK4 (SRK4) algorithm provides $\psi_{ik}(\vec{r}, t + \Delta t)$ and $\dot{\vec{A}}(t + \Delta t)$, but not the vector potential directly. The last piece of the algorithm is the calculation of the vector potential. One possibility for evaluation of the vector potential is a simple finite-difference formula,

$$
\vec{A}(t + \Delta t) \approx 2\vec{A}(t) - \vec{A}(t - \Delta t) + \Delta t^2 \ddot{\vec{A}}(t), \tag{4.10}
$$

as it has been used in Algorithms 1 and 2, but this implementation uses two previous time steps. Considering that the RK4 algorithm is the algorithm depends only on the previous step, the Euler method is a more suitable approach.

$$
\vec{A}(t + \Delta t) \approx \vec{A}(t) + \Delta t \dot{\vec{A}}(t). \tag{4.11}
$$

To obtain the same order of accuracy as eq.4.10, one can expand the vector potential at $t + \Delta t/2$ with a Taylor expansion in two ways as

$$
\begin{aligned}
\vec{A}(t + \frac{\Delta t}{2}) &= \vec{A}(t) + \frac{\Delta t}{2} \dot{\vec{A}}(t) + \frac{\Delta t^2}{8} \ddot{\vec{A}}(t) + O(\Delta t^3) \\
\vec{A}(t + \frac{\Delta t}{2}) &= \vec{A}(t + \Delta t) - \frac{\Delta t}{2} \dot{\vec{A}}(t + \Delta t) + \frac{\Delta t^2}{8} \ddot{\vec{A}}(t + \Delta t) + O(\Delta t^3).
\end{aligned} \tag{4.12}
$$

Subtracting these two equations and dropping the $O(\Delta t^3)$ terms allows one to evaluate $A(t+\Delta t)$ using only one previous time step,

$$\vec{A}(t+\Delta t) \approx \vec{A}(t) + \frac{\Delta t}{2}\left[\dot{\vec{A}}(t) + \dot{\vec{A}}(t+\Delta t)\right] + \frac{\Delta t^2}{8}\left[\ddot{\vec{A}}(t) - \ddot{\vec{A}}(t+\Delta t)\right]. \tag{4.13}$$

Eq.4.13 gives the vector potential with the desired $O(\Delta t^2)$ accuracy. We will use this expression in the RK4 algorithm for consistent formulation and easy implementation.

By combining the SRK4 and one of the equation for the evaluation of the vector potential, one obtains the approach summarized in Algorithm 3.

Algorithm 3 Simultaneous Runge-Kutta Method (4th order)

procedure SIMULTANEOUSRUNGEKUTTA1STEP($n(\vec{r},t)$, $\{\psi_{ik}(\vec{r},t)\}$, $\vec{A}(t)$, $\dot{\vec{A}}(t)$) ▷ The initial condition

$c^{rk} \leftarrow \{1, \frac{1}{2}, \frac{1}{2}, 1\}$

for $m \leftarrow 1,2,3,4$ **do** ▷ Runge-Kutta stages

if $m = 1$ **then**

$\{\psi_{ik}^{rk}(\vec{r})\} \leftarrow \{\psi_{ik}(\vec{r},t)\}$

$\dot{\vec{A}}^{rk} \leftarrow \dot{\vec{A}}(t)$

else

$\{\psi_{ik}^{rk}(\vec{r})\} \leftarrow \{\psi_{ik}(\vec{r},t)\} + \Delta t\, c_m^{rk}\, \{k_{m-1}(\psi)\}$

$\dot{\vec{A}}^{rk} \leftarrow \dot{\vec{A}}(t) + \Delta t\, c_m^{rk}\, k_{m-1}(\dot{\vec{A}})$

end if

$\vec{J} \leftarrow$ COMPUTECURRENT($\{\psi_{ik}^{rk}(\vec{r})\}$)

$k_m(\dot{\vec{A}}) \leftarrow \dot{\vec{A}}(t) + \Delta t(-4\pi\vec{J})$

$\vec{A}^{rk} \leftarrow \vec{A}(t) + \Delta t\dot{\vec{A}}(t)$ ▷ can be replaced by Equation 4.10 or 4.13

$\{k_m(\psi)\} \leftarrow -iH\left[n(\vec{r},t), \vec{A}^{rk}\right]\{\psi_{ik}^{rk}(\vec{r})\}$

end for

$\{\psi_{ik}(\vec{r},t+\Delta t)\} \leftarrow \{\psi_{ik}(\vec{r},t)\} + \frac{\Delta t}{6}\left[\{k_1(\psi)\} + 2\{k_2(\psi)\} + 2\{k_3(\psi)\} + \{k_4(\psi)\}\right]$

$\dot{\vec{A}}(t+\Delta t) \leftarrow \dot{\vec{A}}(t) + \frac{1}{6}\left[k_1(\dot{\vec{A}}) + 2k_2(\dot{\vec{A}}) + 2k_3(\dot{\vec{A}}) + k_4(\dot{\vec{A}})\right]$

$\vec{J} \leftarrow$ COMPUTECURRENT($\{\psi_{ik}(\vec{r},t+\Delta t)\}$)

$\vec{A}(t+\Delta t) \leftarrow \vec{A}(t) + \Delta t\dot{\vec{A}}(t)$ ▷ can be replaced by Equation 4.10 or 4.13

$n(\vec{r},t+\Delta t) \leftarrow$ COMPUTEDENSITY($\{\psi_{ik}(\vec{r},t+\Delta t)\}$)

end procedure

Unlike the PC method, which only updates the vector potential once, there are multiple updates of the vector potential in the SRK4 algorithm. This results in a better approximation of the vector potential. As for the computational cost, the SRK4 approach requires only 4 applications of the Hamiltonian to each Kohn-Sham orbital per time step. In practice, we

have found that the cost of the evaluation of the current in SRK4 is comparably expensive to these sparse matrix-vector multiplications, and include this cost in our algorithm analysis. We therefore find that the cost of SRK4 is only slightly lower than that of the PC method (see Table 4.1) if the same time step is used. As we will show in the next section, the real advantage of the SRK4 method is that a time step of, Δt_{SRK4}=0.05 a.u. (0.0012 fs), gives well converged results. This time step is comparable to Δt_0=0.04 a.u., the maximum allowed time step for the Taylor propagation of the TDKS without coupling to the Maxwell-equations.

4.5 Numerical Examples Using the SRK4 Method

In this section we present numerical examples to show the computational efficiency and accuracy of the SRK4 approach. The system investigated is a diamond crystal perturbed by a delta-kick (as described in section II). There are 32 electrons per unit cell with 16 Kohn-Sham orbital doubly occupied for the ground state. The ground state density is shown in Fig. 4.3 (a) and a typical ground state population evolution in the excitation is shown in Fig. 4.3 (b).

In Fig. 4.4 we have compared the PC method with a time step of $\Delta t_{PC} = 0.02$ a.u. to SRK4 with a time step of, $\Delta t_{SRK4} = 0.05$ a.u. The Kohn-Sham orbitals are propagated for, T=400 a.u. The PC and SRK4 calculations are compared to a well converged benchmark Taylor propagation (Algorithm 1) with time step, $\Delta t_T = 0.002$ a.u. Over the course of the simulation errors in the PC method accumulate, leading the current, vector potential and energy to diverge compared to the benchmark. The error of the energy accumulates at a very early time (about 50 a.u.). The SRK4 method remains stable and accurate for the whole duration.

This simple benchmark on a $2 \times 2 \times 2$ k-point mesh provides a quick test of the SRK4 algorithm. In practice, a more dense k-point mesh is required for comparison with experiments. In Fig. 4.5 we show the current and vector potential of a diamond crystal with a

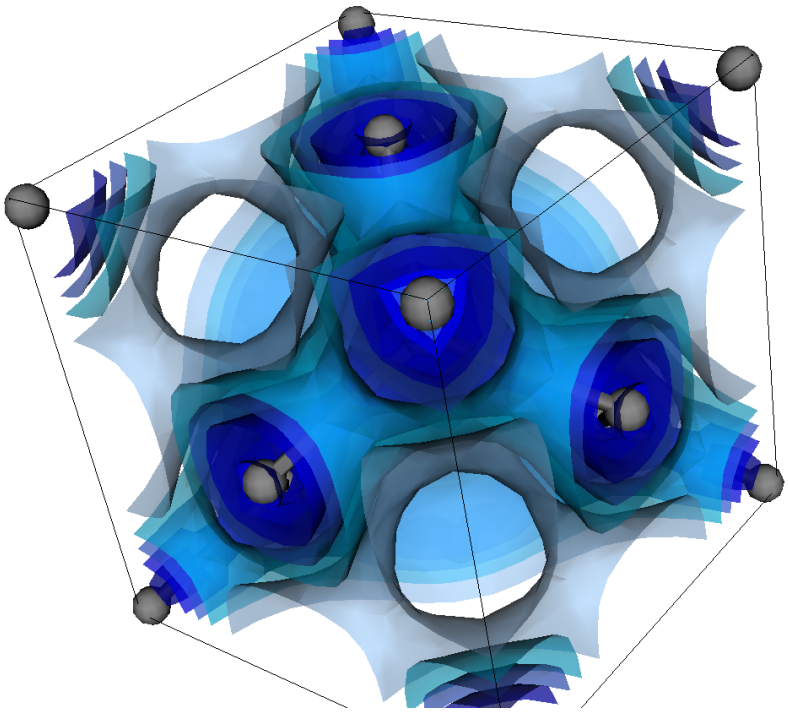

(a)

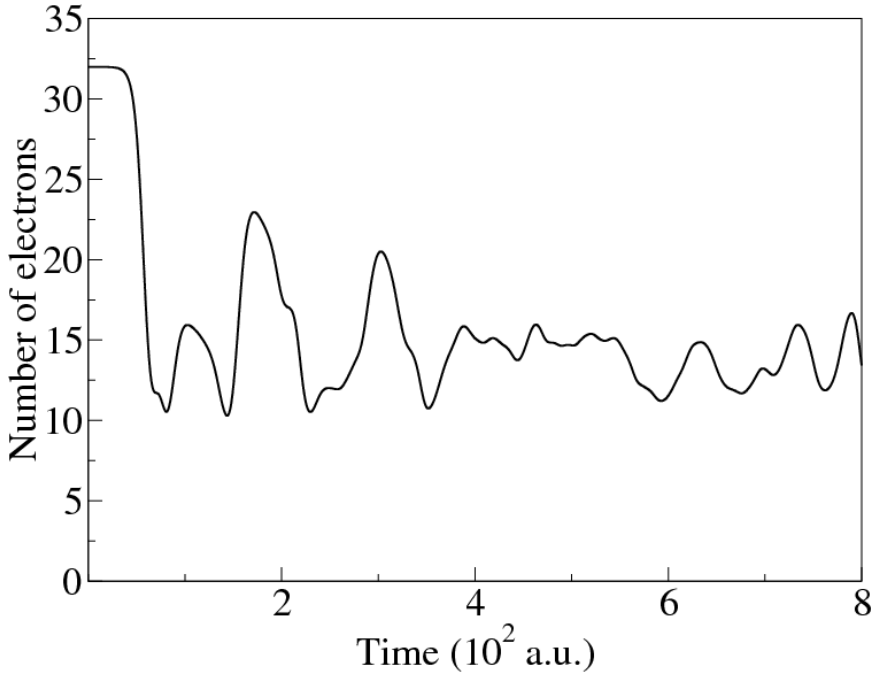

(b)

Figure 4.3: (Color online) (a) Ground state density iso-surface plot and (b) Number of electrons in the ground state orbitals as a function of time.

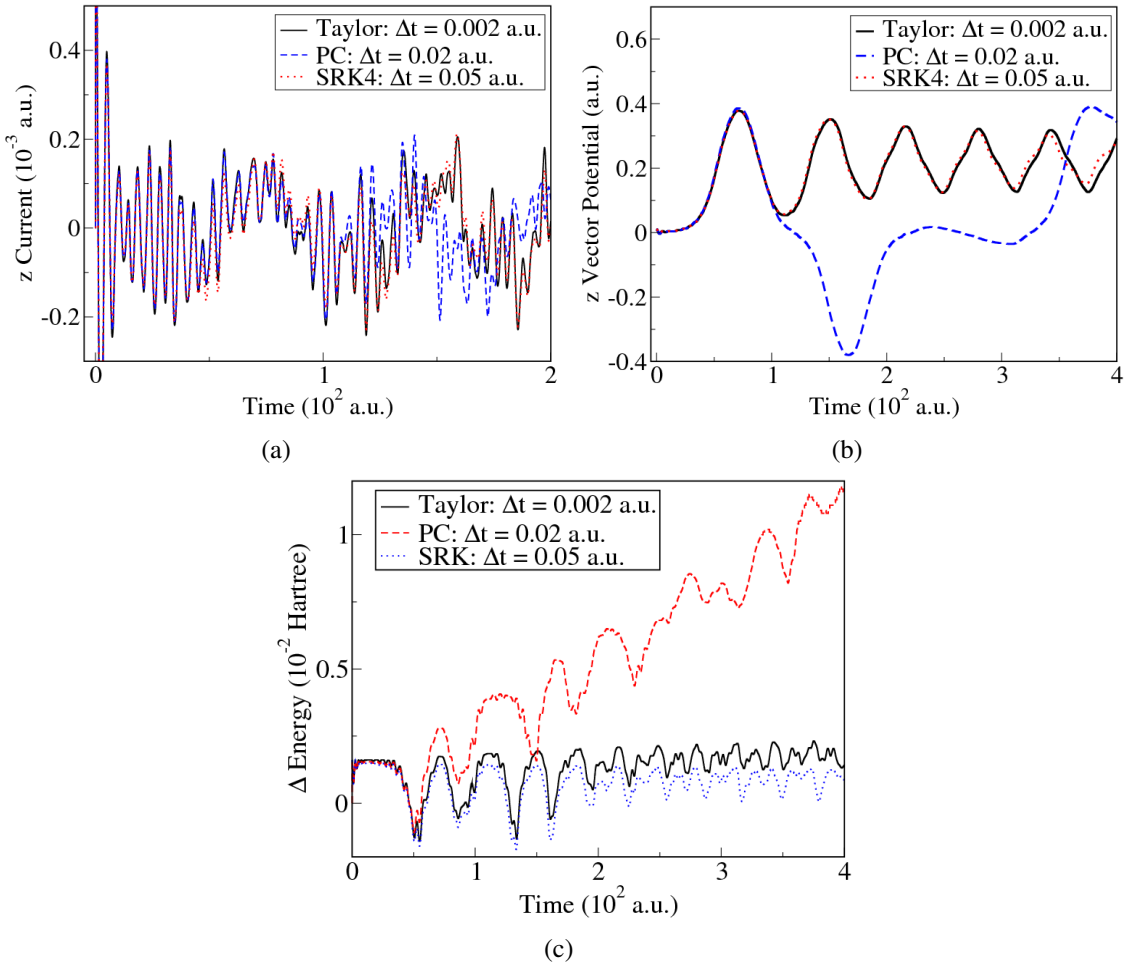

Figure 4.4: (Color online) (a) Current, (b) vector potential and (c) total energy change of a diamond crystal after an applied delta kick on a $2 \times 2 \times 2$ k-point mesh. The system is propagated up to a time of 400 a.u. The current is only plotted up to 200 a.u. The PC and SRK4 propagation schemes are compared. $\Delta t_{PC} = 0.02$ a.u. is used for the PC method, in agreement with the previous sections. The results of the benchmark Taylor and PC methods, also shown in Fig. 4.2, are shown here for comparison. $\Delta t_{SRK4} = 0.05$ a.u. is used since it is the maximum allowed value for this scheme. The SRK4 method finds excellent agreement with the benchmark Taylor propagation with small time step, $\Delta t_T = 0.002$ a.u.

delta-kick perturbation on a $5 \times 5 \times 5$ k-point mesh for a total propagation time of 2000 a.u. The time steps for the Taylor benchmark and the SRK4 method are, as before, 0.002 a.u. and 0.05 a.u. respectively. We consider PC time steps of 0.02 a.u. and 0.05 a.u. On the denser k-point mesh the PC method remains relatively stable with a time step of 0.02 a.u. However, for a time step of 0.05 a.u. the vector potential calculated with the PC method becomes increasingly divergent (see Fig. 4.5.b). The current (Fig. 4.5.a) also diverges from the benchmark Taylor calculation. On the other hand the SRK4 method gives a more stable propagation with larger time steps than the PC method. The current calculated with SRK4 closely agrees with the benchmark, and the vector potential also shows excellent agreement.

In addition, the comparison between the simulations on $2 \times 2 \times 2$ k mesh and $5 \times 5 \times 5$ k mesh using Taylor propagation as benchmark indicates that there is almost no k point sampling dependency for the SRK4 method in applications, i.e. the SRK4 method matches the Taylor results in different k point sampling cases. The PC method shows better accuracy by increasing k point sampling from $2 \times 2 \times 2$ to $5 \times 5 \times 5$ (see Figs. 4.4 (a), (b) and Figs. 4.5 (a), (b)). By using more k points the disagreement (in current and vector potential) in case of PC method is delayed from 100 a.u. to about 1000 a.u.. The reason for this is probable the sensitivity of the PC approach to the smoothness of the density and potential, which requires more fine k point grid. In Ref. [152] a well converged result has been obtained by using $32 \times 32 \times 32$ k point mesh propagating the system up to 500 a.u. with a time step of 0.05 a.u.. A comparison of the PC and SRK4 methods for such a large k point mesh is computationally prohibitively expensive for the time duration needed (2000 a.u). It is, however, quite likely (and our examples show) that the accuracy and allowable time step of the PC approach will increase with finer k point sampling.

To compare the different time propagation approaches further we calculate the dielectric function,

$$\frac{1}{\varepsilon(\omega)} = \frac{1}{A_0} \int_{0^+}^{\infty} dt\, e^{i\omega t - \eta t} \frac{\partial \vec{A}_{ind}(t) \cdot \vec{e}_z}{\partial t} + 1, \tag{4.14}$$

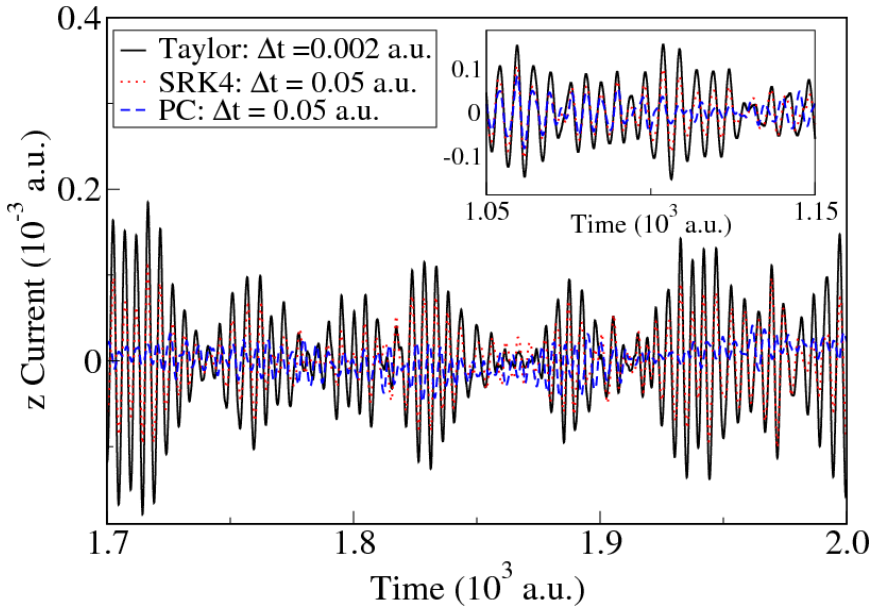

(a)

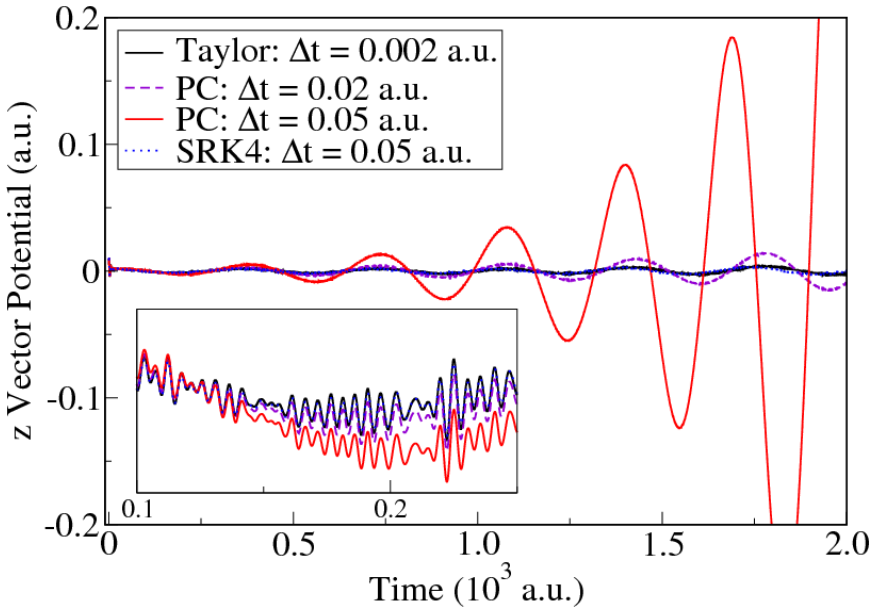

(b)

Figure 4.5: (Color online) (a) Current and (b) vector potential of a diamond crystal after an applied delta kick on a $5 \times 5 \times 5$ k-point mesh. The system is propagated up to a time of 2000 a.u. The current is plotted up from 1700 a.u. to 2000 a.u. Inset (a) shows the current in units of 10^{-3} a.u. from time 1050 a.u. to 1150 a.u. Inset (b) shows the z vector potential in a.u. from time 100 a.u. to 250 a.u. The PC and SRK4 propagation schemes are compared. Time steps of 0.02 a.u. and 0.05 a.u. are shown for the PC method. A time step of 0.05 a.u. is used for the SRK4 method. The SRK4 method finds excellent agreement with the benchmark Taylor propagation with small time step, $\Delta t_T = 0.002$ a.u. for the duration of the propagation.

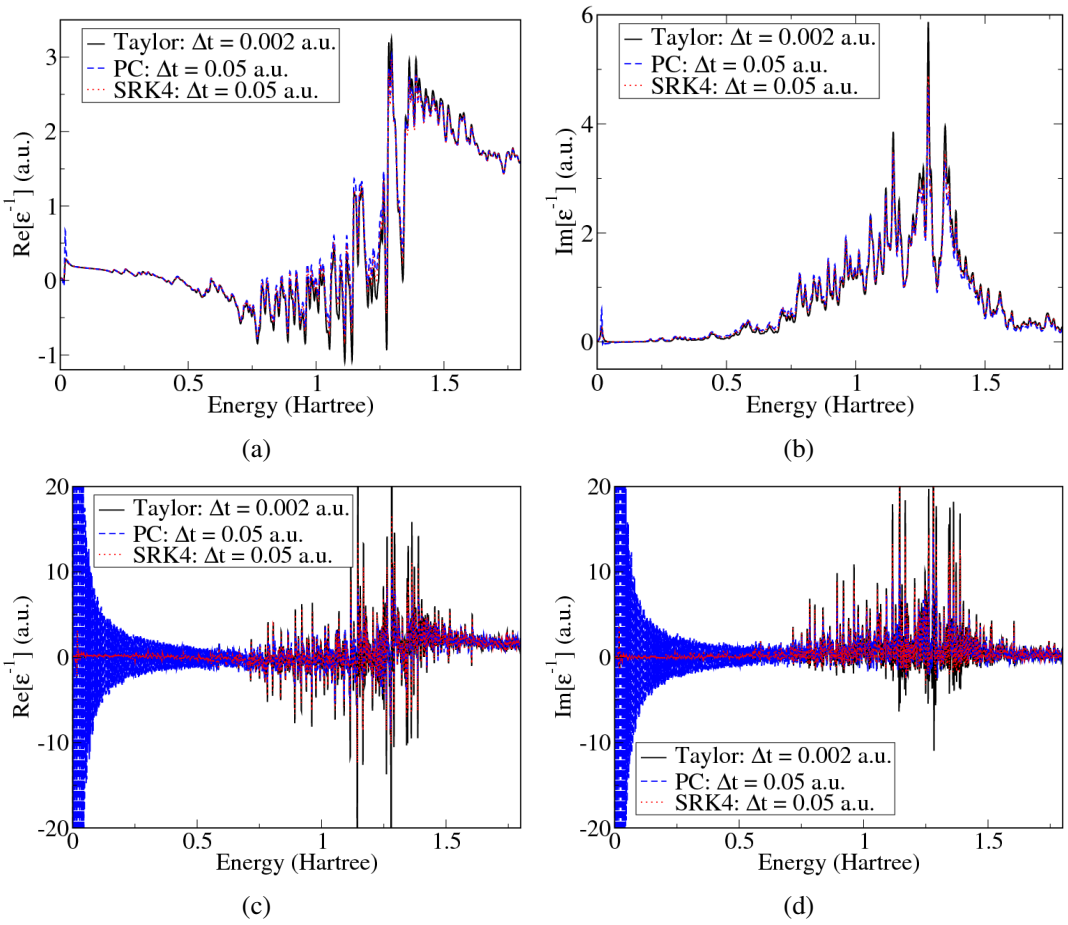

Figure 4.6: (Color online) Inverse of the dielectric constant of a diamond crystal obtained through TDDFT simulations of the electron dynamics after a delta kick on a $5 \times 5 \times 5$ k-point mesh. The Kohn-Sham orbitals are propagated with the Taylor, PC, and SRK4 propagation schemes. Plots (a-b) show the (a) real and (b) imaginary parts of the inverse of the dielectric constant obtained by Fourier transforming the induced vector potential with a small broadening constant, $\eta = 0.005$ a.u. Plots (c-d) show the (c) real and (d) imaginary parts of the inverse of the dielectric constant obtained without a broadening parameter.

where η is a small broadening constant. Fig. 4.6 compares the dielectric functions calculated with the SRK4 and the PC methods, on a $5 \times 5 \times 5$ k-point mesh. The PC propagation with time step, $\Delta t = 0.05$ a.u., produces an unphysical plasmon peak as shown in Fig. 4.6 (a)-(b) in the low frequency range. This spurious plasmon peak has been observed in the literature [152], and has been associated with the use of discrete meshes in real and momentum spaces. The SRK4 and Taylor propagation produces a much smaller spurious plasmon peak, signifying the stability of the propagation.

To understand the qualitative difference observed in the spurious peaks of the two methods, we also calculated the dielectric constant without the broadening parameter, i.e. $\eta = 0$ a.u., as shown in Fig. 4.6 (c)-(d). The dielectric function, when calculated with the PC method and a time step of 0.05 a.u., contains a noisy tail at low energies due to the divergence of the vector potential. The amplitude of the noise is comparable to that of the dielectric function. The introduction of the broadening parameter averages this noise, yielding the small residual plasmon peak in Fig.4.6 (a)-(b). In contrast, the SRK4 method and benchmark Taylor calculation does not produce the unphysical noise at low energies. We note that reducing the time step of the PC method to 0.02 a.u. reduces the noise significantly.

Finally, to show the SRK4 method is a general solver for the Maxwell-TDKS equations, we provide two examples: First, a calculation for the dielectric function for graphene with an applied external field parallel to its plane. The k-point mesh used is $11 \times 19 \times 1$. Cheon et al. [160] calculated the dielectric function using linear response DFT with a fine k-point mesh. The dielectric function computed with SRK4 (see Fig. 4.7) agrees well with their results.

The second example is a simulation for an ultrafast laser pulse applied to the diamond crystal. When the external field is applied, the induced field cancels part of the external field as shown in Fig. 4.8. The calculated current is Fourier transformed to find the high harmonic character of the signals [161]. After the transformation, we find 3 lowest har-

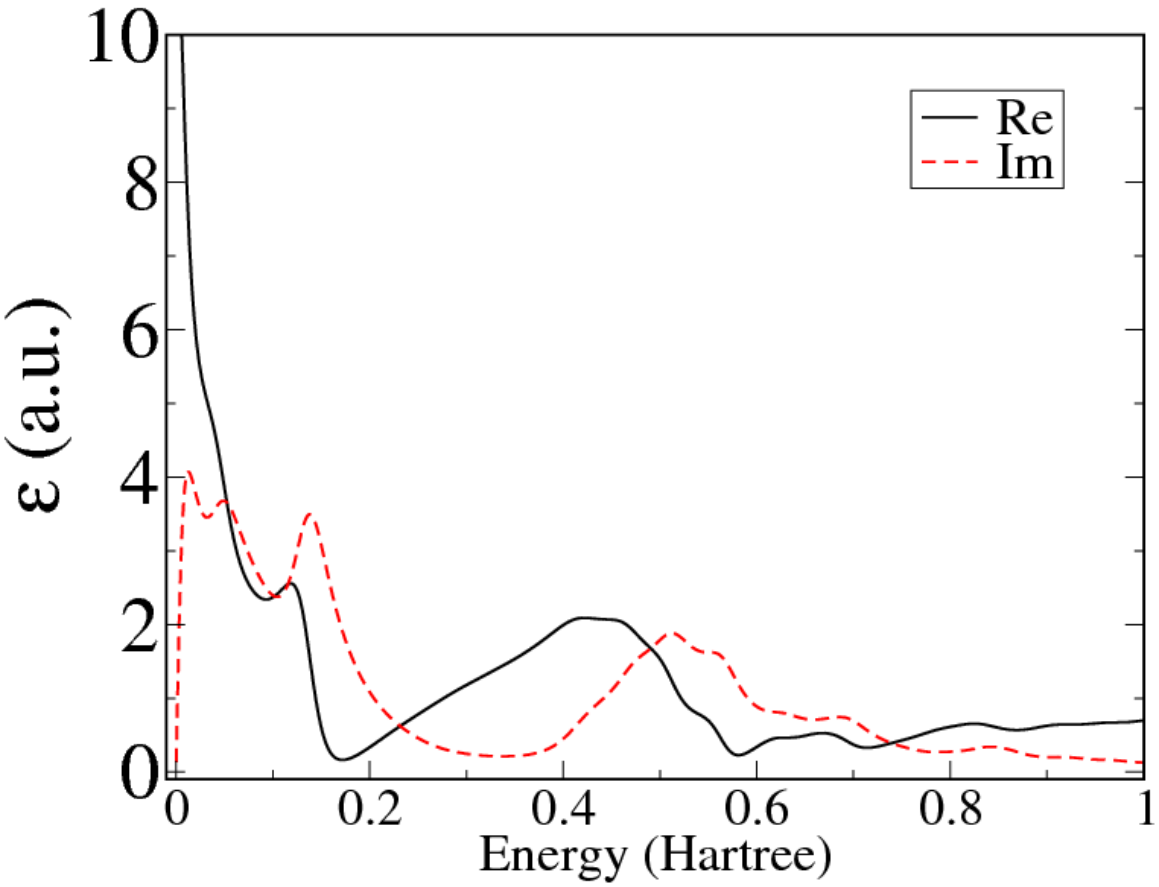

Figure 4.7: (Color online) Real and imaginary components of the dielectric function of graphene obtained with TDDFT simulations of the electron dynamics after a delta kick on a $11 \times 19 \times 1$ k-point mesh. The Kohn-Sham orbitals are propagated with the SRK4 scheme with time step, 0.05 a.u.

Summary of the simulations	Taylor	PC	SRK4
Time step (a.u.)	0.002	0.02*	0.05
Hamiltonian-Orbital Multiplication (operation cost A)	4	8	4
Current evaluation (operation cost B)	1	2	5
Total operation cost (A+0.8B)	4.8	9.6	8
Operations cost per a.u.	2400	480	160

* a time step for relatively stable PC propagation in this paper.

Table 4.1: Comparison of 3 Maxwell-TDKS integrators: Taylor, PC and SRK4 methods.

monics at ω, 3ω and 5ω. The results agrees with the literature [161].

4.6 Summary

We have described an accurate method, the SRK4 approach, for time propagation of the coupled Maxwell and time-dependent Kohn-Sham equation. The new approach uses a simultaneous fourth-order Runge-Kutta based propagation of the vector potential and the Kohn-Sham orbitals. We have compared the approach to conventional fourth-order Taylor propagation and predictor-corrector methods. While the PC method was shown to have a divergence problem dependent on the time step, the SRK4 method can be used for long propagations without divergence. In our test case, the PC method with a time step of 0.02 a.u. gave reasonable results for a propagation time of 2000 a.u. However, even with this small time step increasing numerical inaccuracies in the vector potential were observed. The SRK4 method, in contrast, gave a more stable propagation with a larger time step of 0.05 a.u. . The SRK4 method has shown negligible dependence on k point sampling. Further test on different systems may help to explore the advantages and disadvantages of the present approach comparing to other schemes.

The computational efficiency of the three propagation schemes is summarized in Table 4.1. Compared to the PC method with a time step of 0.02 a.u., the SRK4 method proves more computationally efficient by factor of 3. Since the PC method becomes more numerically unstable with increasing propagation times, one expects that an even shorter time step

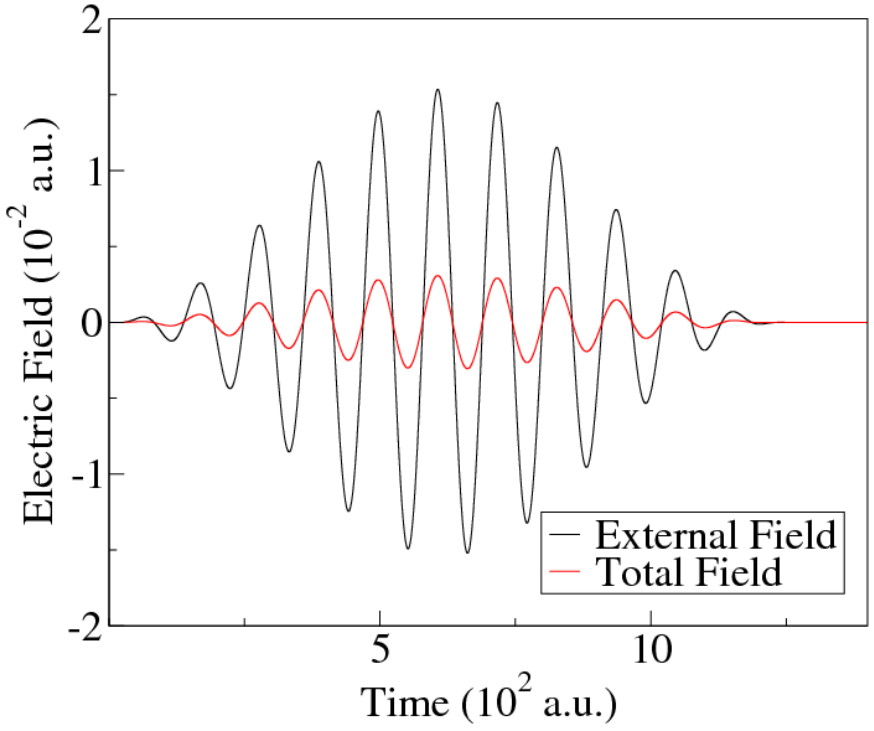

(a)

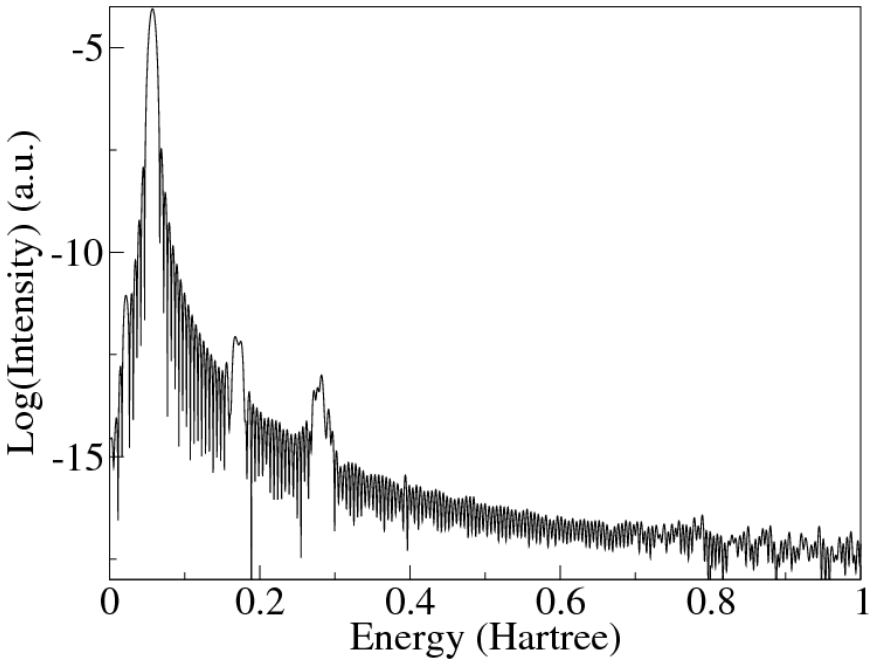

(b)

Figure 4.8: (Color online) (a) Electric field and current in diamond subject to a short laser pulse, calculated by the SRK4 method on a $12 \times 12 \times 12$ k-point mesh. The pulse is 1240 a.u. (30fs) wide with 0.057 a.u. (1.55eV) frequency and 0.0154 a.u. amplitude. (b) The first 3 harmonic generators located at 0.057 a.u., 0.171 a.u. and 0.285 a.u. as shown in the logarithmic scaled current transformed in energy space.

would be required. SRK4 remains very stable even for long propagation times, and therefore the SRK4 method becomes more advantageous as the propagation time is increased.

In energy space, the SRK4 method produced a better signal than the PC method. Fewer numerical artifacts were observed in the calculation of the dielectric function. One must use a broadening parameter for the PC method to remove a spurious plasmon peak at low energies. This artifact was much less prevalent in the SRK4 calculations, further highlighting the numerical stability of this method.

In this chapter, we have tested the Coupled Maxwell and Kohn-Sham propagation for crystalline materials. In the future it would be interesting to explore the possibility of the application for molecules, gases or liquids. Another area of interest is the investigation of the cases with weaker laser and soft bonds [162].

Due to its greater computational efficiency, numerical stability, and more rigorous foundation as a differential equation solver, we recommend the SRK4 method for the solution of the Maxwell-TDKS equations in further studies of coupled Schrödinger-Maxwell.

Chapter 5

Local Currents in Pristine and Single-defect Zigzag Graphene Nanoribbons

In this chapter, the spatial current distribution in H-terminated zigzag graphene nanoribbons (ZGNRs) under electrical bias is investigated using time-dependent density-functional theory solved on a real-space grid. A projected complex absorbing potential is used to minimize the effect of reflection at simulation cell boundary. The calculations show that the current flows mainly along the edge atoms in the hydrogen terminated pristine ZGNRs. When a vacancy is introduced to the ZGNRs, loop currents emerge at the ribbon edge due to electrons hopping between carbon atoms of the same sublattice. The loop currents hinder the flow of the edge current, explaining the poor electric conductance observed in recent experiments. Work shown in this chapter has been published [163].

5.1 Background

Graphene is a two-dimensional material which has attracted considerable interest due to its superior electronic and mechanical properties[164]. Graphene does not have a bandgap, which limits its potential application in nano-electronic devices. Alternatively, Graphene nanoribbons (GNRs) have a bandgap which is opened by the lateral confinement. This makes them promising materials for future nanoscale applications [12, 13, 14, 15, 16, 17, 18, 19, 20]. Currently there are several methods to fabricate graphene nanoribbons such as chemical vapor deposition [15, 16], gas-phase chemical/plasma etching [13], and oxidized unzipping of carbon nanotubes [16, 165, 166, 167]. However, the measured electronic properties of GNRs have an apparent dependency on the experimental process [12, 14, 15]. This may be explained by the difficulty in producing pristine graphene free of defects [12, 16].

An understanding of the local current distribution in electrically biased GNRs, and

how this distribution is affected by defects, is desirable to interpret the measured transport properties. Recently, experimental methods have been developed to image the local current. Stützel et al.[168] investigated local currents in GNRs through scanning photocurrent microscopy, and Lubk et al. [32] measured local currents in solids with atomic resolution using transmission electron microscopy. Negative local resistance has been experimentally observed in GNRs at the low temperature limit, and interpreted using a simple viscous Fermi liquid model of the local current [169].

Although there are many theoretical work on the transmission property of GNRs[170, 171, 172, 173, 174, 175], theoretical investigations of local current are rare and typically use tight-binding models which only consider interactions with nearest neighbors [176, 177]. In these studies only bond currents can be examined while electron hopping between non-bonded atoms is neglected. Solomon et al. [178] included a coupling between second-nearest neighbor atoms in the study of local currents in molecular junctions, and found that current flow through non-bonded atoms dominates in some instances. Since current flow is the result of electron interference between all possible electron transport channels, first principles calculation is needed which includes a more complete electron interactions. In Ref. [179] the local current density in pristine armchair graphene nanoribbons with varying width has been investigated using ab initio calculations, and streamline currents have been observed. The effect of edge hydrogenation and oxidation on the transport of zigzag nanoribbons has been studied in Ref. [180], and spin polarization has been predicted. These examples show the rich physics problems accessible with first principles and/or experimental studies of nanoribbons.

In this work, we investigate the local current under a bias voltage in both pristine and single-vacancy H-terminated zigzag GNRs (ZGNRs) at *ab initio* level using the time-dependent density-functional theory (TDDFT) [61]. The nonequilibrium Green's function approach (NEGF) [25, 7, 26], combined with the density functional theory (DFT) [1] Hamiltonian is the most popular approach to describe steady state electron transport in

nanostructures. This approach, however, is a manifestly ground state theory (it is based on the ground state Kohn-Sham single particle states) and alternative schemes using TDDFT are proposed [181, 182, 183, 184, 185, 186, 187, 188, 189, 190, 191, 192, 193, 194, 195]. The TDDFT is a computationally feasible approach to access excitation energies and it is expected to give a better description of the nonequlibrium current carrying states than the conventional DFT. The apparent advantage of the TDDFT scheme is that it is readily usable for time dependent problems. In an earlier work we have compared the TDDFT and NEGF-DFT approaches for calculation of transport properties of molecular junctions and discussed the differences of the two approaches [69]. One advantage of the TDDFT approach is that it only needs a single time propagation, while in NEGF-DFT one needs converged calculation for many energies to calculate the current. At the same time, NEGF-DFT is evidently time independent, while the TDDFT approach has a transient period before the time-independent limit is reached. Another drawback of the TDDFT approach is that it only works for finite bias, and zero bias conductance cannot be easily calculated with that approach.

The Chapter is organized as follows. In Sec. 5.2 we present the computational details. In Sec. 5.3 we present the calculation of the electron transport for the pristine and single-vacancy ZGNRs, and interpret the results by investigating the local current distribution. Finally, in Sec. 5.3 the paper is closed with a summary and future outlook.

5.2 Computational Details

The current flow in pristine and single-vacancy ZGNRs under a bias voltage are simulated using the bias potential approach we introduced in the section 2.4.1.

Sub-5-nm-wide GNRs [13] are desired for field effect transistors (FET) devices [16] due to their large band gap. Using chemical methods, many sub-5-nm GNR-based devices have been fabricated and studied [12, 13]. We have investigated H-terminated ZGNRs with a width of 1.5 nm, which is similar to that of recent experiments [12, 13], and is also

sufficiently wide for the study of local currents in the presence of a single vacancy. The geometric structures of the pristine and single-vacancy ZGNRs are optimized using the projector-augmented wave method implemented in the Python Atomic Simulation Environment until the atomic forces converge to < 0.02 eV/ Å . The Kohn-Sham equations are solved on a real-space grid with a uniform spacing of 0.25 Å along each spatial coordinate. The simulation cell is a rectangular box with dimensions $L_x \times L_y \times L_z = 60\,\text{Å} \times 25\,\text{Å} \times 10\,\text{Å}$. The ZGNR lies in the x-y plane, with the long side parallel to the x axis. The left and right electrode regions of the bias potential are defined by $x < -20$ Å and $x > 20$ Å, respectively. The origin lies at the center of the simulation box. The projected CAP potential, W, begins at 10 Å from the x boundaries of the simulation cell. The time step is given by, $\delta t = 0.001$ fs. The real-space real-time computer code used in this calculations are developed by our group [196].

5.3 Results and Discussion

In this section we shall investigate the current dynamics induced by a two-step bias potential in pristine and single-vacancy ZGNR graphene nanoribbons. Figure 5.1 shows the geometry of the pristine ZGNR. The three carbon vacancy sites (labeled 1, 2, 3) are also marked on the pristine geometry. Vacancy 1 sits at the edge of the nanoribbon. Vacancies 2 and 3 lie in the middle of the nanoribbon and belong to sublattices A and B, respectively. The step potential ramps to its maximum (minimum) value of 0.05 V (-0.05 V) over 0.5 fs. The shape of the bias potential is shown in Fig. 5.1.

Figure 5.2 shows the time-dependent currents of the four ZGNRs, as induced by the bias potential. The current is obtained by integrating the current density over the plane perpendicular to the center of the graphene nanoribbon, i.e. $I = \int J_x(x = 0, y, z)dydz$. In each case the current strongly oscillates until ≈ 2 fs, after which the current approaches a steady state. The current remains steady until the end of the simulation at time, $t = 8$ fs. The initial oscillations, which are caused by the relatively short ramp time, have been observed

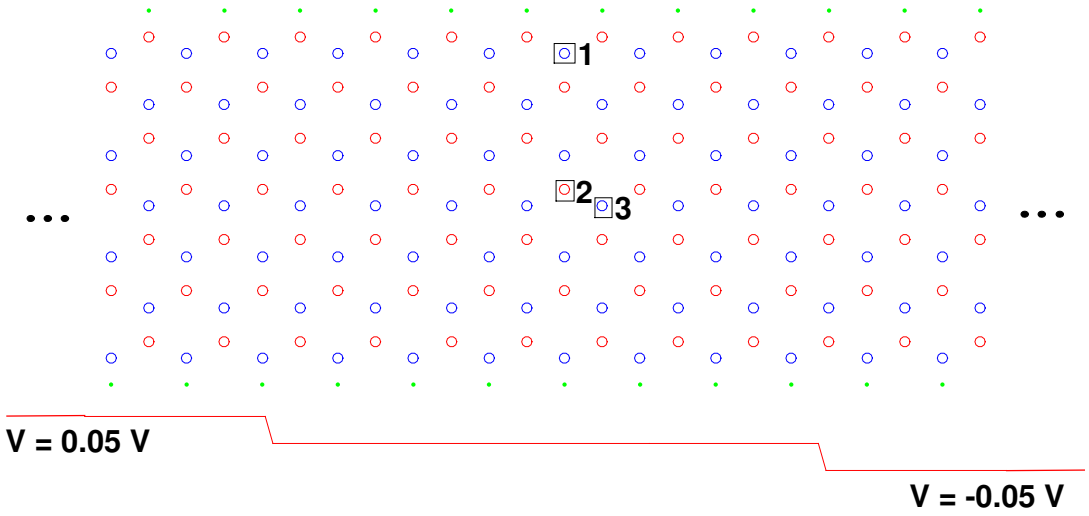

Figure 5.1: (Color online) Geometry of the pristine graphene nanoribbon in the region with zero complex absorbing potential. A (red) and B (blue) are the carbon atoms of the two sublattices. The hydrogen atoms (green) saturate the dangling carbon bonds. The three carbon vacancy sites (boxes 1, 2, and 3) are considered in the calculation, vacancy 1 is an edge vacancy, vacancies 2 and 3 belong to sublattices A and B, respectively. The red line shows the change of the step potential along the x axis (the potential is constant in the perpendicular plane.

in other time-dependent calculations [197, 198, 199, 200]. In each simulation the projected CAP absorbs < 0.066 electrons. At $t = 0$, the pristine and single-vacancy ZGNRs have 1160 and 1156 electrons, respectively. The small number of absorbed electrons justifies the use of the projected CAP for low bias voltage.

The pristine ZGNR current has, in general, the largest magnitude. The introduction of vacancies reduces the current, with a small drop in current for the edge vacancy and a large drop in current for vacancies near the center of the ZGNR. To understand why different vacancy positions result in considerably different conductance, we investigate the local current distribution of the defected ZGNRs.

We shall begin by describing the local currents of the pristine ZGNR at time, $t = 6$ fs, well within the steady-state regime. Figure 6.2.a shows the vector flow of the local current along the plane of the pristine ZGNR. The x and y components of the current flow are

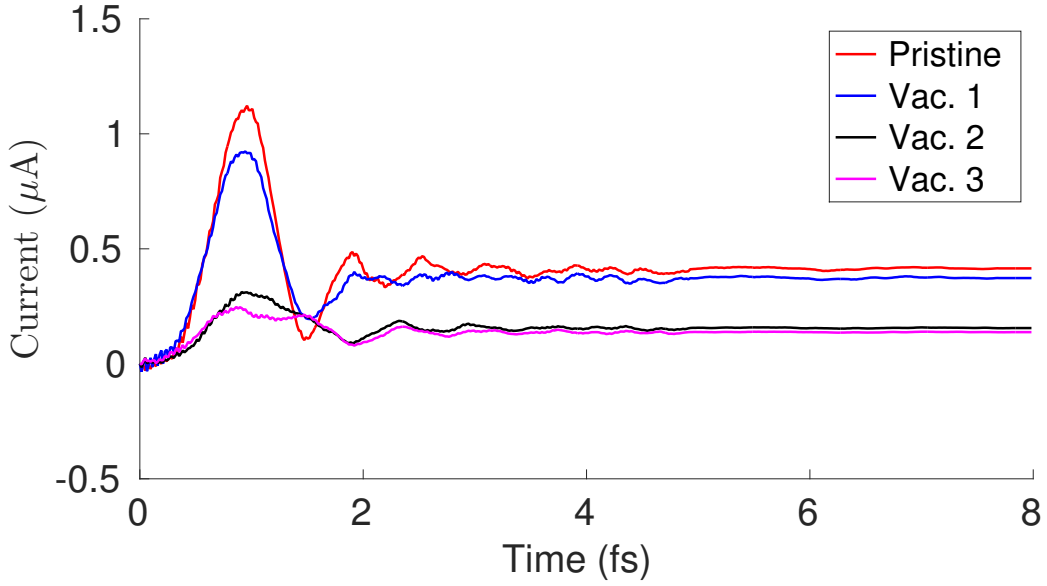

Figure 5.2: (Color online) Time-dependent current of the pristine ZGNR and the three single-vacancy GNRs (see Fig. 5.1).

obtained by integrating over the z direction,

$$J_i = \int J_i(x,y,z)dz \quad i = x,y \tag{5.1}$$

One observes that the current flows along the transport (x) direction and forms streamline patterns. The magnitude of the current density is shown in Fig. 6.2.b. The current flow is greatest along the edge of the ZGNR since this region has a maximal density of states [201]. Fig. 6.2.c shows the magnitude of the current density along the axis perpendicular to the middle of the ribbon (z axis), i.e. $\int J_x(0,y,z)dy$. The peak value is located at ≈ 0.5 Å above and below the ribbon plane, indicating that the current flow is dominated by π-bonded electrons. Due to the nodal symmetry of the π orbitals, the current flow splits into an upper and lower sheet.

We now turn to the description of the local current of the single-vacancy ZGNRs. Fig. 5.4.a shows the local current distribution of a ZGNR with the edge vacancy. The edge current maintains the streamline pattern of a pristine ZGNR, and therefore the conduction

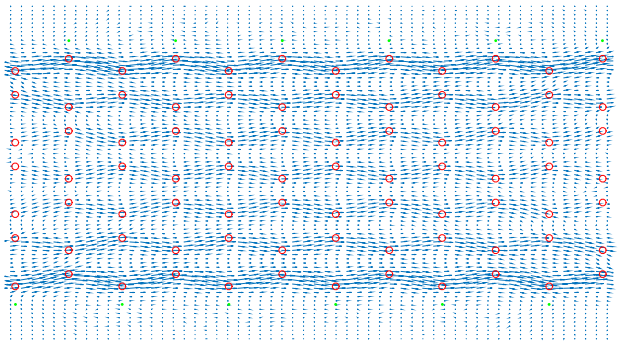

(a)

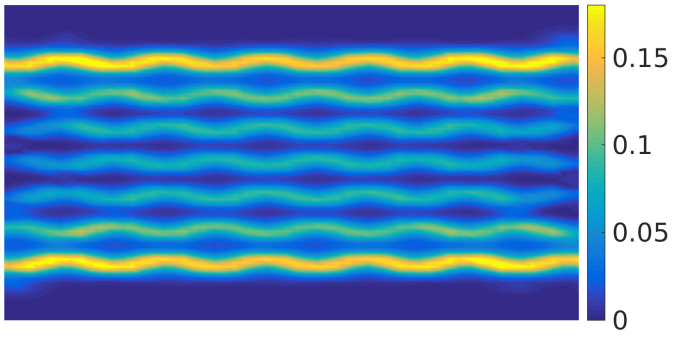

(b)

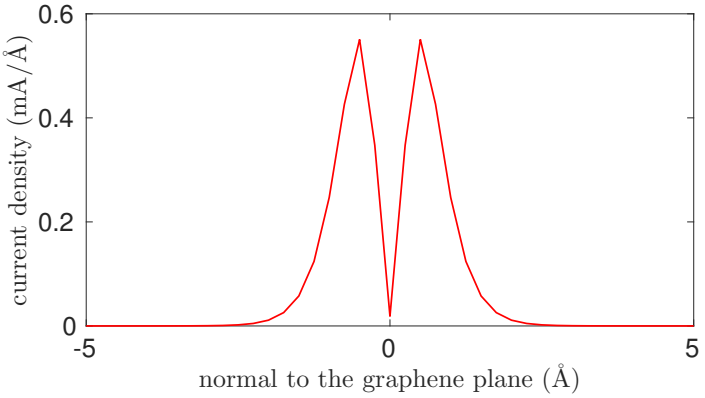

(c)

Figure 5.3: (Color online) Steady-state local current density of a pristine ZGNR. Each plot corresponds to time, $t = 6$ fs. Plot (a) shows a vector map of the local current parallel to the plane of the ZGNR, plot (b) shows the magnitude of the current density (units mA/Å), and plot (c) shows magnitude of current density in the direction perpendicular to the ZGNR plane.

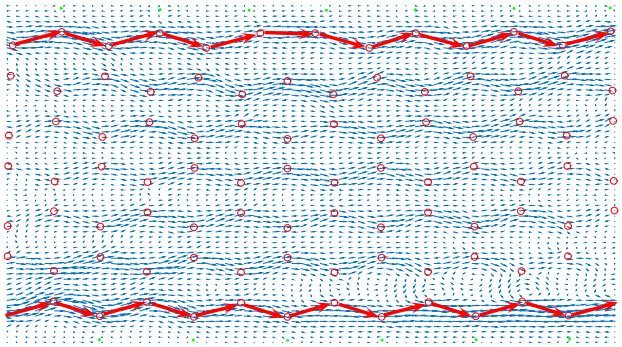

(a)

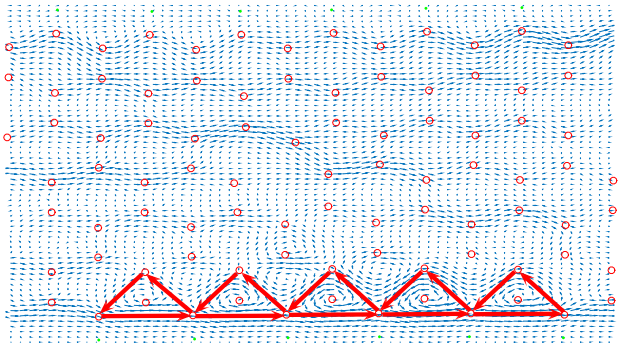

(b)

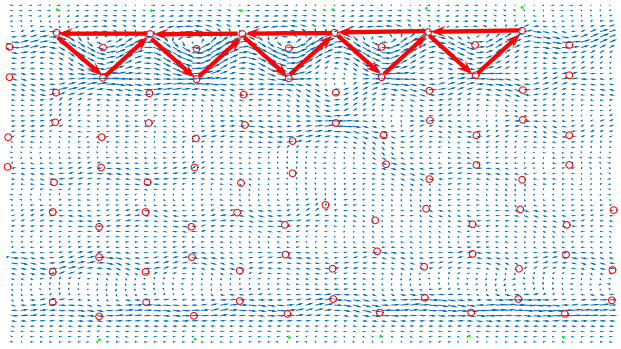

(c)

Figure 5.4: (Color online) Vector maps of the steady-state local current density parallel to the plane of a single-vacancy ZGNR at $t = 6$ fs. Plot (a) shows the local current for vacancy 1, which lines on the edge of the GNR. Plots (b) and (c) show the local current for vacancies 2 and 3, which are located in the middle on of the GNR on sublattices A and B, respectively. The three positions are shown in Fig. 5.1.

remains relatively high. The difference of ground and excited state electron density (not shown) is also the highest at the edges. Fig. 5.4.b and Fig. 5.4.c show that loop currents appear at the edge when a carbon vacancy is introduced in the middle of a ZGNR. The loop currents appear at in sublattice A (B) when a vacancy is introduced in sublattice B (A). The carbon atoms which are adjacent to the vacancy, and are therefore the most affected, belong to the opposite sublattice. The loop currents, induced by the vacancies, break the streamline pattern, leading to the large drop in conductance. The current flow in the ZGNR is the result of the interference of all electron transport paths through the carbon lattice sites. Defects alter the transport path and in some cases induce loop currents. These loop currents can be quite pronounced (see the the bottom of Fig. 5.4.b and the top of Fig. 5.4.c), in other cases they are less visible (see the bottom left corner of Fig. 5.4.a). By moving the position of the vacancy gradually from the edge to the center, the conductance decreases and the loop current at the edge increases.

Summary

In conclusion, we studied the local current distribution of electrically biased ZGNRs using TDDFT. The calculations show that current mainly flows through the edge of pristine ZGNRs under small bias. Loop currents, due to electron hopping through carbon atoms belonging to the same sublattice, emerge at the ribbon edge when there is a carbon vacancy in the middle of ZGNRs. These loop currents hinder the flow of edge current, resulting in the poor electrical conductivity. Recent experiments have observed loop currents caused by electron backflow in graphene [169]. In our case, the loop currents are the result of electron hopping between carbon atoms belonging to the same symmetry sublattice. Neto *et al.* proposed that electrons in graphene could hop between carbon atoms belonging to the same sublattice, and that this hopping is very weak [202]. Our results show that inter-lattice hopping can be very strong under electrical bias when a carbon vacancy is introduced. These simulations will drive future experiments and simulations studying the

effect of defects on the conductance of graphene nanoribbons. The projected CAP method has proven effective at low bias voltage. Simulations involving high bias voltages would be more complex since a method of electron injection would become necessary. Topics for future investigations include the local currents of multiple carbon vacancies, doped GNRs, and GNRs with surface adsorbates, which are common methods to modify the transport properties of GNRs[203, 204]. The electron dynamics determine the performance of GNR-based devices, and therefore studying local currents is important for developing practical applications of GNR-based device.

Chapter 6

Simulation of Local Currents in Low Dimension Materials Using Complex Injecting Potentials

In this Chapter, We use a complex injecting potential method discussed in section 2.4.2 to inject electrons into the conduction band, mimicking electron currents in nanoscale systems. The injected electrons are time propagated until a steady state is reached. The local current density can then be calculated to show the path of the conducting electrons on an atomistic level. The method allows for the calculation of the current density vectors within the medium as a function of energy of the conducting electron. Using this method, we investigate the electron pathway in graphene nanoribbons in various structures, in molecular junctions, and in black phosphorus nanoribbons. By analyzing the current flow through the structures, we find strong dependence on the structural geometry and the energy of the injected electrons. This method may be of general use in the study of nano-electronic materials and interfaces. Work shown in this chapter has been submitted to the physical review B.

6.1 Background

With the need for faster computer processors comes the need for ever smaller transistors. Recently, due to the scaling issues of silicon transistors [205, 206], much focus has been placed on the use of graphene nanoribbons (GNRs) [207, 208], carbon nanotubes [209, 210, 211], nanowires [212, 213, 214], transition metal dichalcogenides [215, 216, 217], and other low dimensional materials [218, 219, 220, 221, 222, 205, 223, 224, 225, 226, 227, 228]. An advantage of using carbon–based materials for nanoscale electronics is that a variety of fabrication techniques exist [21, 22, 23, 24]. However, unwanted quantum and short channel effects, e.g. leakage current, occur in transistors with channel lengths

on the nanometer length scale [229, 230, 231]. Therefore, in nano-electronic devices, an understanding of electron transport properties is fundamental for practical applications.

Most experimental and theoretical work focuses on global observables, such as the current-voltage (I-V) curve and the transmission spectrum. The underlying physics, for example the local electron pathway[232], is usually neglected. As devices get ever smaller, approaching the nano scale, the study of spacial dependency of current density is important as it unveils the electron pathway through the structure and can help us better understand the transport properties, e.g. the role of the bonds, defects and impurities.

Experimental observation of the microscopic current flow has been the focus of several recent studies [33, 34, 35]. However, these investigations only determine the current over several nanometers or larger and cannot be considered atomic resolution. One study [32] was able to show the electron current in $SrTiO_3$ using the lateral probability current of the scattered electrons from transmission electron microscope images, though this technique could not be applied to a low dimensionality system. Due to the limited access to the current density on an atomistic scale by experimental means, quantum computational simulations are needed.

Several methods exist for computationally studying the conductance properties of materials. The nonequilibrium Green's function approach (NEGF) [25, 7, 26, 27, 28, 29], combined with the density functional theory (DFT) [1] Hamiltonian is the most widely used method for studying electron transport in nanostructures [233, 2, 3, 4, 5, 6, 7, 8, 9, 10, 11]. This approach, however, is a ground state theory (it is based on the ground state Kohn-Sham single particle states) and alternative schemes using time dependent density functional theory (TDDFT) are proposed [181, 182, 183, 184, 185, 186, 187, 188, 189, 190, 191, 192, 193, 194, 195].

The use of TDDFT for transport calculations is not easy. One possible approach is to use a large but finite system with a bias potential to move electrons across the system [183, 234, 235]. The disadvantage of that approach is that large system reservoirs are nec-

essary for long time propagation, especially to reach steady states. The bias moves the electrons, but the electron deficiency in the lead regions eventually makes the simulations unphysical. Moreover, a complex absorbing potential (CAP) has to be introduced [235] to avoid artificial reflections from the boundary making the calculations computationally expensive. The CAP should only absorb the current carrying orbitals, so one has to project out the ground state components, and the computational cost of applying the projected-CAP is proportional to the square of the total number of orbitals, adding significant computational effort as the system size increases.

A better approach is to use a source potential to supply the system with electrons. The construction of such a potential is not simple because it has to be a steady source of electrons. In a recent work [236] absorbing and anti-absorbing boundaries are introduced for simulating the coupling to a source and a drain and to supply the system with electrons without electrical polarization build-up. This approach can alleviate the issues with reflections and loss of electrons, but the construction of the anti-absorbing boundary is nontrivial and it eventually leads to changes in the orbitals, making long time simulations difficult.

In this chapter we will show how a complex injecting potential can be used in transport calculations. In a recent work [237] we have developed a time–dependent source potential approach in which one can inject a desired state into a quantum system. We have tested the approach on simple analytically solvable model systems to check its accuracy. In the present paper we apply the injecting potential approach on nanoscale systems with atomistic details within the framework of TDDFT. In this approach a complex potential, acting as an electron source, is added to the Hamiltonian. The system is time propagated with continuous injection of electrons until a steady state is reached. The spatial current density is then calculated from the steady state wavefunction. This method greatly reduces computational cost since one only needs to propagate one orbital – the injected electron. In addition, the injection method allows for the study of the local current corresponding to a specific energy level. The main advantage of the method is that the transport problem is

solved in a finite simulation box without loosing electrons and without introducing artificial charge buildup.

6.2 Computational Details

The initial state of the system is prepared by solving for the ground state wavefunction using DFT. To model electron injection into the system, we use a point source potential method proposed in section 2.4.2 The time-dependent KS equations were solved on a real-space grid with a uniform spacing along each spatial coordinate. A plot of the current density injected into a GNR is shown in Fig. 6.1. The simulation cell is a rectangular box with dimensions dependent upon the system under investigation. At least 4 Å of vacuum is placed between the atoms and the boundary to prevent confinement of the ground state wavefunction. The material lies in the *x*-*y* plane, with the long side parallel to the *x* axis. The CAP begins $5-10$ Å inside the system in the *x* direction and reaches a maximum on the outermost atoms. This configuration insures that the injected wavefunction will be completely absorbed before reaching the end of the system and effectively renders the system infinite (not quantized) in the transport direction. With systems typically several nanometers in the transport direction and a few nanometers wide, the bases are on the order of a million grid points. A time step between $\delta t = 0.0008$ fs and $\delta t = 0.0015$ fs was used. The real–space real–time computer code used in these calculations was developed by our group [238].

In this implementation of the injecting potential method, the injected electronic wave function is not renormalized after steady state is reached. Because we are interested in the local electron pathway through the system, the normalization is not important and the calculated current density is scaled by an arbitrary constant. In principle one could normalize the continuum states by box normalization see e.g. [239] and then the transmission probability can be calculated by integrating the current. In this work we chose a different venue and we calculated the transmission coefficient with the Monte-Carlo method as proposed

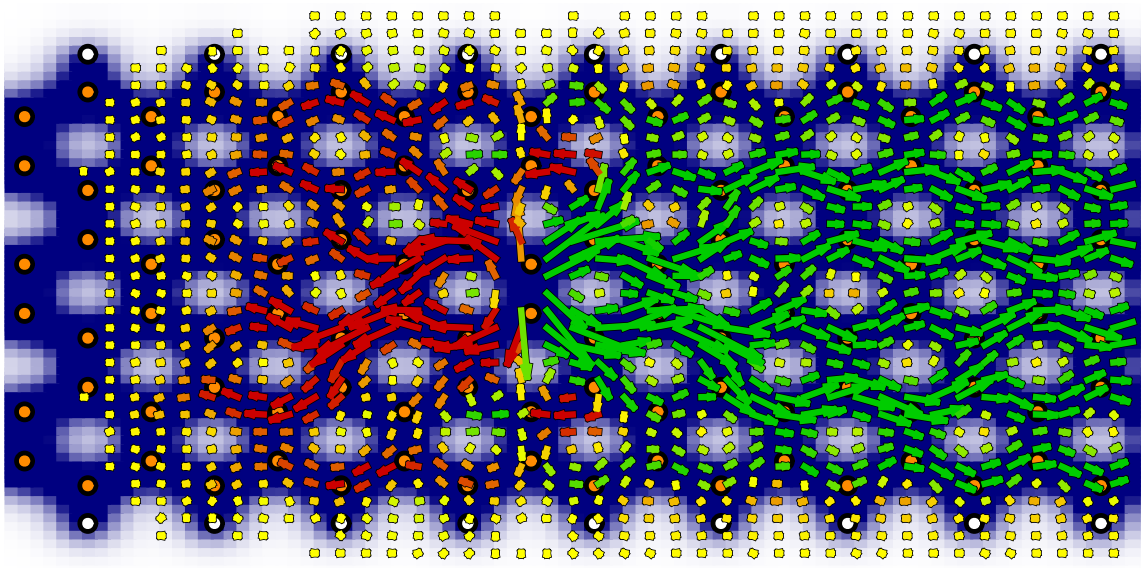

Figure 6.1: An image of the x–y current density resulting from a point source injection in a GNR. The injected wave is being absorbed on the left and spreading out on the right.

in Ref. [240].

6.3 Results and Discussion

In this section we shall investigate the local current distribution of different materials that are potential building blocks in the nano-scale devices.

6.3.1 Graphene Nanoribbons

6.3.2 Graphene Nanoribbons

The first example illustrates graphene nanoribbons with possible defect structures. Fig. 6.2.a shows the local currents along the plane of the pristine zigzag graphene nanoribbon (ZGNR) at an injection energy of 0.5 eV above the Fermi level. Also shown in the figure, as the background, is the electron density distribution of the nanoribbon to show the bonds. The injection point is located in the center of the nanoribbon with respect to the perpendicular directions and at 20 Å from the left boundary of the simulation cell in the transport

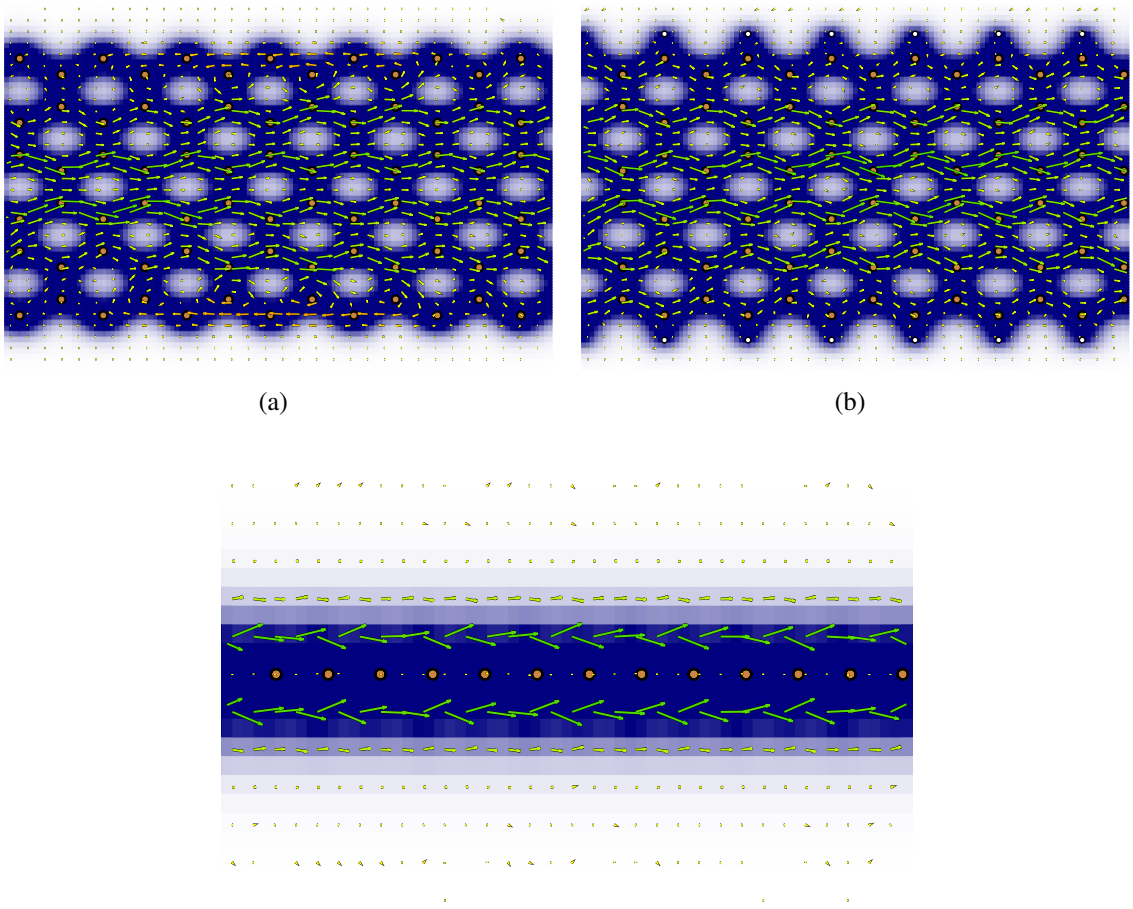

(a) (b)

(c)

Figure 6.2: Local current density vectors from injected state at 0.5 eV above Fermi level of ZGNRs overlaid on the charge density background. The current density vectors are color-coded to show the different flow directions. Plot (a) shows vector map of local current density in a pristine ZGNR at injection energy of 0.5 eV above Fermi level. loop current is formed at edge causing electron back flow. Streamline pattern is observed in the middle. Plot (b) shows vector map of local current density in a pristine ZGNR saturated with hydrogen atoms (white) at same injection energy. Streamline pattern is established at the edge. Plot (c) shows the side view of local current density distribution

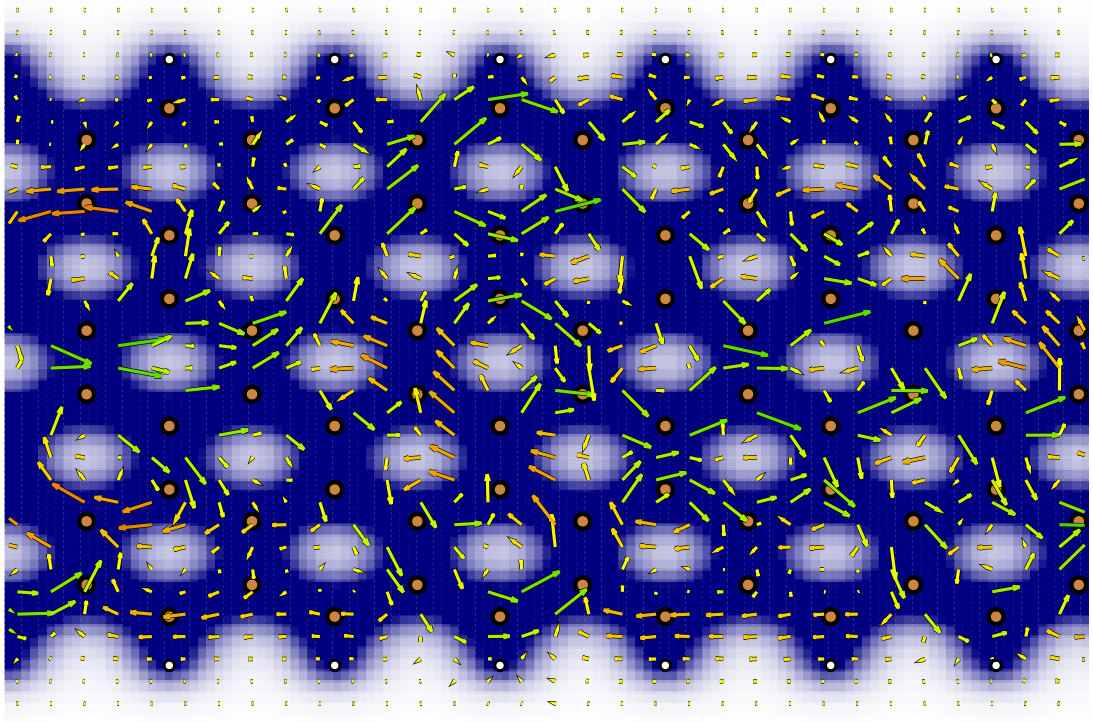

Figure 6.3: local current density vector from injected state at 2 eV above Fermi level of ZGNRs overlaid on the charge density background. The current density vectors are color-coded to show the different flow directions.

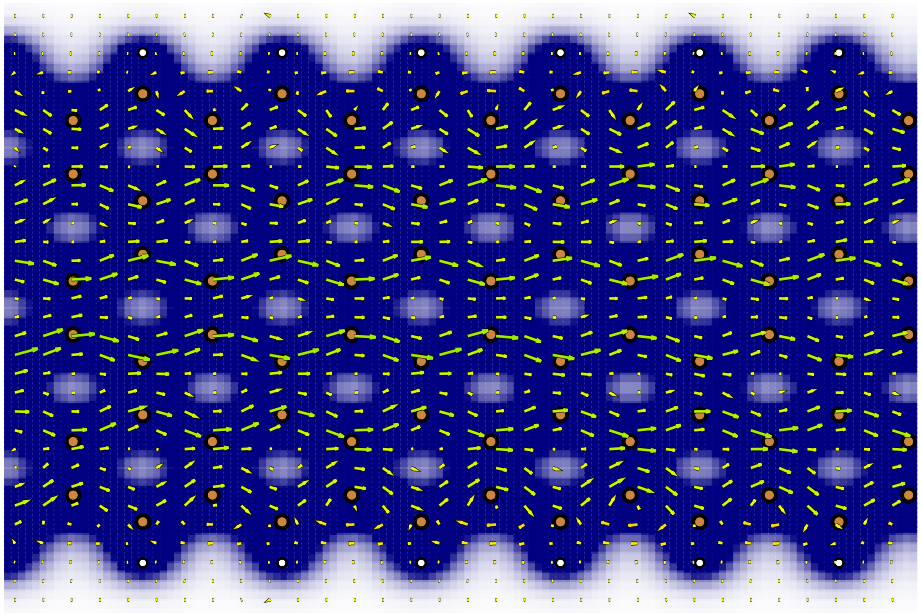

(a)

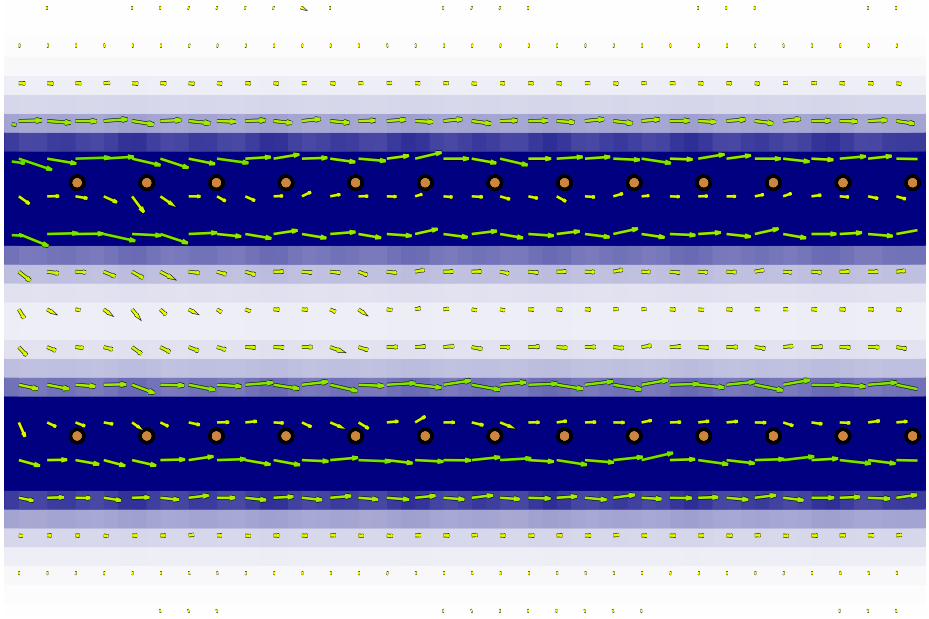

(b)

Figure 6.4: Local current density vectors from injected state at 0.5 eV above Fermi level of a bilayer AA stacking ZGNRs overlaid on the charge density background. The current density vectors are color-coded to show the different flow directions. Plot (a) shows the top view Streamline pattern is observed. Plot (b) shows the side view. Current splits into both layers and flows along the corresponding π bonds of each layer.

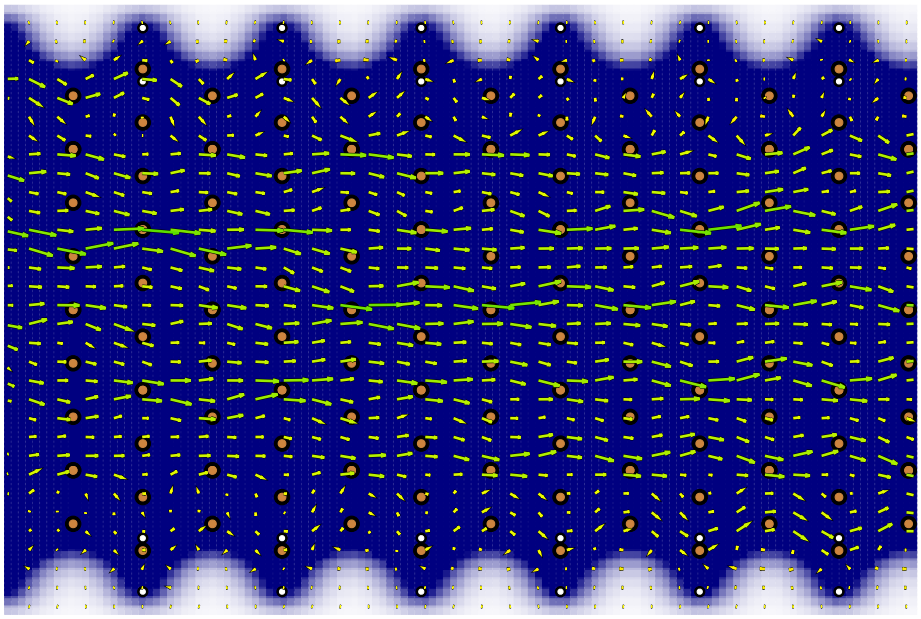

(a)

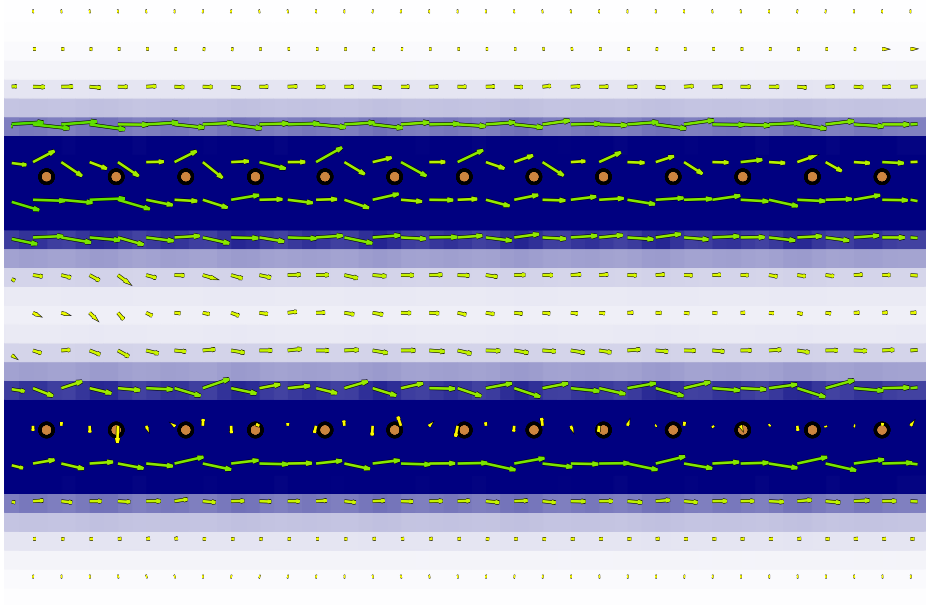

(b)

Figure 6.5: Local current density vectors from injected state at 0.5 eV above Fermi level of a bilayer AB stacking ZGNRs overlaid on the charge density background. The current density vectors are color-coded to show the different flow directions. Plot (a) shows the top view Similar streamline pattern is observed. Plot (b) shows the side view. Current splits into both layers and flows along the corresponding π bonds of each layer.

direction. The CAP starts at 10 Å from the ends of the nanoribbon in the x direction. The current shown is at $t = 80$ fs, long after the wavefunction has developed into a steady state.

The x and y components of the current flow are obtained by integrating over the z direction,

$$J_i = \int J_i(x,y,z)dz \quad i = x,y \tag{6.1}$$

The current flow is color-coded to help visualize different directions. One observes that the current flow forms streamline patterns along the bonded carbon atoms in the middle of the ribbon and loop currents at the edge. These loop currents are due to the dangling bonds of the unsaturated carbon atoms at the ribbon edge and cause electron back flow. The charge density distribution at the edge of pure ZGNR is relatively delocalized and provides a channel for electron backflow. Depending upon method of production [241, 242], hydrogen atoms typically saturate those dangling bonds. As shown in Fig. 6.2.b, by saturating the dangling bonds with hydrogen atoms, the loop currents and hence the electron back flow are greatly reduced while streamline pattern is established at the edge. The charge density at the edge of pure ZGNR is more localized compared to that pure ZGNR and thus blocks the channel for electron backflow. Therefore, hydrogen terminated ZGNR has a more consistent local current pattern and better transport property. Also the calculated transmission coefficient of the hydrogen terminated ZGNR is 1.0182 and the pure ZGNR is 0.9581, which means that pure ZGNR is slightly less conductive than hydrogen terminated ZGNR

The side view (see Fig. 6.2.c) shows that the current mainly flows above and below the plane of atoms and no current is observed in the plane. This indicates that the current mainly flows through the π bonds, due to the nodal symmetry of which the current flow splits into an upper and lower sheet. In addition, because of the shape of π bonds, the current does not flow evenly and tends to go up and down along the π bonds. Currents at other energy levels are also studied, we observe similar pattern for energy levels from 0-1.5 eV above the fermi level. This might be due to the fact that there is only a single transmission

channel due to the π band in this energy window [243] For higher energy levels because of the interference effect of multiple transmission channels, the current shows different pattern. As an example, Fig.6.3 shows the currents at an injection energy of $2eV$ above the fermi level.

Bilayer GNR has been proposed to be a building block in the field-effective transistor due to their widely tunable bandgap in the presence of a external electric field [244, 245]. In transport experiments, bilayer GNR are usually put on top of gold electrodes with which only one layer is directly connected to. It would be interested to know, after electron jump from the electrodes into one layer of the GNR, whether it will remain in that layer alone or spread into both layers. This can be perfectly studied using the injection method. We will inject electrons on top of one layer. We will investigate the most two common stacking: AA and AB stacking. Current has similar streamline pattern as shown in Fig. 6.4.a and Fig. 6.5.a. The side view Fig. 6.4.b and Fig. 6.4.b, show that the injected electrons spread into both layers and flows along the corresponding π bonds of each layer in both cases.

By doping graphene nanoribbons, one can modify its electronic properties, with common doping elements being boron and nitrogen[246, 247]. Fig. 6.6.a shows the local currents of boron-doped, nitrogen-doped, and boron-nitrogen co-doped ZGNRs. A strong loop current is formed near the boron doped site, as shown in Fig. 6.6.a. There are also two weak but larger loop currents joining the dominant one. Since boron has only a nuclear charge of 5, inclusion in the lattice creates a region of slightly higher potential (considering the full KS potential) which acts as a barrier to the conducting electron. In the nitrogen-doped case, as shown in Fig. 6.6.b, part of the current is scattered before reaching the doped site. Nitrogen has a nuclear charge of 7 which, considering the full KS potential, creates a region of slightly lower potential. This nitrogen defect is then acting as a trap for the electron. The calculated transmission coefficient for the boron-doped and nitrogen-doped ZGNR at this energy level are 0.5513 and 0.6827 respectively, which is a big drop compared to the pristine ZGNR case. Fig. 6.6.c shows the local currents in the boron and nitrogen co-doped

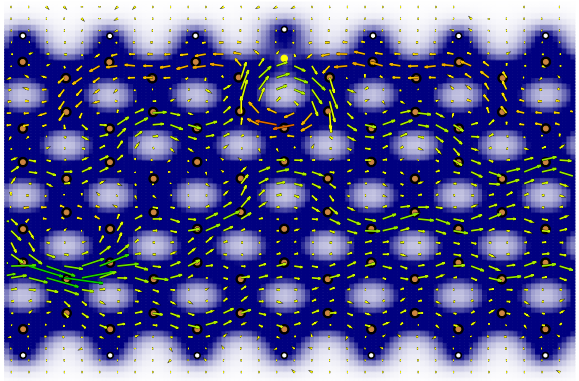

(a)

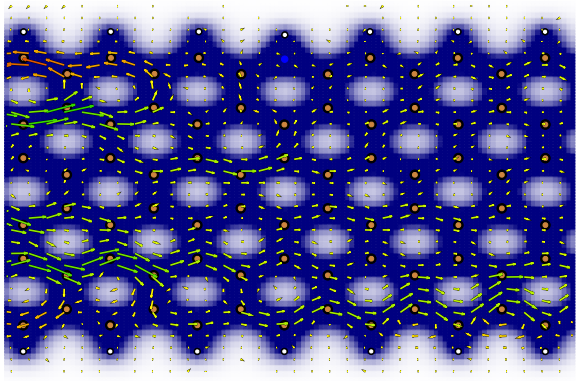

(b)

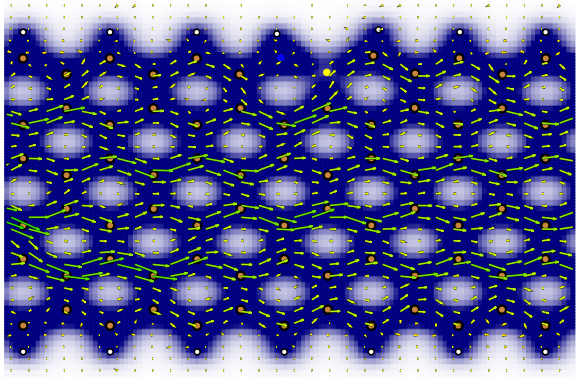

(c)

Figure 6.6: Local current density vectors from injected state at 0.5 eV above Fermi level of doped ZGNRs overlaid on the charge density background. The current density vectors are color-coded to show the different flow directions. Plot (a) shows the local currents of boron atom(yellow) doped ZGNR. A strong loop current is observed at doped site with two weak loop currents at the side. Plot (b) shows the local currents of nitrogen atom (blue) doped ZGNR. Part of the current turns around before reaching the doped site. Plot (c) shows the local currents of a boron and nitrogen co-doped case. Streamline pattern similar to that in 6.2.b is established

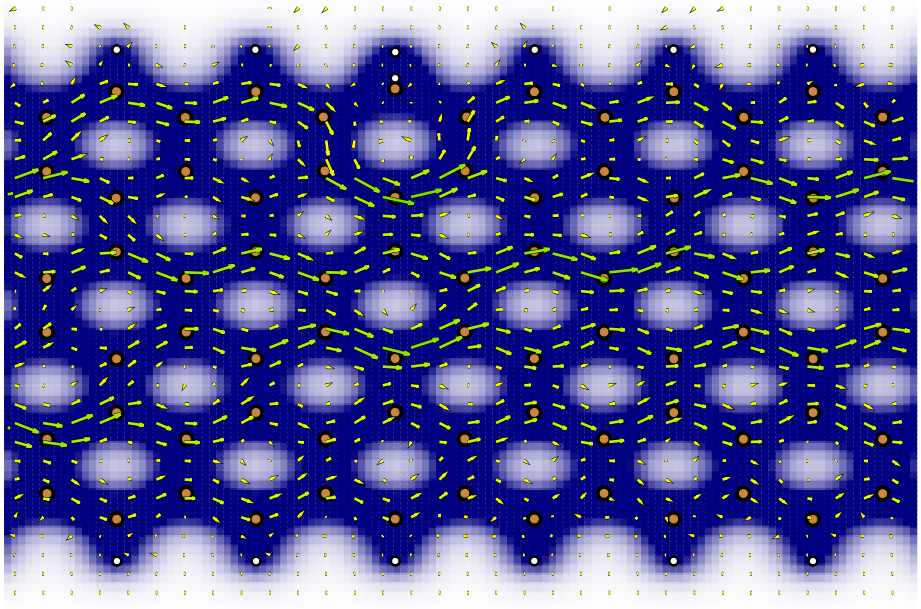

(a)

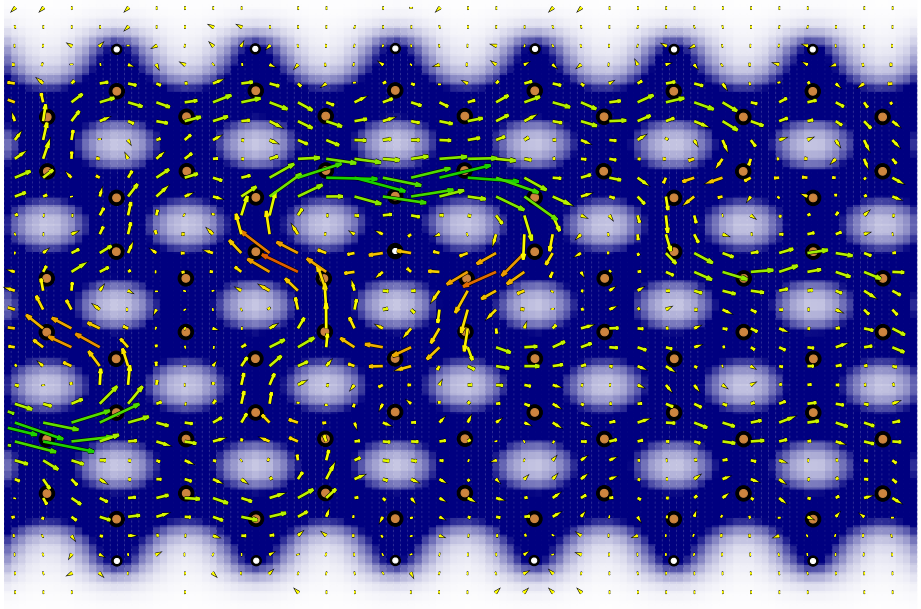

(b)

Figure 6.7: Local current density vectors from injected state at 0.5 eV above Fermi level of hydrogen atom adsorbed ZGNRs overlaid on the charge density background. The current density vectors are color-coded to show the different flow directions. Plot (a) shows the local currents of ZGNR with hydrogen atom adsorbed on the edge. Current bypass the adsorbed hydrogen atom and streamline pattern is preserve in the middle. Plot (b) shows the local currents of ZGNR with hydrogen atom adsorbed on the middle. A loop current is formed around the adsorbed hydrogen atom

case. The streamline current pattern is restored. This can be explained by the recovery of the sp^2 network due to the valence compensation effect of boron and nitrogen atom (boron has three valence electrons and nitrogen has five). Also, this recovery is demonstrated in the calculated transmission coeficient of 0.9913 which is close to that of the pristine case. At other low energy levels below 1.5 eV, the current pattern is sightly different for the boron or nitrogen doped case. However the general trend is similar. The streamline pattern observed in the pristine ZGNR is restored in the nitrogen and boron co-doped case.

Molecule adsorption is another way to change the electronic property[248, 249]. Fig. 6.7 shows the local currents of hydrogen atom adsorbed ZGNRS. We find that the current pattern is strongly dependent on the location of the adsorbed hydrogen atom. When the hydrogen atom is adsorbed on the edge of ZGNR, as shown in Fig. 6.7.a, the current bypass the adsorbed hydrogen atom and streamline pattern is preserved in the rest of ZGNR. When the hydrogen atom is adsorbed in the middle of ZGNR, as shown in Fig. 6.7.b, a strong loop current is formed around the adsorbed hydrogen atom, which destroys the streamline pattern and hinder the current flow. Therefore, the hydrogen atom will have a greater impact on the electron transport when it is adsorbed in the middle of ZGNR. The calculated transmission coefficient of ZGNR with hydrogen atom adsorbed on the edge and the middle are 0.7897 and 0.1139 respectively, which also demonstrate the site dependency of conductance with far greater drop for the latter case.

6.3.3 Graphene Nanoribbon Constrictions, Wing and Bent Structures

Constricted GNRs [250] are the next set of examples. In this case, we inject electrons at different energy levels in a wedge-shaped constriction. Fig. 6.8.a shows the local currents at 0.1 eV above Fermi energy. We observe no current except small loop currents at edge. Fig. 6.8.a shows the local currents at 0.5 eV Fermi energy above Fermi energy. Current flows in in the middle and gradually turns back along the edge and so the total current is near zero. Therefore, almost no current gets transmitted through the constriction at these

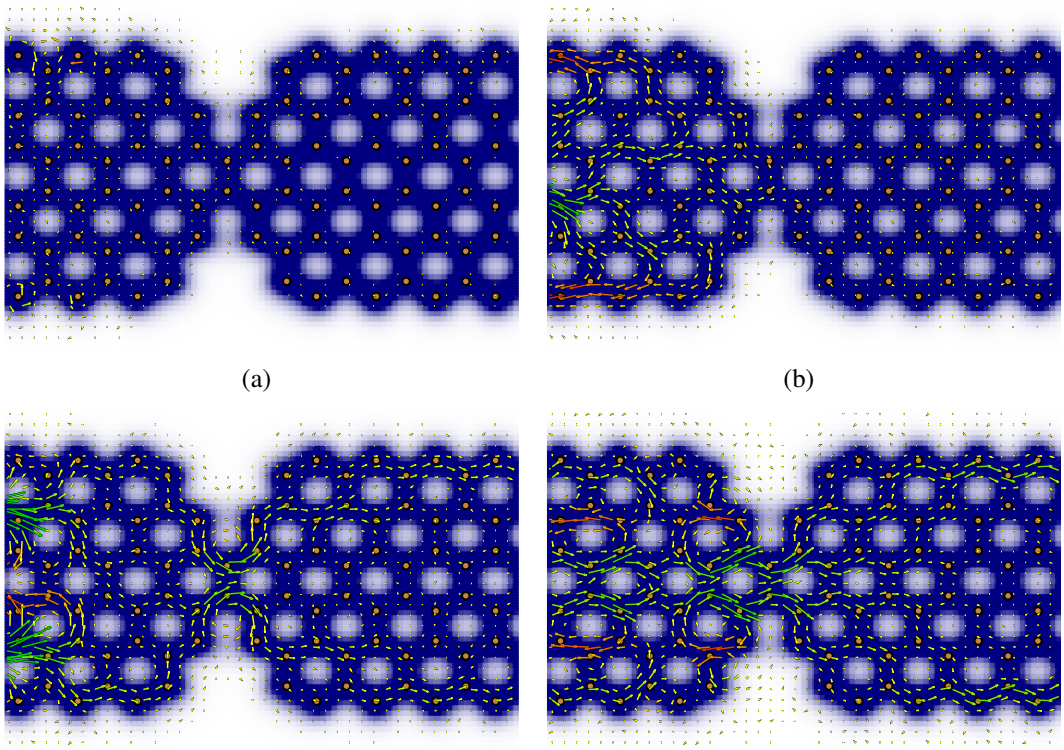

Figure 6.8: Local current density distributions of a constricted ZGNR at different injection energy levels. Plot (a) injection at the Fermi level. Almost no current is observed Plot (b) is at 0.5 eV above the Fermi level. Current turns around and does not get transmitted through the constriction. Plot (c) and (d) are at 1 eV and 2 eV above the Fermi level respectively, where part of current gets transmitted through the constriction.

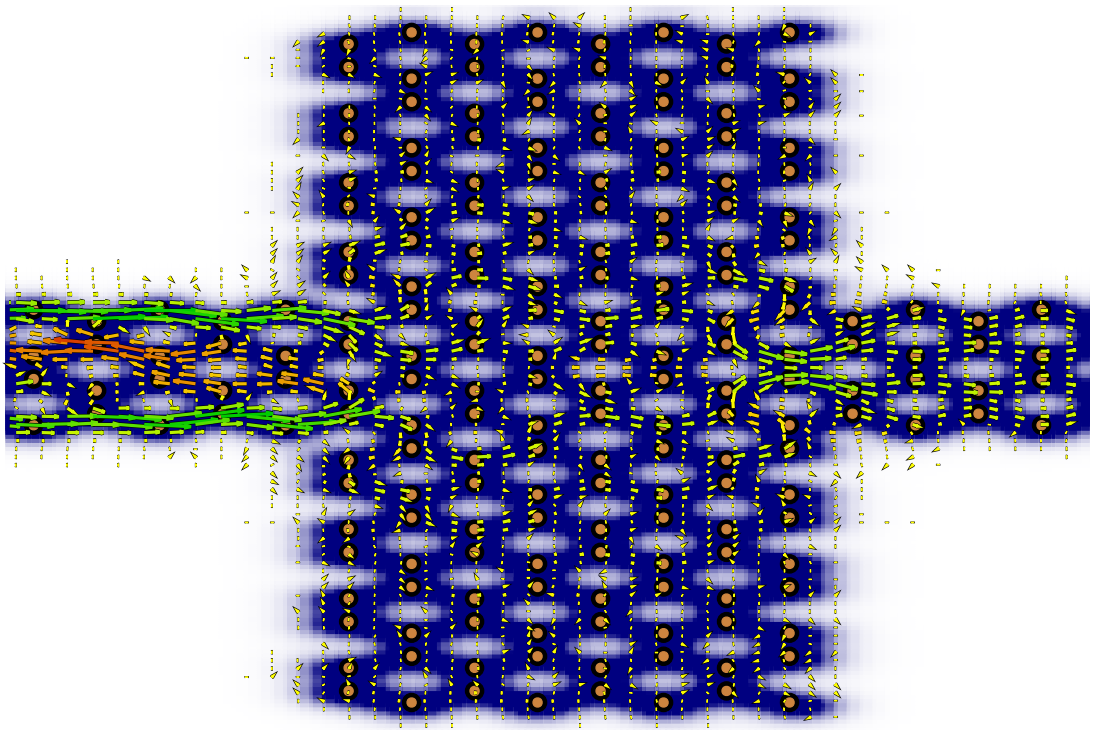

Figure 6.9: Local current density distributions of a wing GNR at 0.5 eV above fermi levels. Part of current gets reflected in the middle. The rest gets transmitted and spread out into the both sides of the wider part of GNR

two energy levels. The reason is that the wedge-shaped constriction behaves like a quantum dot and opens up a transport gap at low energy ranges due to quantum confinement [251]. At higher energies of 1eV and 2eV above Fermi level, as shown in Fig. 6.8.c and 6.8.d respectively, part of the current can pass through the constriction. Although the current may have turbulent features, the transmitted current mainly flows along the edge and forms streamline patterns.

In contrast, current can get transmitted in the wing structure GNRS [252] at all tested energy levels. Fig. 6.9 shows the local current at 0.5 eV above fermi level. Part of current gets reflected in the middle before it enter into the wider part of GNR. The rest gets transmitted and spread out to the both sides of the wider part.

To connect electronic devices in non-linear geometries, other shapes of GNRs are needed. Several methods exist for fabricating GNR in various shapes [253, 23]. In the case of bent geometries within GNRs, also called nano wiggles, the bend angle affects the transmission of electrons [254]. Using the injecting potential method, the transport properties of bent GNRs can also be investigated. Fig. 6.10 shows a short hydrogen-terminated bent GNR with a 60° bend angle with electrons injected at several energies. At lower energies, strong loop currents are observed as the change of direction in the GNR reflects most of the current. With higher energies, less loop currents are present, and the GNR should have better transport properties for higher energies.

6.3.4 Molecular Devices

In this section we present a prototypical examples of transport in molecules [255, 256] concentrating on interference effects. Quantum interference plays an important part in the transport property of molecular devices [257, 258]. One such molecule with strong quantum effects is anthraquinone which contains two oxygen atoms that disrupt the current flow despite all atoms belonging to the same *pi*-bonded system due to cross conjugation [259]. Theorists have predicted that cross conjugation can lead to strong quantum-interference

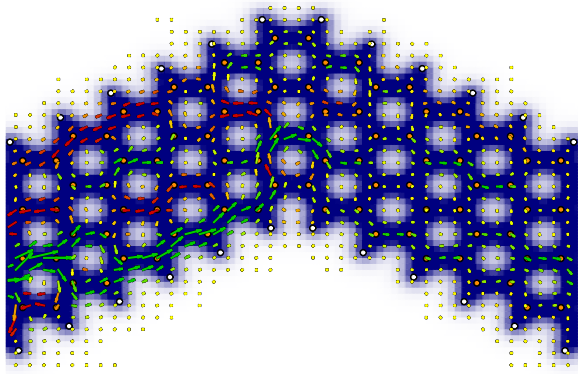

(a)

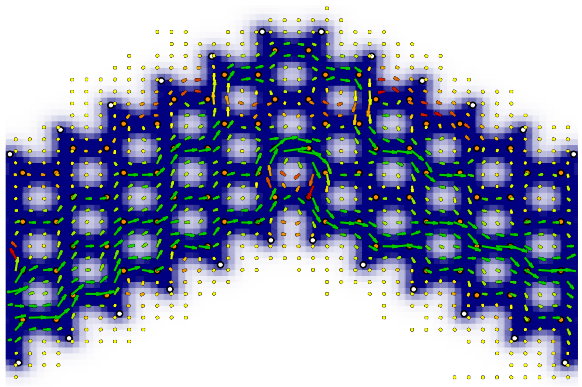

(b)

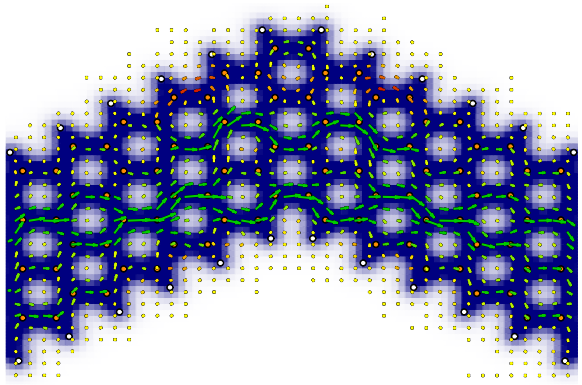

(c)

Figure 6.10: A bent GNR with electrons injected at various energies. Plot (a) shows injection at 0.2 eV above the Fermi energy with transmission reflected. Plot (b) shows injection at 0.5 eV above the Fermi energy with some transmission and loop currents. Plot (c) shows injection at 1.0 eV above the Fermi energy with significantly reduced loop current.

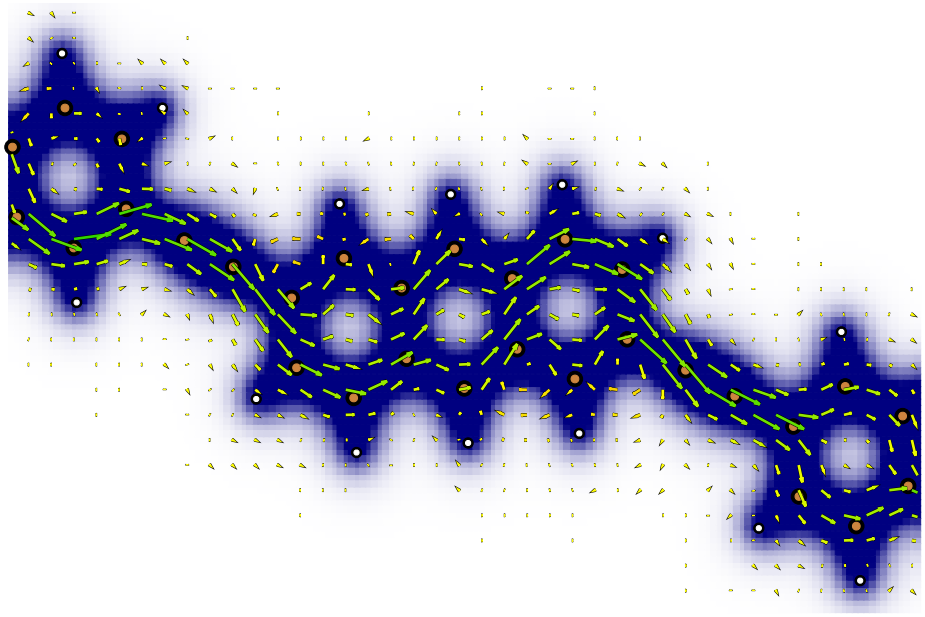

(a)

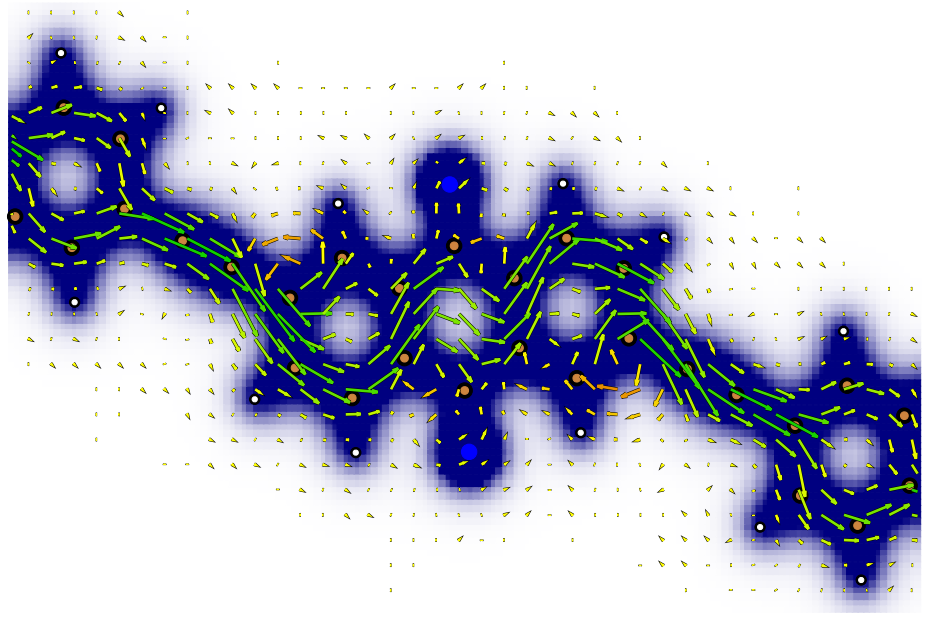

(b)

Figure 6.11: Plot (a) shows the local current distribution of anthracene core at energy 0.5 eV above Fermi level. Current flows along the bonded carbon atoms. Plot (b) shows local currents distribution of anthraquinone core at energy 0.5 eV above Fermi level. Current flows through the non-bonded carbon atoms in the middle ring.

effects[260]. Recent experiments confirmed the prediction by electrical measurements on anthraquinone and anthracene. The π bond network in anthracene is considered to be linear conjugation because it has alternating single and double carbon-carbon bonds. It was found that the linear-conjugation of anthracene is at least 10 times more conductive than the cross-conjugated π bond network of anthraquinone [257]. To understand how quantum interference affects electron transport, we investigate the local currents of those two molecules. Fig. 6.11.a and Fig. 6.11.b show the local current distribution of anthracene and anthraquinone at 0.5 eV above Fermi level respectively. In anthracene, the current splits into two parts and mainly flows along the carbon chain. In anthraquinone, the electron does not flow along the carbon chain. Instead it hops through the non-bonded carbon atoms in the middle and the hopping is very weak according to Neto *et al.* [202]. The charge density distribution shows a high localized density near the oxygen atoms (dark blue dots) which destroys the linear conjugated pathway and pushes the electrons to flow through the non-bonded carbon atoms. Besides, one observes small loop currents at both ends of the anthraquinone core. The cross conjugation breaks electron pathway through bonded carbon atoms and therefore greatly reduces the conductance.

6.3.5 Black Phosphorus

Black phosphorus has received significant attention lately as a 2.5D material with interesting semiconductor properties [262]. Fig. 6.12 shows a 1.5 nm wide ribbon of mono-layer black phosphorus. Interestingly, with an injection energy of 0.5 eV, there is current that proceeds along the edge of the nanoribbon. This edge current is probably due to the unpassivated bonds on the edge atoms. However, if a state with energy 1.0 eV is injected, the wave function is nearly completely reflected, and does not produce substantial current across the system. When a state with energy 1.5 eV is injected, an energy corresponding to the experimental band gap for mono-layer black phosphorus, the electrons are transmitted [261]. This result indicates that edge states and defect can effect the conduction of elec-

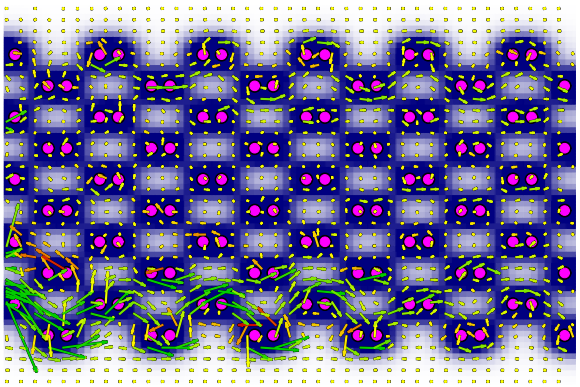

(a)

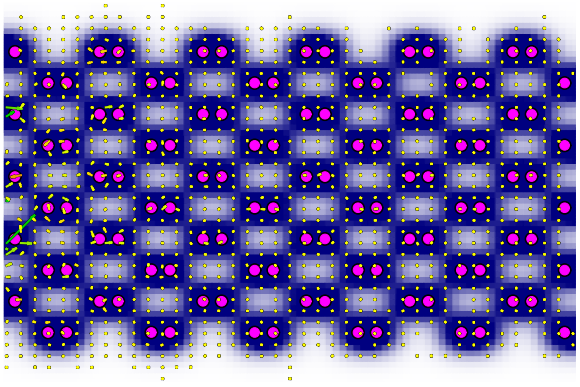

(b)

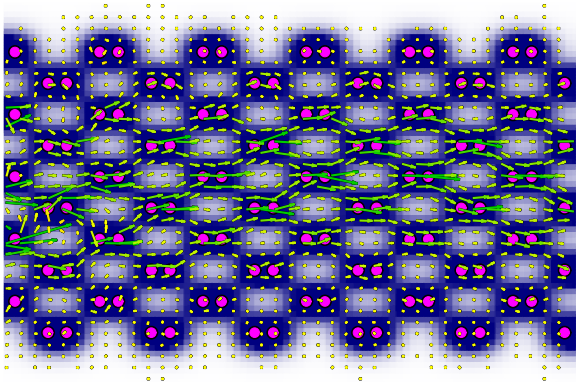

(c)

Figure 6.12: A 1.5 nm wide segment of black phosphorus with electrons injected at various energies. Plot (a) shows injection at 0.5 eV above the Fermi energy with current along the edge due to unsaturated atoms. Plot (b) shows injection at 1.0 eV above the Fermi energy showing near completely reflected. Plot (c) shows injection at 1.5 eV above the Fermi energy showing transmission. The band gap for mono-layer black phosphorus is around 1.5 eV [261].

trons in black phosphorus, as stated above for graphene. One notices that the current on the two sides of the system is not equal. The reason of this is that the position of the injection point is not symmetric with respect to the atomic structure. The injection point was in the middle in all previous examples, and the current developed into a symmetric pattern. This case shows the dependence of the current distribution on the initial injection geometry and simulates an experiment where the electron source, e.g. a scanning tunneling microscope tip is situated at a given point. One expects, that if the simulation cell is large enough, than the current becomes more symmetric far away from the injection point.

6.4 Summary

As a summary, we studied local electron pathway in ZGNR, molecules, and black phosphorus using a complex injecting potential method. The presented approach has several computational advantages. The local current is calculated with a simple time propagation in a finite system without the need of semi-infinite leads. Unlike localized atomic orbitals, the real-space basis is flexible enough to represent the current carrying states. The current can be calculated for any desired energy, and the approach can be readily extended for time-dependent transport problems, e.g. to study the effect of laser excitation. The present work used a single point source with a given energy, future work is planned to use wave packets and more extended sources.

In the presented computational studies we have found, that in pristine ZGNR, the current mainly flows along the carbon chain. Using hydrogen atoms to saturate the dangling carbon bonds at the edge of ZGNR, edge current backflow is suppressed and a more consistent streamline current pattern is achieved. In bilayer ZGNR, the current flow spreads into both layers and flow along the along the corresponding π bonds of each layer. In boron and nitrogen doped nanoribbons, the doped site hinders the electron flow and results in poor conductance. Nevertheless, in the case of boron and nitrogen co-doped nanoribbon, the current pattern is similar to that in the pristine ZGNR, due to the compensation effect of

valence electrons of boron and nitrogen atom and the restoration of sp^2 network. In the hydrogen atom adsorbed GNR, the current pattern is dependent upon the site of the adsorbed hydrogen atom. In constricted nanoribbons, we show that little current can be transmitted in low energies. At higher energy levels, parts of current can flow through the constricted channel. In the wing structure GNR, part of current get transmitted at all tested energy levels. Similarly to constricted GNRs, bent GNRs also show energies where the current is reflected. We also studied the current flow in molecules anthracene and anthraquinone. Due to the cross-conjugation, the electrons flow through the non-bonded carbon atoms in anthraquinone which results in the poor conductance compared to anthracene. Unpassivated black phosphorus shows edge currents for energies below the band gap, and streamline flow at energies near the bandgap. In the future, we will investigate the current path in other low dimensional materials, such as transition metal dichalcogenides, and in material junctions which also play an important role in determining device performance.

Chapter 7

Conclusion

In this dissertation, we have applied ab initio simulations to investigate the local electron transport through various nanostructures, including graphene nanoribbon, molecules and black phosphorus. The simluation tool is the time-dependent density functional theory.

In Chapter 2 we presented the formalism used in this thesis. We reviewed the density functional and time-dependent density functional theory, including the Hohenberg-Kohn theorem, Runge-Gross theorem, Kohn-Sham equations, approximation to the exchange and correlation functionals, and the time propagator. We then introduced the two approaches we used in this thesis to simulate the local electron transport, which are the bias potential and complex injecting potential within the framework of the time-dependent density functional theory.

In Chapter 3 we investigated the numerical stability and accuracy of two subspace propagation methods to solve the time-dependent Kohn-Sham equations. The bases considered are the Lnczos basis and the adiabatic eigenbasis. The results are compared to a benchmark fourth-order Taylor expansion of the time propagator. By making use of a multiscale algorithm where propagation of the orbitals is performed with small time steps and basis updating is performed on a larger time step, the computational efficiency of the subspace methods were improved over the Taylor benchmark by factors on the order of 2–3 (see Table 4.1). The Lánczos basis propagation proved to give a reasonably accurate optical absorption spectrum over the entire energy range considered, while the adiabatic eigenbasis propagation only gave accurate results at low energies. Additionally, both subspace methods gave relatively stable propagations with only minor deviations from energy conservation.

Chapter 4 we presented a new method for time propagation of the coupled Maxwell

and time-dependent Kohn-Sham (TDKS) equation. The new approach uses a simultaneous fourth-order Runge-Kuttabased propagation of the vector potential and the Kohn-Sham orbitals. We have compared the approach to conventional fourth-order Taylor propagation and predictor-corrector methods. While the PC method was shown to have a divergence problem dependent on the time step, the SRK4 method can be used for long propagations without divergence. In our test case, the PC method with a time step of $0.02 a.u.$ gave reasonable results for a propagation time of $2000 a.u.$ However, even with this small time step, increasing numerical inaccuracies in the vector potential were observed. The SRK4 method, in contrast, gave a more stable propagation with a larger time step of 0.05 a.u. The SRK4 method has shown negligible dependence on k-point sampling. Compared to the conventional fourth-order Taylor propagation and predictor-corrector method, the new approach has the advantages of higher computational performance, greater stability, better accuracy, and faster convergence.

In Chapter 5 we studied the spatial current distribution in H-terminated zigzag graphene nanoribbons under electrical bias using time-dependent density-functional theory solved on a real-space grid. A projected complex absorbing potential is used to minimize the effect of reflection at simulation cell boundary and proven to be effective at low bias voltage. The calculations show that the current flows mainly along the edge atoms in the hydrogen terminated pristine ZGNRs. When a vacancy is introduced to the ZGNRs, loop currents emerge at the ribbon edge due to electrons hopping between carbon atoms of the same sublattice. The loop currents hinder the flow of the edge current, resulting in the poor electrical conductivity.

In Chapter 6 We construct a complex potential to mimic conduction in nanoscale systems by injecting electrons into the conduction band. The method allows for the calculation of the current density vectors within the medium, as a function of energy of the conducting electron. Using this method, we investigate the electron pathway in graphene nanoribbons in various structures, in molecular junctions, and in black phosphorus nanoribbons. By an-

alyzing current flow through the structures, we find strong dependence on the structure and energy of the injected electrons. In pristine ZGNR, the current mainly flows along the carbon chain except at edges where loop current cause electron backflow due to the unsaturated carbon bonds. Using hydrogen atoms to saturate the dangling carbon bonds at the edge of ZGNR, edge current backflow is suppressed and a more consistent streamline current pattern is achieved. In bilayer ZGNR, the injected electrons will spread into both layers and flow along the along the corresponding π bonds of each layer. In boron or nitrogen doped nanoribbons, the dopants hinders the electron flow and results in the poor conductance. Nevertheless, in the case of boron and nitrogen co-doped nanoribbon, the current pattern similar to that in the pristine ZGNR is observed due to the compensation effect of valence electrons of boron and nitrogen atom and the restoration of sp^2 network. In hydrogen atom adsorbed GNR, we find strong adsorption site dependance of current pattern. In constricted nanoribbons, we show that little current can be transmitted in low energies due to the transport gap opened up by quantum confinement. At higher energy levels, parts of current can flow through the constricted channel. In wing structure GNR, current can be transmitted at all tested energy levels Similarly to constricted GNRs, current gets reflected at low energy levels. We also studied the current flow in molecule anthracene and anthraquinone. Due to the cross-conjugation, the electrons flow through the non-bonded carbon atoms in anthraquinone which results in the poor conductance compared to anthracene. Unpassivated black phosphorus shows edge currents for energies below the band gap, and streamline flow at energies near the bandgap. An understanding of the local electron pathway, the underlying physics behind the measured global transport properties, is important for nano scale device application.

BIBLIOGRAPHY

[1] W. Kohn and L. J. Sham. Self-consistent equations including exchange and correlation effects. *Phys. Rev.*, 140(4A):A1133–A1138, Nov 1965.

[2] J. J. Palacios, A. J. Pérez-Jiménez, E. Louis, E. SanFabián, and J. A. Vergés. First-principles phase-coherent transport in metallic nanotubes with realistic contacts. *Phys. Rev. Lett.*, 90(10):106801, Mar 2003.

[3] K. Stokbro, J. Taylor, M. Brandbyge, J. L. Mozos, and P. Ordejn. Theoretical study of the nonlinear conductance of di-thiol benzene coupled to au(111) surfaces via thiol and thiolate bonds. *Computational Materials Science*, 27(1-2):151 – 160, 2003.

[4] Eldon G. Emberly and George Kirczenow. Models of electron transport through organic molecular monolayers self-assembled on nanoscale metallic contacts. *Phys. Rev. B*, 64(23):235412, Nov 2001.

[5] Jeremy Taylor, Hong Guo, and Jian Wang. Ab initio modeling of quantum transport properties of molecular electronic devices. *Phys. Rev. B*, 63(24):245407, Jun 2001.

[6] Marco Buongiorno Nardelli, J.-L. Fattebert, and J. Bernholc. $o(n)$ real-space method for ab initio quantum transport calculations: Application to carbon nanotube–metal contacts. *Phys. Rev. B*, 64(24):245423, Dec 2001.

[7] Yongqiang Xue, Supriyo Datta, and Mark A. Ratner. Charge transfer and "band lineup" in molecular electronic devices: A chemical and numerical interpretation. *J. Chem. Phys.*, 115(9):4292–4299, 2001.

[8] K.S. Thygesen and K.W. Jacobsen. Molecular transport calculations with wannier functions. *Chemical Physics*, 319(1-3):111 – 125, 2005. Molecular Charge Transfer

in Condensed Media - from Physics and Chemistry to Biology and Nanoengineering in honour of Alexander M. Kuznetsov on his 65th birthday.

[9] San-Huang Ke, Harold U. Baranger, and Weitao Yang. Electron transport through molecules: Self-consistent and non-self-consistent approaches. *Phys. Rev. B*, 70(8):085410, Aug 2004.

[10] Pedro A. Derosa and Jorge M. Seminario. Electron transport through single molecules: scattering treatment using density functional and green function theories. *The Journal of Physical Chemistry B*, 105(2):471–481, 2001.

[11] S. Sanvito, C. J. Lambert, J. H. Jefferson, and A. M. Bratkovsky. General green's-function formalism for transport calculations with *spd* hamiltonians and giant magnetoresistance in co- and ni-based magnetic multilayers. *Phys. Rev. B*, 59(18):11936–11948, May 1999.

[12] Xinran Wang, Yijian Ouyang, Xiaolin Li, Hailiang Wang, Jing Guo, and Hongjie Dai. Room-temperature all-semiconducting sub-10-nm graphene nanoribbon field-effect transistors. *Phys. Rev. Lett.*, 100:206803, May 2008.

[13] Xinran Wang and Hongjie Dai. Etching and narrowing of graphene from the edges. *Nature Chemistry*, 2(8):661–665, 2010.

[14] Melinda Y. Han, Juliana C. Brant, and Philip Kim. Electron transport in disordered graphene nanoribbons. *Phys. Rev. Lett.*, 104:056801, Feb 2010.

[15] Wan Sik Hwang, Kristof Tahy, Xuesong Li, Huili (Grace) Xing, Alan C. Seabaugh, Chun Yung Sung, and Debdeep Jena. Transport properties of graphene nanoribbon transistors on chemical-vapor-deposition grown wafer-scale graphene. *Applied Physics Letters*, 100(20):203107, 2012.

[16] Patrick B. Bennett, Zahra Pedramrazi, Ali Madani, Yen-Chia Chen, Dimas G. de Oteyza, Chen Chen, Felix R. Fischer, Michael F. Crommie, and Jeffrey Bokor. Bottom-up graphene nanoribbon field-effect transistors. *Applied Physics Letters*, 103(25):253114, 2013.

[17] Qing Wang, Ryo Kitaura, Shoji Suzuki, Yuhei Miyauchi, Kazunari Matsuda, Yuta Yamamoto, Shigeo Arai, and Hisanori Shinohara. Fabrication and in situ transmission electron microscope characterization of free-standing graphene nanoribbon devices. *ACS Nano*, 10(1):1475–1480, 2016. PMID: 26731015.

[18] Leonardo Vicarelli, Stephanie J. Heerema, Cees Dekker, and Henny W. Zandbergen. Controlling defects in graphene for optimizing the electrical properties of graphene nanodevices. *ACS Nano*, 9(4):3428–3435, 2015. PMID: 25864552.

[19] Yen-Chia. Chen, Ting. Cao, Chen. Chen, Zahra. Pedramrazi, Danny. Haberer, de OteyzaDimas G., Felix R. Fischer, Steven G. Louie, and Michael F. Crommie. Molecular bandgap engineering of bottom-up synthesized graphene nanoribbon heterojunctions. *Nature Nanotechnology*, 10:156, Feb 2015.

[20] Yen-Chia Chen, Dimas G. de Oteyza, Zahra Pedramrazi, Chen Chen, Felix R. Fischer, and Michael F. Crommie. Tuning the band gap of graphene nanoribbons synthesized from molecular precursors. *ACS Nano*, 7(7):6123–6128, 2013. PMID: 23746141.

[21] Jayeeta Lahiri, You Lin, Pinar Bozkurt, Ivan I. Oleynik, and Matthias Batzill. An extended defect in graphene as a metallic wire. *Nat Nano*, 5(5):326–329, May 2010.

[22] Rosanna Larciprete, Stefano Colonna, Fabio Ronci, Roberto Flammini, Paolo Lacovig, Nicoleta Apostol, Antonio Politano, Peter Feulner, Dietrich Menzel, and Silvano Lizzit. Self-assembly of graphene nanoblisters sealed to a bare metal surface. *Nano Letters*, 16(3):1808–1817, 2016. PMID: 26829243.

[23] Patrick Han, Kazuto Akagi, Filippo Federici Canova, Ryota Shimizu, Hiroyuki Oguchi, Susumu Shiraki, Paul S. Weiss, Naoki Asao, and Taro Hitosugi. Self-assembly strategy for fabricating connected graphene nanoribbons. *ACS Nano*, 9(12):12035–12044, 2015. PMID: 26588477.

[24] Lukas Dssel, Lileta Gherghel, Xinliang Feng, and Klaus Mllen. Graphene nanoribbons by chemists: Nanometer-sized, soluble, and defect-free. *Angewandte Chemie International Edition*, 50(11):2540–2543, 2011.

[25] S. Datta. *Electronic transport in mesoscopic systems*. Cambridge University Press, 1997.

[26] Massimiliano Di Ventra. *Electrical Transport in Nanoscale Systems*. Cambridge University Press, 2008.

[27] Supriyo Datta. *Electronic Transport in Mesoscopic Systems*. Cambridge University Press, Cambridge, 1997.

[28] Yongqiang Xue, Supriyo Datta, and Mark A. Ratner. Charge transfer and band lineup in molecular electronic devices: A chemical and numerical interpretation. *The Journal of Chemical Physics*, 115(9):4292–4299, 2001.

[29] Massimiliano Di Ventra. *Electrical Transport in Nanoscale Systems*. Cambridge University Press, Cambridge, 2008.

[30] Jeremy Taylor, Hong Guo, and Jian Wang. Ab initio modeling of quantum transport properties of molecular electronic devices. *Physical Review B*, 63(24):245407, 2001.

[31] Sergey V Faleev, François Léonard, Derek A Stewart, and Mark van Schilfgaarde. Ab initio tight-binding lmto method for nonequilibrium electron transport in nanosystems. *Physical Review B*, 71(19):195422, 2005.

[32] A. Lubk, A. Béché, and J. Verbeeck. Electron microscopy of probability currents at atomic resolution. *Phys. Rev. Lett.*, 115:176101, Oct 2015.

[33] D. A. Bandurin, I. Torre, R. Krishna Kumar, M. Ben Shalom, A. Tomadin, A. Principi, G. H. Auton, E. Khestanova, K. S. Novoselov, I. V. Grigorieva, L. A. Ponomarenko, A. K. Geim, and M. Polini. Negative local resistance caused by viscous electron backflow in graphene. *Science*, 351(6277):1055–1058, 2016.

[34] K. Chang, A. Eichler, J. Rhensius, L. Lorenzelli, and C. L. Degen. Nanoscale imaging of current density with a single-spin magnetometer. *Nano Letters*, 17(4):2367–2373, 2017. PMID: 28329445.

[35] Jean-Philippe Tetienne, Nikolai Dontschuk, David A. Broadway, Alastair Stacey, David A. Simpson, and Lloyd C. L. Hollenberg. Quantum imaging of current flow in graphene. *Science Advances*, 3(4), 2017.

[36] Efthimios Kaxiras. *Atomic and electronic structure of solids*. Cambridge University Press, 2003.

[37] D. M. Ceperley and B. J. Alder. Ground state of the electron gas by a stochastic method. *Phys. Rev. Lett.*, 45:566–569, Aug 1980.

[38] J. P. Perdew and Alex Zunger. Self-interaction correction to density-functional approximations for many-electron systems. *Phys. Rev. B*, 23:5048–5079, May 1981.

[39] Argyrios Tsolakidis, Daniel Sánchez-Portal, and Richard M. Martin. Calculation of the optical response of atomic clusters using time-dependent density functional theory and local orbitals. *Phys. Rev. B*, 66(23):235416, 2002.

[40] Argyrios Tsolakidis and Efthimios Kaxiras. A tddft study of the optical response of dna bases, base pairs, and their tautomers in the gas phase. *The Journal of Physical Chemistry A*, 109(10):2373–2380, 2005.

[41] Hannah E. Johnson and Christine M. Aikens. Electronic structure and tddft optical absorption spectra of silver nanorods. *The Journal of Physical Chemistry A*, 113(16):4445–4450, 2009.

[42] Christine M. Aikens, Shuzhou Li, and George C. Schatz. From discrete electronic states to plasmons: Tddft optical absorption properties of ag n (n = 10, 20, 35, 56, 84, 120) tetrahedral clusters. *The Journal of Physical Chemistry C*, 112(30):11272–11279, 2008.

[43] Joseph A Driscoll, Sergiy Bubin, William R French, and Kalman Varga. Time-dependent density functional study of field emission from nanotubes composed of C, BN, SiC, Si, and GaN. *Nanotechnology*, 22(28):285702, 2011.

[44] Joseph A. Driscoll, Sergiy Bubin, and Kálmán Varga. Laser-induced electron emission from nanostructures: A first-principles study. *Phys. Rev. B*, 83(23):233405, 2011.

[45] Joseph A. Driscoll, Brandon Cook, Sergiy Bubin, and Kálmán Varga. First-principles study of field emission from carbon nanotubes and graphene nanoribbons. *J. Appl. Phys.*, 110(2):024304, 2011.

[46] J. A. Driscoll and K. Varga. Time-dependent density-functional study of field emission from tipped carbon nanotubes. *Phys. Rev. B*, 80(24):245431, 2009.

[47] Xi Chu and Shih-I Chu. Time-dependent density-functional theory for molecular processes in strong fields: Study of multiphoton processes and dynamical response of individual valence electrons of N_2 in intense laser fields. *Phys. Rev. A*, 64(6):063404, 2001.

[48] Sergiy Bubin, Mackenzie Atkinson, Kálmán Varga, Xinhua Xie, Stefan Roither, Daniil Kartashov, Andrius Baltuška, and Markus Kitzler. Strong laser-pulse-

driven ionization and Coulomb explosion of hydrocarbon molecules. *Phys. Rev. A*, 86:043407, 2012.

[49] Sergiy Bubin and Kálmán Varga. First-principles time-dependent simulation of laser assisted desorption of hydrogen atoms from H-Si(111) surface. *Appl. Phys. Lett.*, 98(15):154101, 2011.

[50] Sergiy Bubin and Kálmán Varga. Electron-ion dynamics in laser-assisted desorption of hydrogen atoms from H-Si(111) surface. *J. Appl. Phys.*, 110(6):064905, 2011.

[51] S. Bubin and Kálmán Varga. Electron and ion dynamics in graphene and graphane fragments subjected to high-intensity laser pulses. *Phys. Rev. B*, 85:205441, 2012.

[52] Arthur Russakoff, Sergiy Bubin, Xinhua Xie, Sonia Erattupuzha, Markus Kitzler, and Kálmán Varga. Time-dependent density-functional study of the alignment-dependent ionization of acetylene and ethylene by strong laser pulses. *Phys. Rev. A*, 91:023422, Feb 2015.

[53] Arthur Russakoff and Kálmán Varga. Time-dependent density-functional study of the ionization and fragmentation of c_2h_2 and h_2 by strong circularly polarized laser pulses. *Phys. Rev. A*, 92:053413, Nov 2015.

[54] Jun Haruyama, Chunping Hu, and Kazuyuki Watanabe. First-principles molecular-dynamics simulation of biphenyl under strong laser pulses by time-dependent density-functional theory. *Phys. Rev. A*, 85:062511, 2012.

[55] John Heslar, Dmitry A. Telnov, and Shih-I Chu. Time-dependent density-functional theory with optimized effective potential and self-interaction correction and derivative discontinuity for the treatment of double ionization of He and Be atoms in intense laser fields. *Phys. Rev. A*, 87:052513, 2013.

[56] M. Isla and J. A. Alonso. Interaction of the charged deuterium cluster D_3^+ with femtosecond laser pulse. *J. Phys. Chem. C*, 111(48):17765–17772, 2007.

[57] Ester Livshits and Roi Baer. Time-dependent density-functional studies of the D_2 coulomb explosion. *J. Phys. Chem. A*, 110(27):8443–8450, 2006.

[58] Arkady V. Krasheninnikov, Yoshiyuki Miyamoto, and David Tománek. Role of electronic excitations in ion collisions with carbon nanostructures. *Phys. Rev. Lett.*, 99(1):016104, 2007.

[59] Sergiy Bubin, Bin Wang, Sokrates Pantelides, and Kálmán Varga. Simulation of high-energy ion collisions with graphene fragments. *Phys. Rev. B*, 85:235435, 2012.

[60] Ryan Hatcher, Matthew Beck, Alan Tackett, and Sokrates T. Pantelides. Dynamical Effects in the Interaction of Ion Beams with Solids. *Phys. Rev. Lett.*, 100:103201, Mar 2008.

[61] Erich Runge and E. K. U. Gross. Density-functional theory for time-dependent systems. *Phys. Rev. Lett.*, 52:997–1000, Mar 1984.

[62] Robert van Leeuwen. Mapping from densities to potentials in time-dependent density-functional theory. *Physical review letters*, 82(19):3863, 1999.

[63] Alberto Castro, Miguel A. L. Marques, and Angel Rubio. Propagators for the time-dependent Kohn–Sham equations. *J. Chem. Phys.*, 121(8):3425–3433, 2004.

[64] Alberto Castro, Miguel AL Marques, and Angel Rubio. Propagators for the time-dependent kohn–sham equations. *The Journal of Chemical Physics*, 121(8):3425–3433, 2004.

[65] Joseph A Driscoll, Brandon Cook, Sergiy Bubin, and Kálmán Varga. First-principles study of field emission from carbon nanotubes and graphene nanoribbons. *Journal of Applied Physics*, 110(2):024304, 2011.

[66] Yongqiang Xue, Supriyo Datta, and Mark A Ratner. First-principles based matrix green's function approach to molecular electronic devices: general formalism. *Chemical Physics*, 281(2):151–170, 2002.

[67] Massimiliano Di Ventra. *Electrical transport in nanoscale systems*, volume 14. Cambridge University Press Cambridge, 2008.

[68] David E. Manolopoulos. Derivation and reflection properties of a transmission-free absorbing potential. *The Journal of Chemical Physics*, 117(21):9552–9559, 2002.

[69] Kálmán Varga. Time-dependent density functional study of transport in molecular junctions. *Phys. Rev. B*, 83:195130, May 2011.

[70] N. Troullier and José Luís Martins. Efficient pseudopotentials for plane-wave calculations. *Phys. Rev. B*, 43:1993–2006, Jan 1991.

[71] Shunsuke A Sato and Kazuhiro Yabana. Efficient basis expansion for describing linear and nonlinear electron dynamics in crystalline solids. *Phys. Rev. B*, 89(22):224305, 2014.

[72] Ingrid Rotter. A non-hermitian hamilton operator and the physics of open quantum systems. *Journal of Physics A: Mathematical and Theoretical*, 42(15):153001, 2009.

[73] Christian E Rüter, Konstantinos G Makris, Ramy El-Ganainy, Demetrios N Christodoulides, Mordechai Segev, and Detlef Kip. Observation of parity-time symmetry in optics. *Nature physics*, 6(3):192, 2010.

[74] Jean Dalibard, Yvan Castin, and Klaus Mølmer. Wave-function approach to dissipative processes in quantum optics. *Physical review letters*, 68(5):580, 1992.

[75] Howard Carmichael. *An open systems approach to quantum optics: lectures presented at the Université Libre de Bruxelles, October 28 to November 4, 1991*, volume 18. Springer Science & Business Media, 2009.

[76] AD McLachlan. A variational solution of the time-dependent schrodinger equation. *Molecular Physics*, 8(1):39–44, 1964.

[77] E Gerjuoy, ARP Rau, and Larry Spruch. A unified formulation of the construction of variational principles. *Reviews of Modern Physics*, 55(3):725, 1983.

[78] Arieh Aviram and Mark A Ratner. Molecular rectifiers. *Chemical Physics Letters*, 29(2):277–283, 1974.

[79] Arthur Russakoff, Yonghui Li, Shenglai He, and Kalman Varga. Accuracy and computational efficiency of real-time subspace propagation schemes for the time-dependent density functional theory. *The Journal of chemical physics*, 144(20):204125, 2016.

[80] E. Runge and E. K. U Gross. Density-functional theory for time-dependent systems. *Phys. Rev. Lett.*, 52(12):997–1000, 1984.

[81] Carsten A. Ullrich and Zeng-hui Yang. A brief compendium of time-dependent density functional theory. *Brazilian Journal of Physics*, 44:154–188, 2014.

[82] Sonia Erattupuzha, Cody Covington, Arthur Russakoff, Erik Lotstedt, Seyedreza Larimian, Václav Hanus, Sergiy Bubin, Markus Koch, Stefanie Graefe, Andrius Baltuska, et al. Enhanced ionization of polyatomic molecules in intense laser pulses is due to energy upshift and field coupling of multiple orbitals. *Journal of Physics B: Atomic, Molecular and Optical Physics*, 2017.

[83] Mark E Casida. Time-dependent density-functional response theory for molecules. *Recent advances in density functional methods*, 1:155, 1995.

[84] M.E. Casida and M. Huix-Rotllant. Progress in time-dependent density-functional theory. *Annu. Rev. Phys. Chem.*, 63(1):287–323, May 2012.

[85] Barry I. Schneider, Lee A. Collins, and S. X. Hu. Parallel solver for the time-dependent linear and nonlinear schrödinger equation. *Phys. Rev. E*, 73:036708, Mar 2006.

[86] Tomoko Akama, Osamu Kobayashi, and Shinkoh Nanbu. Development of efficient time-evolution method based on three-term recurrence relation. *The Journal of Chemical Physics*, 142(20), 2015.

[87] Zhigang Sun and Weitao Yang. Communication: An exact short-time solver for the time-dependent schrdinger equation. *The Journal of Chemical Physics*, 134(4), 2011.

[88] G. Goldstein and D. Baye. Sixth-order factorization of the evolution operator for time-dependent potentials. *Phys. Rev. E*, 70:056703, Nov 2004.

[89] Zhigang Sun, Soo-Y. Lee, Hua Guo, and Dong H. Zhang. Comparison of second-order split operator and chebyshev propagator in wave packet based state-to-state reactive scattering calculations. *The Journal of Chemical Physics*, 130(17), 2009.

[90] Stephen K. Gray and Gabriel G. Balint-Kurti. Quantum dynamics with real wave packets, including application to three-dimensional (j=0)d+h2hd+h reactive scattering. *The Journal of Chemical Physics*, 108(3):950–962, 1998.

[91] D Kosloff and R Kosloff. A fourier method solution for the time dependent schrdinger equation as a tool in molecular dynamics. *Journal of Computational Physics*, 52(1):35 – 53, 1983.

[92] M.D Feit, J.A Fleck, and A Steiger. Solution of the schrdinger equation by a spectral method. *Journal of Computational Physics*, 47(3):412 – 433, 1982.

[93] Rongqing Chen and Hua Guo. A single lanczos propagation method for calculating transition amplitudes. *The Journal of Chemical Physics*, 111(22):9944–9951, 1999.

[94] H. Tal-Ezer and R. Kosloff. An accurate and efficient scheme for propagating the time dependent Schrödinger equation. *J. Chem. Phys.*, 81:3967–3971, 1984.

[95] ANDR D. BANDRAUK and HUIZHONG LU. Exponential propagators (integrators) for the time-dependent schrdinger equation. *Journal of Theoretical and Computational Chemistry*, 12(06):1340001, 2013.

[96] Andr D. Bandrauk, Effat Dehghanian, and Huizhong Lu. Complex integration steps in decomposition of quantum exponential evolution operators. *Chemical Physics Letters*, 419(46):346 – 350, 2006.

[97] Tae Jun Park and J. C. Light. Unitary quantum time evolution by iterative lanczos reduction. *The Journal of Chemical Physics*, 85(10):5870–5876, 1986.

[98] U. Manthe, H. Köppel, and L. S. Cederbaum. Dissociation and predissociation on coupled electronic potential energy surfaces: A three-dimensional wave packet dynamical study. *The Journal of Chemical Physics*, 95(3):1708–1720, 1991.

[99] C Leforestier, R.H Bisseling, C Cerjan, M.D Feit, R Friesner, A Guldberg, A Hammerich, G Jolicard, W Karrlein, H.-D Meyer, N Lipkin, O Roncero, and R Kosloff. A comparison of different propagation schemes for the time dependent Schrödinger equation. *J. Comput. Phys.*, 94(1):59 – 80, 1991.

[100] Uwe Manthe and Frank Matzkies. Quantum calculations of thermal rate constants and reaction probabilities. *Chemical Physics Letters*, 282(5-6):442 – 449, 1998.

[101] Edward S. Smyth, Jonathan S. Parker, and K.T. Taylor. Numerical integration of the time-dependent schrödinger equation for laser-driven helium. *Computer Physics Communications*, 114(13):1 – 14, 1998.

[102] John D. Farnum and David A. Mazziotti. Spectral difference lanczos method for effi-

cient time propagation in quantum control theory. *The Journal of Chemical Physics*, 120(13):5962–5967, 2004.

[103] Renate Pazourek, Johannes Feist, Stefan Nagele, and Joachim Burgdörfer. Attosecond streaking of correlated two-electron transitions in helium. *Phys. Rev. Lett.*, 108:163001, Apr 2012.

[104] Ana Laura Frapiccini, Aliou Hamido, Sebastian Schröter, Dean Pyke, Francisca Mota-Furtado, Patrick F. O'Mahony, Javier Madroñero, Johannes Eiglsperger, and Bernard Piraux. Explicit schemes for time propagating many-body wave functions. *Phys. Rev. A*, 89:023418, Feb 2014.

[105] M Lehner and M Jungen. Lanczos wave packet propagation on coupled potential energy surfaces: the three body predissociation of rotating d 3 and h 3. *Journal of Physics B: Atomic, Molecular and Optical Physics*, 48(3):035101, 2015.

[106] Zuojing Chen and Eric Polizzi. Spectral-based propagation schemes for time-dependent quantum systems with application to carbon nanotubes. *Phys. Rev. B*, 82:205410, Nov 2010.

[107] Zhi Wang, Shu-Shen Li, and Lin-Wang Wang. Efficient real-time time-dependent density functional theory method and its application to a collision of an ion with a 2D material. *Physical Review Letters*, 114(6), Feb 2015.

[108] Cody Covington, Daniel Kidd, Justin Gilmer, and Kálmán Varga. Simulation of electron dynamics subject to intense laser fields using a time-dependent volkov basis. *Phys. Rev. A*, 95:013414, Jan 2017.

[109] K. Yabana and G. F. Bertsch. Time-dependent local-density approximation in real time. *Phys. Rev. B*, 54(7):4484–4487, 1996.

[110] G. F. Bertsch, J.-I. Iwata, Angel Rubio, and K. Yabana. Real-space, real-time method for the dielectric function. *Phys. Rev. B*, 62(12):7998–8002, 2000.

[111] P. Ehrenfest. Bemerkung über die angenäherte Gültigkeit der klassischen Mechanik innerhalb der Quantenmechanik. *Z. Phys.*, 45:455–457, 1927.

[112] Xiaosong Li, John C. Tully, H. Bernhard Schlegel, and Michael J. Frisch. Ab initio ehrenfest dynamics. *J. Chem. Phys.*, 123(8):084106, 2005.

[113] E. L. Briggs, D. J. Sullivan, and J. Bernholc. Real-space multigrid-based approach to large-scale electronic structure calculations. *Phys. Rev. B*, 54:14362–14375, Nov 1996.

[114] Octopus.

[115] James R. Chelikowsky, N. Troullier, and Y. Saad. Finite-difference-pseudopotential method: Electronic structure calculations without a basis. *Phys. Rev. Lett.*, 72:1240–1243, Feb 1994.

[116] N. Troullier and José Luriaas Martins. Efficient pseudopotentials for plane-wave calculations. *Phys. Rev. B*, 43(3):1993–2006, 1991.

[117] J. P. Perdew and Alex Zunger. Self-interaction correction to density-functional approximations for many-electron systems. *Phys. Rev. B*, 23(10):5048–5079, 1981.

[118] Cornelius Lanczos. *An iteration method for the solution of the eigenvalue problem of linear differential and integral operators*. United States Governm. Press Office, 1950.

[119] Shunsuke A. Sato and Kazuhiro Yabana. Efficient basis expansion for describing linear and nonlinear electron dynamics in crystalline solids. *Phys. Rev. B*, 89:224305, Jun 2014.

[120] Stefan Roither, Xinhua Xie, Daniil Kartashov, Li Zhang, Markus Schöffler, Huailiang Xu, Atsushi Iwasaki, Tomoya Okino, Kaoru Yamanouchi, Andrius Baltuska, and Markus Kitzler. High energy proton ejection from hydrocarbon molecules driven by highly efficient field ionization. *Phys. Rev. Lett.*, 106:163001, 2011.

[121] Alexei N. Markevitch, Dmitri A. Romanov, Stanley M. Smith, and Robert J. Levis. Coulomb Explosion of Large Polyatomic Molecules Assisted by Nonadiabatic Charge Localization. *Phys. Rev. Lett.*, 92:063001, 2004.

[122] Xiaochun Gong, Qiying Song, Qinying Ji, Haifeng Pan, Jingxin Ding, Jian Wu, and Heping Zeng. Strong-field dissociative double ionization of acetylene. *Phys. Rev. Lett.*, 112:243001, 2014.

[123] Constantin Brif, Raj Chakrabarti, and Herschel Rabitz. Control of quantum phenomena: past, present and future. *New J. Phys.*, 12(7):075008, 2010.

[124] Yunquan Liu, Xianrong Liu, Yongkai Deng, Chengyin Wu, Hongbing Jiang, and Qihuang Gong. Selective steering of molecular multiple dissociative channels with strong few-cycle laser pulses. *Phys. Rev. Lett.*, 106:073004, 2011.

[125] Xinhua Xie, Katharina Doblhoff-Dier, Stefan Roither, Markus S. Schöffler, Daniil Kartashov, Huailiang Xu, Tim Rathje, Gerhard G. Paulus, Andrius Baltuška, Stefanie Gräfe, and Markus Kitzler. Attosecond-recollision-controlled selective fragmentation of polyatomic molecules. *Phys. Rev. Lett.*, 109:243001, 2012.

[126] Xinhua Xie, Katharina Doblhoff-Dier, Huailiang Xu, Stefan Roither, Markus S. Schöffler, Daniil Kartashov, Sonia Erattupuzha, Tim Rathje, Gerhard G. Paulus, Kaoru Yamanouchi, Andrius Baltuška, Stefanie Gräfe, and Markus Kitzler. Selective control over fragmentation reactions in polyatomic molecules using impulsive laser alignment. *Phys. Rev. Lett.*, 112:163003, 2014.

[127] Junfeng Ren, Nenad Vukmirović, and Lin-Wang Wang. Nonadiabatic molecular dynamics simulation for carrier transport in a pentathiophene butyric acid monolayer. *Phys. Rev. B*, 87:205117, May 2013.

[128] Yonghui Li, Shenglai He, Arthur Russakoff, and Kálmán Varga. Accurate time propagation method for the coupled maxwell and kohn-sham equations. *Physical Review E*, 94(2):023314, 2016.

[129] Schultze Martin, Bothschafter Elisabeth M., Sommer Annkatrin, Holzner Simon, Schweinberger Wolfgang, Fiess Markus, Hofstetter Michael, Kienberger Reinhard, Apalkov Vadym, Yakovlev Vladislav S., Stockman Mark I., and Krausz Ferenc. Controlling dielectrics with the electric field of light. *Nature*, 493(7430):75–78, jan 2013. 10.1038/nature11720.

[130] Alexander V. Mitrofanov, Aart J. Verhoef, Evgenii E. Serebryannikov, Julien Lumeau, Leonid Glebov, Aleksei Zheltikov, and Andrius Baltuška. Optical detection of attosecond ionization induced by a few-cycle laser field in a transparent dielectric material. *Phys. Rev. Lett.*, 106:147401, Apr 2011.

[131] Ghimire Shambhu, DiChiara Anthony D., Sistrunk Emily, Agostini Pierre, DiMauro Louis F., and Reis David A. Observation of high-order harmonic generation in a bulk crystal. *Nat Phys*, 7(2):138–141, feb 2011. 10.1038/nphys1847.

[132] Hohenleutner M., Langer F., Schubert O., Knorr M., Huttner U., Koch S. W., Kira M., and Huber R. Real-time observation of interfering crystal electrons in high-harmonic generation. *Nature*, 523(7562):572–575, jul 2015.

[133] Neppl S., Ernstorfer R., Cavalieri A. L., Lemell C., Wachter G., Magerl E., Bothschafter E. M., Jobst M., Hofstetter M., Kleineberg U., Barth J. V., Menzel D., Burgdorfer J., Feulner P., Krausz F., and Kienberger R. Direct observation of electron propagation and dielectric screening. *Nature*, 517(7534):342–346, jan 2015.

[134] E Weinan, Jianfeng Lu, and Xu Yang. Effective Maxwell equations from time-dependent density functional theory. *Acta Mathematica Sinica, English Series*, 27(2):339–368, 2011.

[135] Milan Šindelka. Derivation of coupled maxwell-schrödinger equations describing matter-laser interaction from first principles of quantum electrodynamics. *Phys. Rev. A*, 81:033833, Mar 2010.

[136] Lorin E., Chelkowski S., and Bandrauk A. A numerical Maxwell-Schrödinger model for intense laser-matter interaction and propagation. *Computer Physics Communications*, 177(12):908–932, dec 2007.

[137] Erich Runge and E. K. U. Gross. Density-functional theory for time-dependent systems. *Phys. Rev. Lett.*, 52(12):997–1000, Mar 1984.

[138] C. A. Ullrich. *Time-dependent density-functional theory: concepts and applications*. Oxford University Press: Oxford, UK, 2012.

[139] Ole Keller. Local fields in the electrodynamics of mesoscopic media. *Physics Reports*, 268(2-3):85–262, 1996.

[140] Gang Bao, Di Liu, and Songting Luo. A Multiscale Method for Optical Responses of Nanostructures. *SIAM Journal on Applied Mathematics*, 73(2):741–756, 2013.

[141] Neepa T. Maitra, Ivo Souza, and Kieron Burke. Current-density functional theory of the response of solids. *Phys. Rev. B*, 68:045109, Jul 2003.

[142] Camilla Pellegrini, Johannes Flick, Ilya V. Tokatly, Heiko Appel, and Angel Rubio. Optimized effective potential for quantum electrodynamical time-dependent density functional theory. *Phys. Rev. Lett.*, 115:093001, Aug 2015.

[143] Yi Gao and Daniel Neuhauser. Dynamical quantum-electrodynamics embedding:

Combining time-dependent density functional theory and the near-field method. *The Journal of Chemical Physics*, 137(7), 2012.

[144] M. Farzanehpour and I. V. Tokatly. Quantum electrodynamical time-dependent density-functional theory for many-electron systems on a lattice. *Phys. Rev. B*, 90:195149, Nov 2014.

[145] Michael Ruggenthaler, Johannes Flick, Camilla Pellegrini, Heiko Appel, Ilya V. Tokatly, and Angel Rubio. Quantum-electrodynamical density-functional theory: Bridging quantum optics and electronic-structure theory. *Phys. Rev. A*, 90:012508, Jul 2014.

[146] M. Ruggenthaler, F. Mackenroth, and D. Bauer. Time-dependent kohn-sham approach to quantum electrodynamics. *Phys. Rev. A*, 84:042107, Oct 2011.

[147] I. Ahmed, Eng Huat Khoo, Erping Li, and R. Mittra. A hybrid approach for solving coupled maxwell and schrödinger equations arising in the simulation of nanodevices. *Antennas and Wireless Propagation Letters, IEEE*, 9:914–917, 2010.

[148] I. V. Tokatly. Time-dependent density functional theory for many-electron systems interacting with cavity photons. *Phys. Rev. Lett.*, 110:233001, Jun 2013.

[149] Takashi Takeuchi, Shinichiro Ohnuki, and Tokuei Sako. Maxwell-schrödinger hybrid simulation for optically controlling quantum states: A scheme for designing control pulses. *Phys. Rev. A*, 91:033401, Mar 2015.

[150] G. Vignale and Mark Rasolt. Density-functional theory in strong magnetic fields. *Phys. Rev. Lett.*, 59:2360–2363, Nov 1987.

[151] K. Yabana, T. Sugiyama, Y. Shinohara, T. Otobe, and G. F. Bertsch. Time-dependent density functional theory for strong electromagnetic fields in crystalline solids. *Phys. Rev. B*, 85:045134, Jan 2012.

[152] G. F. Bertsch, J.-I. Iwata, Angel Rubio, and K. Yabana. Real-space, real-time method for the dielectric function. *Physical Review B*, 62(12):7998–8002, Sep 2000.

[153] Georg Wachter, Christoph Lemell, Joachim Burgdörfer, Shunsuke A. Sato, Xiao-Min Tong, and Kazuhiro Yabana. Ab initio simulation of electrical currents induced by ultrafast laser excitation of dielectric materials. *Physical Review Letters*, 113(8), Aug 2014.

[154] Shunsuke A. Sato, Yasutaka Taniguchi, Yasushi Shinohara, and Kazuhiro Yabana. Nonlinear electronic excitations in crystalline solids using meta-generalized gradient approximation and hybrid functional in time-dependent density functional theory. *The Journal of Chemical Physics*, 143(22), 2015.

[155] S. A. Sato, Y. Shinohara, T. Otobe, and K. Yabana. Dielectric response of laser-excited silicon at finite electron temperature. *Phys. Rev. B*, 90:174303, Nov 2014.

[156] James R. Chelikowsky, N. Troullier, and Y. Saad. Finite-difference-pseudopotential method: Electronic structure calculations without a basis. *Phys. Rev. Lett.*, 72:1240–1243, Feb 1994.

[157] E. L. Briggs, D. J. Sullivan, and J. Bernholc. Real-space multigrid-based approach to large-scale electronic structure calculations. *Phys. Rev. B*, 54(20):14362–14375, Nov 1996.

[158] K. Yabana, T. Nakatsukasa, J.-I. Iwata, and G. F. Bertsch. Real-time, real-space implementation of the linear response time-dependent density-functional theory. *phys. stat. sol. (b)*, 243(5):1121–1138, Apr 2006.

[159] William H. Press, Saul A. Teukolsky, William T. Vetterling, and Brian P. Flannery. *Numerical Recipes in FORTRAN; The Art of Scientific Computing*. Cambridge University Press, New York, NY, USA, 2nd edition, 1993.

[160] Sosan Cheon, Kenneth David Kihm, Hong goo Kim, Gyuñin Lim, Jae Sung Park, and Joon Sik Lee. How to reliably determine the complex refractive index (ri) of graph ene by using two independent measurement constraints. *Scientific Reports*, 4:6364, Sep 2014.

[161] T Otobe. First-principle description for the high-harmonic generation in a diamond by intense short laser pulse. *Journal of Applied Physics*, 111(9):093112, 2012.

[162] M. Ben-Nun, Jason Quenneville, and Todd J. Martnez. Ab initio multiple spawning: photochemistry from first principles quantum molecular dynamics. *The Journal of Physical Chemistry A*, 104(22):5161–5175, 2000.

[163] Shenglai He, Arthur Russakoff, Yonghui Li, and Kálmán Varga. Time-dependent density-functional theory simulation of local currents in pristine and single-defect zigzag graphene nanoribbons. *Journal of Applied Physics*, 120(3):034304, 2016.

[164] A. K. Geim. Graphene: Status and prospects. *Science*, 324(5934):1530–1534, 2009.

[165] Qingyu Peng, Yibin Li, Xiaodong He, Xuchun Gui, Yuanyuan Shang, Chunhui Wang, Chao Wang, Wenqi Zhao, Shanyi Du, Enzheng Shi, Peixu Li, Dehai Wu, and Anyuan Cao. Graphene nanoribbon aerogels unzipped from carbon nanotube sponges. *Advanced Materials*, 26(20):3241–3247, 2014.

[166] Liying Jiao, Xinran Wang, Georgi Diankov, Hailiang Wang, and Hongjie Dai. Facile synthesis of high-quality graphene nanoribbons. *Nature Nanotechnology*, 5(5):321–325, 2010.

[167] Dmitry V Kosynkin, Amanda L Higginbotham, Alexander Sinitskii, Jay R Lomeda, Ayrat Dimiev, B Katherine Price, and James M Tour. Longitudinal unzipping of carbon nanotubes to form graphene nanoribbons. *Nature*, 458(7240):872–876, 2009.

[168] Eberhard Ulrich Stützel, Thomas Dufaux, Adarsh Sagar, Stephan Rauschenbach, Kannan Balasubramanian, Marko Burghard, and Klaus Kern. Spatially resolved photocurrents in graphene nanoribbon devices. *Applied Physics Letters*, 102(4):043106, 2013.

[169] DA Bandurin, I Torre, R Krishna Kumar, M Ben Shalom, A Tomadin, A Principi, GH Auton, E Khestanova, KS Novoselov, IV Grigorieva, et al. Negative local resistance caused by viscous electron backflow in graphene. *Science*, 351(6277):1055–1058, 2016.

[170] Thomas Lehmann, Dmitry A. Ryndyk, and Gianaurelio Cuniberti. Combined effect of strain and defects on the conductance of graphene nanoribbons. *Phys. Rev. B*, 88:125420, Sep 2013.

[171] Simon M-M Dubois, Alejandro Lopez-Bezanilla, Alessandro Cresti, François Triozon, Blanca Biel, Jean-Christophe Charlier, and Stephan Roche. Quantum transport in graphene nanoribbons: Effects of edge reconstruction and chemical reactivity. *ACS nano*, 4(4):1971–1976, 2010.

[172] Karri Saloriutta, Andreas Uppstu, Ari Harju, and Martti J. Puska. *Ab initio* transport fingerprints for resonant scattering in graphene. *Phys. Rev. B*, 86:235417, Dec 2012.

[173] José Eduardo Padilha, Renato Borges Pontes, Antônio José Roque da Silva, and Adalberto Fazzio. Graphene nanoribbon intercalated with hexagonal boron nitride: Electronic transport properties from ab initio calculations. *Solid State Communications*, 173:24–29, 2013.

[174] XQ Deng, ZH Zhang, GP Tang, ZQ Fan, and CH Yang. Spin filter effects in zigzag-edge graphene nanoribbons with symmetric and asymmetric edge hydrogenations. *Carbon*, 66:646–653, 2014.

[175] Brandon G Cook, William R French, and Kálmán Varga. Electron transport properties of carbon nanotube–graphene contacts. *Applied Physics Letters*, 101(15):153501, 2012.

[176] Liviu P Zârbo and BK Nikolić. Spatial distribution of local currents of massless dirac fermions in quantum transport through graphene nanoribbons. *EPL (Europhysics Letters)*, 80(4):47001, 2007.

[177] Jie-Yun Yan, Ping Zhang, Bo Sun, Hai-Zhou Lu, Zhigang Wang, Suqing Duan, and Xian-Geng Zhao. Quantum blockade and loop current induced by a single lattice defect in graphene nanoribbons. *Phys. Rev. B*, 79:115403, Mar 2009.

[178] Gemma C Solomon, Carmen Herrmann, Thorsten Hansen, Vladimiro Mujica, and Mark A Ratner. Exploring local currents in molecular junctions. *Nature Chemistry*, 2(3):223–228, 2010.

[179] Jan Wilhelm, Michael Walz, and Ferdinand Evers. Ab initio quantum transport through armchair graphene nanoribbons: Streamlines in the current density. *Physical Review B*, 89(19):195406, 2014.

[180] Can Cao, Ling-Na Chen, Meng-Qiu Long, Wei-Rong Huang, and Hui Xu. Electronic transport properties on transition-metal terminated zigzag graphene nanoribbons. *Journal of Applied Physics*, 111(11):113708, 2012.

[181] G. Stefanucci and C.-O. Almbladh. Time-dependent quantum transport: An exact formulation based on tddft. *EPL (Europhysics Letters)*, 67(1):14, 2004.

[182] Gianluca Stefanucci and Carl-Olof Almbladh. Time-dependent partition-free approach in resonant tunneling systems. *Phys. Rev. B*, 69(19):195318, May 2004.

[183] Chiao-Lun Cheng, Jeremy S. Evans, and Troy Van Voorhis. Simulating molecular

conductance using real-time density functional theory. *Phys. Rev. B*, 74:155112, Oct 2006.

[184] S. Kurth, G. Stefanucci, C.-O. Almbladh, A. Rubio, and E. K. U. Gross. Time-dependent quantum transport: A practical scheme using density functional theory. *Phys. Rev. B*, 72(3):035308, Jul 2005.

[185] Xiao Zheng, Fan Wang, Chi Yung Yam, Yan Mo, and GuanHua Chen. Time-dependent density-functional theory for open systems. *Phys. Rev. B*, 75(19):195127, May 2007.

[186] San-Huang Ke, Rui Liu, Weitao Yang, and Harold U. Baranger. Time-dependent transport through molecular junctions. *The Journal of Chemical Physics*, 132(23):234105, 2010.

[187] M Di Ventra and T N Todorov. Transport in nanoscale systems: the micro-canonical versus grand-canonical picture. *Journal of Physics: Condensed Matter*, 16(45):8025, 2004.

[188] Joseph Maciejko, Jian Wang, and Hong Guo. Time-dependent quantum transport far from equilibrium: An exact nonlinear response theory. *Phys. Rev. B*, 74(8):085324, Aug 2006.

[189] Joel Yuen-Zhou, David G. Tempel, César A. Rodríguez-Rosario, and Alán Aspuru-Guzik. Time-dependent density functional theory for open quantum systems with unitary propagation. *Phys. Rev. Lett.*, 104:043001, Jan 2010.

[190] Alexander Prociuk and Barry D. Dunietz. Modeling time-dependent current through electronic open channels using a mixed time-frequency solution to the electronic equations of motion. *Phys. Rev. B*, 78(16):165112, Oct 2008.

[191] Na Sai, Neil Bushong, Ryan Hatcher, and Massimiliano Di Ventra. Microscopic current dynamics in nanoscale junctions. *Phys. Rev. B*, 75(11):115410, Mar 2007.

[192] G. Stefanucci, S. Kurth, A. Rubio, and E. K. U. Gross. Time-dependent approach to electron pumping in open quantum systems. *Phys. Rev. B*, 77(7):075339, Feb 2008.

[193] S. Weiss, J. Eckel, M. Thorwart, and R. Egger. Iterative real-time path integral approach to nonequilibrium quantum transport. *Phys. Rev. B*, 77(19):195316, May 2008.

[194] Petri Myöhänen, Adrian Stan, Gianluca Stefanucci, and Robert van Leeuwen. Kadanoff-baym approach to quantum transport through interacting nanoscale systems: From the transient to the steady-state regime. *Phys. Rev. B*, 80:115107, Sep 2009.

[195] Xiaofeng Qian, Ju Li, Xi Lin, and Sidney Yip. Time-dependent density functional theory with ultrasoft pseudopotentials: Real-time electron propagation across a molecular junction. *Phys. Rev. B*, 73(3):035408, Jan 2006.

[196] Kálmán Varga and Joseph A Driscoll. *Computational nanoscience: Applications for molecules, clusters, and solids*. Cambridge University Press, 2011.

[197] Bin Wang, Yanxia Xing, Lei Zhang, and Jian Wang. Transient dynamics of molecular devices under a steplike pulse bias. *Phys. Rev. B*, 81(12):121103, 2010.

[198] ChiYung Yam, Xiao Zheng, GuanHua Chen, Yong Wang, Thomas Frauenheim, and Thomas A Niehaus. Time-dependent versus static quantum transport simulations beyond linear response. *Phys. Rev. B*, 83(24):245448, 2011.

[199] Kálmán Varga. Time-dependent density functional study of transport in molecular junctions. *Phys. Rev. B*, 83:195130, May 2011.

[200] Lei Zhang, Jian Chen, and Jian Wang. First-principles investigation of transient current in molecular devices by using complex absorbing potentials. *Phys. Rev. B*, 87(20):205401, 2013.

[201] Young-Woo Son, Marvin L. Cohen, and Steven G. Louie. Energy gaps in graphene nanoribbons. *Phys. Rev. Lett.*, 97:216803, Nov 2006.

[202] A. H. Castro Neto, F. Guinea, N. M. R. Peres, K. S. Novoselov, and A. K. Geim. The electronic properties of graphene. *Rev. Mod. Phys.*, 81:109–162, Jan 2009.

[203] Bing Huang, Zuanyi Li, Zhirong Liu, Gang Zhou, Shaogang Hao, Jian Wu, Bing-Lin Gu, and Wenhui Duan. Adsorption of gas molecules on graphene nanoribbons and its implication for nanoscale molecule sensor. *The Journal of Physical Chemistry C*, 112(35):13442–13446, 2008.

[204] Haibo Wang, Thandavarayan Maiyalagan, and Xin Wang. Review on recent progress in nitrogen-doped graphene: synthesis, characterization, and its potential applications. *ACS Catalysis*, 2(5):781–794, 2012.

[205] Thomas N. Theis and Paul M. Solomon. It's time to reinvent the transistor! *Science*, 327(5973):1600–1601, 2010.

[206] T. N. Theis and H. S. P. Wong. The end of moore's law: A new beginning for information technology. *Computing in Science Engineering*, 19(2):41–50, Mar 2017.

[207] Xiaolin Li, Xinran Wang, Li Zhang, Sangwon Lee, and Hongjie Dai. Chemically derived, ultrasmooth graphene nanoribbon semiconductors. *Science*, 319(5867):1229–1232, 2008.

[208] Phaedon Avouris, Zhihong Chen, and Vasili Perebeinos. Carbon-based electronics. *Nat Nano*, 2(10):605–615, Oct 2007.

[209] Ali Javey, Jing Guo, Qian Wang, Mark Lundstrom, and Hongjie Dai. Ballistic carbon nanotube field-effect transistors. *Nature*, 424(6949):654–657, Aug 2003.

[210] Ray H. Baughman, Anvar A. Zakhidov, and Walt A. de Heer. Carbon nanotubes–the route toward applications. *Science*, 297(5582):787–792, 2002.

[211] S. Heinze, J. Tersoff, R. Martel, V. Derycke, J. Appenzeller, and Ph. Avouris. Carbon nanotubes as schottky barrier transistors. *Phys. Rev. Lett.*, 89:106801, Aug 2002.

[212] Jie Xiang, Wei Lu, Yongjie Hu, Yue Wu, Hao Yan, and Charles M. Lieber. Ge/si nanowire heterostructures as high-performance field-effect transistors. *Nature*, 441(7092):489–493, May 2006.

[213] Yat Li, Fang Qian, Jie Xiang, and Charles M. Lieber. Nanowire electronic and optoelectronic devices. *Materials Today*, 9(10):18 – 27, 2006.

[214] Jean-Pierre Colinge, Chi-Woo Lee, Aryan Afzalian, Nima Dehdashti Akhavan, Ran Yan, Isabelle Ferain, Pedram Razavi, Brendan O'Neill, Alan Blake, Mary White, Anne-Marie Kelleher, Brendan McCarthy, and Richard Murphy. Nanowire transistors without junctions. *Nat Nano*, 5(3):225–229, Mar 2010.

[215] Saptarshi Das, Hong-Yan Chen, Ashish Verma Penumatcha, and Joerg Appenzeller. High performance multilayer mos2 transistors with scandium contacts. *Nano Letters*, 13(1):100–105, 2013. PMID: 23240655.

[216] Hsiao-Yu Chang, Shixuan Yang, Jongho Lee, Li Tao, Wan-Sik Hwang, Debdeep Jena, Nanshu Lu, and Deji Akinwande. High-performance, highly bendable mos2 transistors with high-k dielectrics for flexible low-power systems. *ACS Nano*, 7(6):5446–5452, 2013. PMID: 23668386.

[217] Michael S. Fuhrer and James Hone. Measurement of mobility in dual-gated mos2 transistors. *Nat Nano*, 8(3):146–147, Mar 2013.

[218] Han Liu, Adam T. Neal, Zhen Zhu, Zhe Luo, Xianfan Xu, David Tomnek, and Peide D. Ye. Phosphorene: An unexplored 2d semiconductor with a high hole mobility. *ACS Nano*, 8(4):4033–4041, 2014. PMID: 24655084.

[219] Fengnian Xia, Han Wang, and Yichen Jia. Rediscovering black phosphorus as an anisotropic layered material for optoelectronics and electronics. *Nature Communications*, 5:4458 EP –, Jul 2014. Article.

[220] Michele Buscema, Dirk J. Groenendijk, Sofya I. Blanter, Gary A. Steele, Herre S. J. van der Zant, and Andres Castellanos-Gomez. Fast and broadband photoresponse of few-layer black phosphorus field-effect transistors. *Nano Letters*, 14(6):3347–3352, 2014. PMID: 24821381.

[221] Yexin Deng, Zhe Luo, Nathan J. Conrad, Han Liu, Yongji Gong, Sina Najmaei, Pulickel M. Ajayan, Jun Lou, Xianfan Xu, and Peide D. Ye. Black phosphorus-monolayer mos2 van der waals heterojunction pn diode. *ACS Nano*, 8(8):8292–8299, 2014. PMID: 25019534.

[222] I. Meric, C. R. Dean, N. Petrone, L. Wang, J. Hone, P. Kim, and K. L. Shepard. Graphene field-effect transistors based on boron nitride dielectrics. *Proceedings of the IEEE*, 101(7):1609–1619, July 2013.

[223] Aaron D. Franklin. Nanomaterials in transistors: From high-performance to thin-film applications. *Science*, 349(6249), 2015.

[224] Sujay B. Desai, Surabhi R. Madhvapathy, Angada B. Sachid, Juan Pablo Llinas, Qingxiao Wang, Geun Ho Ahn, Gregory Pitner, Moon J. Kim, Jeffrey Bokor, Chenming Hu, H.-S. Philip Wong, and Ali Javey. Mos2 transistors with 1-nanometer gate lengths. *Science*, 354(6308):99–102, 2016.

[225] Paul L. McEuen, Marc Bockrath, David H. Cobden, Young-Gui Yoon, and Steven G.

Louie. Disorder, pseudospins, and backscattering in carbon nanotubes. *Phys. Rev. Lett.*, 83:5098–5101, Dec 1999.

[226] P. L. McEuen, M. S. Fuhrer, and Hongkun Park. Single-walled carbon nanotube electronics. *IEEE Transactions on Nanotechnology*, 1(1):78–85, Mar 2002.

[227] Gianluca Fiori, Francesco Bonaccorso, Giuseppe Iannaccone, Tomas Palacios, Daniel Neumaier, Alan Seabaugh, Sanjay K. Banerjee, and Luigi Colombo. Electronics based on two-dimensional materials. *Nat Nano*, 9(10):768–779, Oct 2014. Review.

[228] Deji Akinwande, Nicholas Petrone, and James Hone. Two-dimensional flexible nanoelectronics. *Nature Communications*, 5:5678 EP –, Dec 2014. Review Article.

[229] D. J. Frank, Y. Taur, and H. S. P. Wong. Generalized scale length for two-dimensional effects in mosfets. *IEEE Electron Device Letters*, 19(10):385–387, Oct 1998.

[230] Suman Datta. Recent advances in high performance cmos transistors: From planar to non-planar. *The Electrochemical Society Interface*, 22(1):41–46, 2013.

[231] Feng Zhang and Joerg Appenzeller. Tunability of short-channel effects in mos2 field-effect devices. *Nano Letters*, 15(1):301–306, 2015. PMID: 25545046.

[232] Gemma C. Solomon, Carmen Herrmann, Thorsten Hansen, Vladimiro Mujica, and Mark A. Ratner. Exploring local currents in molecular junctions. *Nat Chem*, 2(3):223–228, March 2010.

[233] Sergey V. Faleev, Fran çois Léonard, Derek A. Stewart, and Mark van Schilfgaarde. Ab initio tight-binding lmto method for nonequilibrium electron transport in nanosystems. *Phys. Rev. B*, 71(19):195422, May 2005.

[234] Jeremy S. Evans, Oleg A. Vydrov, and Troy Van Voorhis. Exchange and correlation in molecular wire conductance: Nonlocality is the key. *J. Chem. Phys.*, 131(3):034106, 2009.

[235] Shenglai He, Arthur Russakoff, Yonghui Li, and Klmn Varga. Time-dependent density-functional theory simulation of local currents in pristine and single-defect zigzag graphene nanoribbons. *Journal of Applied Physics*, 120(3):034304, 2016.

[236] Philipp Schaffhauser and Stephan Kümmel. Using time-dependent density functional theory in real time for calculating electronic transport. *Phys. Rev. B*, 93:035115, Jan 2016.

[237] BD Wibking and K Varga. Quantum mechanics with complex injecting potentials. *Physics Letters A*, 376(4):365–369, 2012.

[238] Kalman Varga and J. A. Driscoll. *Computational Nanoscience*. Cambridge University Press, 2011.

[239] O. A. Rubtsova, V. I. Kukulin, and V. N. Pomerantsev. Wave-packet continuum discretization for quantum scattering. *Annals of Physics*, 360(2):49, 2015.

[240] Roi Baer, Tamar Seideman, Shahal Ilani, and Daniel Neuhauser. Ab initio study of the alternating current impedance of a molecular junction. *The Journal of chemical physics*, 120(7):3387–3396, 2004.

[241] Kuang He, Gun-do Lee, Alex W. Robertson, Euijoon Yoon, and Jamie H. Warner. Hydrogen-free graphene edges. *Nature Communications*, 5:3040, 01 2014. Copyright - Copyright Nature Publishing Group Jan 2014; Last updated - 2014-04-04.

[242] Amedeo Bellunato, Hadi ArjmandiTash, Yanina Cesa, and Grgory F. Schneider. Chemistry at the edge of graphene. *ChemPhysChem*, 17(6):785–801, 2016.

[243] Geunsik Lee and Kyeongjae Cho. Electronic structures of zigzag graphene nanoribbons with edge hydrogenation and oxidation. *Phys. Rev. B*, 79:165440, Apr 2009.

[244] Yuanbo Zhang, Tsung-Ta Tang, Caglar Girit, Zhao Hao, Michael C Martin, Alex Zettl, Michael F Crommie, Y Ron Shen, and Feng Wang. Direct observation of a widely tunable bandgap in bilayer graphene. *Nature*, 459(7248):820, 2009.

[245] Bhagawan Sahu, Hongki Min, AH MacDonald, and Sanjay K Banerjee. Energy gaps, magnetism, and electric-field effects in bilayer graphene nanoribbons. *Physical Review B*, 78(4):045404, 2008.

[246] Blanca Biel, X. Blase, Fran çois Triozon, and Stephan Roche. Anomalous doping effects on charge transport in graphene nanoribbons. *Phys. Rev. Lett.*, 102:096803, Mar 2009.

[247] Satyendra Singh Chauhan, Pankaj Srivastava, and Ashwani Kumar Shrivastava. Electronic and transport properties of boron and nitrogen doped graphene nanoribbons: an ab initio approach. *Applied Nanoscience*, 4(4):461–467, 2014.

[248] Richard Balog, Bjarke Jørgensen, Louis Nilsson, Mie Andersen, Emile Rienks, Marco Bianchi, Mattia Fanetti, Erik Lægsgaard, Alessandro Baraldi, Silvano Lizzit, et al. Bandgap opening in graphene induced by patterned hydrogen adsorption. *Nature materials*, 9(4):315–319, 2010.

[249] Stephanie J Heerema and Cees Dekker. Graphene nanodevices for dna sequencing. *Nature nanotechnology*, 11(2):127, 2016.

[250] Ye Lu, Brett Goldsmith, Douglas R Strachan, Jong Hsien Lim, Zhengtang Luo, and AT Johnson. High-on/off-ratio graphene nanoconstriction field-effect transistor. *Small*, 6(23):2748–2754, 2010.

[251] Federico Muñoz-Rojas, David Jacob, Joaquín Fernández-Rossier, and JJ Palacios. Coherent transport in graphene nanoconstrictions. *Physical Review B*, 74(19):195417, 2006.

[252] D Bischoff, M Eich, F Libisch, T Ihn, and K Ensslin. Graphene nanoribbons with wings. *Applied Physics Letters*, 107(20):203107, 2015.

[253] Jinming Cai, Pascal Ruffieux, Rached Jaafar, Marco Bieri, Thomas Braun, Stephan Blankenburg, Matthias Muoth, Ari P. Seitsonen, Moussa Saleh, Xinliang Feng, Klaus Mullen, and Roman Fasel. Atomically precise bottom-up fabrication of graphene nanoribbons. *Nature*, 466(7305):470–473, Jul 2010.

[254] Tyler Cary, Eduardo Costa Girão, and Vincent Meunier. Electronic properties of three-terminal graphitic nanowiggles. *Phys. Rev. B*, 90:115409, Sep 2014.

[255] Dong Xiang, Xiaolong Wang, Chuancheng Jia, Takhee Lee, and Xuefeng Guo. Molecular-scale electronics: From concept to function. *Chemical Reviews*, 116(7):4318–4440, 2016. PMID: 26979510.

[256] Sriharsha V. Aradhya and Latha Venkataraman. Single-molecule junctions beyond electronic transport. *Nat Nano*, 8(6):399–410, Jun 2013. Review.

[257] Constant M. Guedon, Hennie Valkenier, Troels Markussen, Kristian S. Thygesen, Jan C. Hummelen, and Sense Jan van der Molen. Observation of quantum interference in molecular charge transport. *Nat Nano*, 7(5):305–309, May 2012.

[258] Stefan Ballmann, Rainer Härtle, Pedro B. Coto, Mark Elbing, Marcel Mayor, Martin R. Bryce, Michael Thoss, and Heiko B. Weber. Experimental evidence for quantum interference and vibrationally induced decoherence in single-molecule junctions. *Phys. Rev. Lett.*, 109:056801, Jul 2012.

[259] Elisabeth H. van Dijk, Daniel J. T. Myles, Marleen H. van der Veen, and Jan C. Hummelen. Synthesis and properties of an anthraquinone-based redox switch for molecular electronics. *Organic Letters*, 8(11):2333–2336, 2006. PMID: 16706519.

[260] Gemma C Solomon, David Q Andrews, Randall H Goldsmith, Thorsten Hansen, Michael R Wasielewski, Richard P Van Duyne, and Mark A Ratner. Quantum interference in acyclic systems: conductance of cross-conjugated molecules. *Journal of the American Chemical Society*, 130(51):17301–17308, 2008.

[261] Han Liu, Adam T. Neal, Zhen Zhu, Zhe Luo, Xianfan Xu, David Tomnek, and Peide D. Ye. Phosphorene: An unexplored 2d semiconductor with a high hole mobility. *ACS Nano*, 8(4):4033–4041, 2014. PMID: 24655084.

[262] Andres Castellanos-Gomez. Black phosphorus: Narrow gap, wide applications. *The Journal of Physical Chemistry Letters*, 6(21):4280–4291, 2015. PMID: 26600394.